The Kelvin-Helmholtz Instability in the Protoplanetary Disk

Yukihiko Hasegawa

Department of Earth and Space Science

Graduate School of Science

Osaka University, Osaka, JAPAN

1-1 Machikaneyama-cho, Toyonaka, Osaka 560-0043, Japan

hasegawa@vega.ess.sci.osaka-u.ac.jp

Submitted: February 2014

The Kelvin-Helmholtz Instability in the Protoplanetary Disk

(原始惑星系円盤における ケルビン・ヘルムホルツ不安定)

Yukihiko Hasegawa

Department of Earth and Space Science

Graduate School of Science

Osaka University, Osaka, JAPAN

1-1 Machikaneyama-cho, Toyonaka, Osaka 560-0043, Japan

hasegawa@vega.ess.sci.osaka-u.ac.jp

Submitted: February 2014

Abstract

Recently, many planetary systems have been found outside the solar system owing to the progress of the observational technology. In order to explain the variety of planetary systems, it is essential to interpret the formation processes of planets. In the core accretion model of planet formation, planetesimals are assumed to form from dust particles in the protoplanetary disk first, and then they grow into planets. However, there are many significant problems. For example, due to gas drag in the protoplanetary disk, dust aggregates migrate inward and fall onto the protostar before growing to planetesimals. This is the radial drift problem. As one of the solutions to the problem, the gravitational instability (GI) of a settled dust layer has been suggested. In this scenario, dust aggregates first settle toward the midplane of the protoplanetary disk and make the dense layer of dust. Then, the dust layer becomes gravitationally unstable, and the dust layer fragments into pieces to form planetesimals before dust aggregates fall onto the protostar. However, as dust aggregates settle toward the midplane, the vertical dust density gradient increases. As a result, vertical shear of the rotational velocity in the dust layer becomes strong. This strong shear has the possibility to induce the Kelvin-Helmholtz instability (KHI), and KHI possibly induces shear-driven turbulence. If the turbulence is sufficiently strong, it prevents dust aggregates from settling toward the midplane, and as a result, GI and the planetesimal formation is possibly suppressed. On the other hand, if GI occurs before KHI, planetesimals will form. However, the condition that GI occurs before KHI during sedimentation is not known. To know this condition, it is necessary to know the dust density at the onset of KHI. Investigation for this condition is essential for understanding

the processes of the planetesimal formation. Previous studies indicated that GI is expected to occur if the dust abundance in the protoplanetary disk is sufficiently larger than that in the minimum mass solar nebula (MMSN) model. However, these works were based on the model with single-sized dust. Previous works did not take into account the appropriate distribution of dust density that is consistent with their sedimentation and growth. Since property of KHI strongly depends on the dust density profile, in order to understand correct outcome after dust sedimentation correctly, it is important to consider appropriate density distribution with sedimentation and growth of dust.

In this thesis, first, we reexamine the possibility of the onset of KHI during dust sedimentation in the protoplanetary disk. We newly use the dust density distributions that are consistent with their growth and sedimentation. To clarify the effect of each of growth and sedimentation, we compare three cases: (1) the case with the single-sized dust without growth, (2) the case with the multi-sized dust without growth, and (3) the case with the multi-sized dust with growth. As the condition for KHI, we use the classical Richardson number criterion by which KHI occurs when the Richardson number is less than 0.25. As a result, it is found that, for the cases without dust growth, GI tends to occur before the onset of KHI if the dust abundance is 660 times (for the single-sized dust) or 50 times (for the multi-sized dust) larger than that in the MMSN model. This result shows that the dust abundance required for GI of the multi-sized dust is much smaller than that of the single-sized dust. The reason is that the vertical gradient of the dust density becomes more gradual as a result of the continuous size distribution. In the case with dust growth, however, it is found that KHI tends to occur before GI even in the case with large dust abundance with continuous size distribution. This qualitative change is found to originate from the change of gas drag law from Epstein's law to Stokes' law owing to dust growth.

In the above investigation, we used the classical Richardson number criterion (RNC) with a constant critical value, 0.25. However, this critical value, 0.25, is based on the case of the incompressible, inviscid and one component fluid with the laminar flow without rotation.

Thus, it is indicated that, for general cases in the protoplanetary disk, the classical RNC whose critical value is 0.25 is not ensured to use. Thus, in the second part of this thesis, we directly perform the linear stability analysis for KHI using the dust density distribution consistent with dust sedimentation. As a result, we derived a condition in terms of the critical dust density required for GI before KHI. By comparing the condition for the onset of KHI estimated by the linear stability analysis with that estimated by the classical RNC, we discuss the validity of the classical RNC. We find that the condition estimated from the linear stability analysis agrees well with that estimated by the classical RNC within a factor of 2 in critical density. In the case without growth, it is found that the classical RNC tends to be more applicable in the case with the multi-sized dust than in the case with the single-sized dust. The classical RNC for the case with dust growth is still the open question for future work.

In conclusion, it is found that KHI tends to occur before GI even in the case with large dust abundance during sedimentation of growing dust aggregates in the protoplanetary disk. This means that small dust aggregates becomes to be unstable for KHI during their sedimentation at least once. We discuss the possible process after KHI. When dust aggregates have larger collisional velocities owing to the shear-driven turbulence than owing to sedimentation and radial drift, dust aggregates have the possibility to grow quickly or fragment. To clarify this possibility, we must take account of dust-dust collisions with shear-driven turbulence induced by KHI in future work.

Contents

Abstract **i**

Acknowledgements **viii**

1 Introduction **1**

1.1 Theory of Planet Formation 1

1.1.1 Formation of the Protoplanetary Disk 1

1.1.2 Gravitational Instability Model 2

1.1.3 Core Accretion Model 3

1.2 Models of the Protoplanetary Disk 4

1.2.1 Minimum Mass Solar Nebula Model 5

1.2.2 Gas Disk 6

1.2.3 Motion of Dust Particles 8

1.2.4 Radial and Rotational Velocities of Gas and Dust 10

1.3 Problems of Core Accretion Model 13

1.3.1 Radial Drift Problem 13

1.3.2 Collisional Fragmentation Problem 15

1.4 Formation and Fragmentation of Dust Layer 17

1.4.1 Sedimentation and Growth of Dust Aggregates 18

1.5 Problem of Shear-driven Turbulence in Planetesimal Formation 24

1.5.1 Strong Shear by Dust Sedimentation 24
1.5.2 Kelvin-Helmholtz Instability 25
1.5.3 Richardson Number 25
1.5.4 Previous Studies and Remained Problems 26
1.6 Purpose of This Thesis 28
1.7 Content of This Thesis 29

2 Sedimentation of Dust Aggregates without Growth **31**
2.1 Models 31
2.2 Sedimentation of Single-sized Dust Aggregates 32
2.2.1 The Initial Condition 32
2.2.2 Vertical Shear of the Rotational Velocity 33
2.2.3 Results 34
2.3 Effect of Size Distribution 37
2.3.1 Dust Density Profile Consistent with Dust Sedimentation 38
2.3.2 Results 40
2.4 Summary 42

3 The Case with Dust Growth **43**
3.1 Models and Methods 43
3.2 Results 44
3.2.1 Possibilities of KHI in the Early Stage 44
3.2.2 The Dust Density at the Onset of KHI for the Case with Dust Growth 49
3.3 Discussion 52
3.3.1 Dependence on the Heliocentric Distance 52
3.3.2 Treatment for Rayleigh-Taylor instability 54
3.3.3 Possibilities of the Streaming Instability 54
3.3.4 Possibility after Kelvin-Helmholtz Instability 54

3.4 Summary 55

4 Validity of the Classical RNC **57**

4.1 Models and Equations 57

4.1.1 Models of Unperturbed State 58

4.1.2 Linear Perturbation Equation 60

4.2 Results and Discussion 62

4.3 Summary 65

5 Summary and Future Prospects **67**

5.1 Summary 67

5.2 Future Prospects 69

A Toomre's Stability Criterion **71**

B Radial and Rotational Velocities of Gas and Dust Components **75**

C Linear Stability Analysis of Dust Layer for GI **79**

D Methods of Numerical Calculations **87**

D.1 Coordinates of Space and Mass 87

D.2 Numerical Method for Dust Sedimentation 88

D.2.1 Detail of Scheme 88

D.2.2 Test Calculation 89

D.3 Numerical Method for Dust Growth 90

D.3.1 Detail of Scheme 90

D.3.2 Test Calculation 93

E Linear Stability Analysis of Laminar Flow for KHI **95**

F Typical Size of Dust Aggregates in the Dust Sedimentation with Growth **103**

G Linear Perturbation Equation for KHI **107**

Bibliography **111**

Acknowledgements

I would like to thank Assistant Professor Toru Tsuribe for his continuous discussions, supports and encouragement as my supervisor.
I would like to thank Professor Fumio Takahara for his fruitful discussions and continuous encouragement.
I would like to thank Professor Kentaro Nagamine for his reading of this thesis valuable supports on the thesis defense.
I am grateful to Associate Professor Yutaka Fujita and Assistant Professor Hideyuki Tagoshi for their valuable advises.
I am also grateful to Professor Hiroshi Shibai, Professor Kentaro Terada and Professor Yoshitsugu Nakagawa for their participation in thesis committee.
I wish to thank Professor Shu-ichiro Inutsuka for his comments about my research content.
I wish to thank Secretary Yasuko Nishii for her valuable supports and advises.
I wish to thank past and present members of the Theoretical Astrophysics Group in the Osaka University for their fruitful discussions.
Thank you very much for everything you've done for me.
Finally, I wish to thank my parents for their unconditional supports throughout my entire life.

Chapter 1

Introduction

Many planetary systems were found outside the solar system owing to the progress of the observational technology (Mayor & Queloz 1995; Kalas et al. 2008; Marois et al. 2008; Doyle et al. 2011; Hirano et al. 2012; Carson et al. 2013). There are about one thousand confirmed exoplanets and more than three thousand candidates. Many observed planetary systems show different characteristics from the solar system. In order to explain the diversity of planetary systems, it is essential to understand the formation processes of planets.

In this chapter, we review the theory of the planet formation, and the purpose of this thesis is presented.

1.1 Theory of Planet Formation

1.1.1 Formation of the Protoplanetary Disk

It is considered that planets form in the protoplanetary disk. The protoplanetary disk is a thin disk around a protostar and is considered to form from the interstellar medium as described below.

The interstellar medium is composed of gas and μm-sized dust. The interstellar medium

is inhomogeneous, and dense regions of the interstellar gas (with number density $\gtrsim 10^3$ cm^{-3}, mass $\gtrsim 10^4 M_\odot$ and temperature ~ 10 K) are called as molecular clouds. The molecular cloud has clumpy structures, and particularly dense regions (with number density $\sim 10^5$ cm^{-3} and mass $\sim M_\odot$) are called as molecular cloud cores. The molecular cloud core has the angular momentum (Zhou et al. 1993; Goodman et al. 1993; Ohashi et al. 1997). This material with the small angular momentum falls towards the center of the core and forms the protostar. On the other hand, the material far from the rotation axis with larger angular momentum forms the protoplanetary disk, that is composed of gas and dust.

1.1.2 Gravitational Instability Model

In the massive protoplanetary disk, the self-gravity of the protoplanetary disk is not negligible compared with the gravity of the central star and the gas pressure of the protoplanetary disk. When the disk is gravitationally unstable and fragments into pieces, it is expected that the pieces become planets. This scenario is the gravitational instability model (Cameron 1978).

Toomre's stability criterion (Toomre 1964; Binney & Tremaine 1987) is known as a criterion for the gravitational instability of the disk. We present the linear analysis of local stability of an infinitely thin, rotating disk in the Appendix A. The Toomre's Q value is given by

$$Q \equiv \frac{c_{\rm s}\Omega_{\rm K}}{\pi G\Sigma}, \tag{1.1}$$

where $c_{\rm s}$ is the sound velocity, $\Omega_{\rm K}$ is the Keplerian angular velocity, G is the gravitational constant, and Σ is the surface density of the protoplanetary disk. It is considered that the gravitational instability of the protoplanetary disk occur when $Q < 1$. Then, from equation (1.1), it is shown that the disk fragmentation tends to occur in the case with the small central star and/or with the cold protoplanetary disk.

For the gravitational instability model, it is shown that the disk fragmentation is expected to occur at the position far from the central star. For example, in the case when the protoplanetary disk has the same angular momentum distribution with the molecular cloud core before

it collapses, it is considered that the mass of the protoplanetary disk is not so small (Hayashi et al. 1982; Kimura & Tsuribe 2012), and it is suggested that gas giant planets form far from the central star (at the heliocentric distance of tens of AU) (Rafikov 2005; Kimura & Tsuribe 2012). Recently, exoplanets are discovered by direct imaging (Kalas et al. 2008; Marois et al. 2008; Carson et al. 2013). These planets are more massive than Jupiter and are farther from the central star than Neptune (more than 30 AU). The gravitational instability model has possibility to explain the formation processes of such planets. However, the gravitational instability model is not promising to explain the formation of terrestrial planets because it is not known how rocky cores with little gas form in gas-rich fragments although a possible route is suggested (Nayakshin 2010).

1.1.3 Core Accretion Model

There are dust aggregates composed of rock and/or ice in the protoplanetary disk. Such dust aggregates are considered to coalesce into large bodies, then they finally form planets. This is the core accretion model (Safronov 1969; Hayashi et al. 1985). In the core accretion model, it is often assumed that the mass of the protoplanetary disk is much (typically 100 times) smaller than the mass of the central star as described in the next section (Hayashi 1981). This disk model explained in the next section is called as the minimum mass solar nebula (MMSN) model.

The classical core accretion model is given below. Micron-sized dust particles (monomers) collide with each other, then the dust particles stick via surface tension and become aggregates of small monomers. It is considered that the dust aggregates grow into planetesimals in consequence of iterations of such hit-and-stick collisions. However, the formation of planetesimals is one of the unresolved issue because there are many problems on the formation of planetesimals as described in section 1.3. If planetesimals form, planetesimals collide with each other and grow into large solid bodies (Kokubo & Ida 1996, 1998, 2000). The large solid bodies eventually become terrestrial planets. If the solid body grows furthermore and becomes roughly 10

times more massive than Earth mass while the gas remains in the protoplanetary disk, then the planet becomes more massive because gas around the solid core is captured by the solid core to form gas envelope (Mizuno 1980). Then, the gas giant planet is formed. At the late step of the planet formation, however, gas abundance of the protoplanetary disk decreases with time because of the accretion towards the central star, magnetically-driven wind, and/or the photoevaporation due to the irradiation from the central region. If the planet grows after most of gas in the disk have disappeared, the Neptune-like planet is formed.

The classical core accretion model is based on the on-site planet formation. It is considered that it is difficult for the core accretion model to explain the formation process of the gas giant planet farther from the central star than Neptune since it is thought that gas has disappeared from the protoplanetary disk before the formation of the massive core (Dodson-Robinson et al. 2009). However, the core accretion model has possibility to explain many kinds of planets in the solar system. In this thesis, we concentrate on the core accretion model. There are, however, many unresolved problems on the formation of planetesimals. The detail of the problems are described in section 1.3.

1.2 Models of the Protoplanetary Disk

In this section, we review the model of a protoplanetary disk where planetesimals (and planets) forms.

In this thesis, we assume that the mass of the central star is given by $1M_{\odot}$. We adopt the cylindrical coordinate system (r, ϕ, z) at rest in this section, where r is the heliocentric distance and z is the height from the midplane of the disk. For simplicity, we take no account of the magnetic tension acting on gas and dust, and neglect the electrostatic force owing to ionization of gas and to electrostatic charge of dust (Umebayashi 1983; Sano et al. 2000; Okuzumi 2009). We also assume that there is not MRI-driven turbulence because there are many tiny dust particles (Sano et al. 2000; Okuzumi & Hirose 2011, 2012).

1.2.1 Minimum Mass Solar Nebula Model

In the core accretion model, the minimum mass solar nebula (MMSN) model (Hayashi 1981) is widely adopted as the model of the protoplanetary disk. The MMSN model is based on amounts of gas and dust of the present solar system and on the elemental composition of the present Sun.

In the MMSN model, the gas surface density, $\Sigma_{\rm g}$, and the dust surface density, $\Sigma_{\rm d}$, are given by

$$\Sigma_{\rm g} = 1.7 \times 10^3 \left(\frac{r}{1[{\rm AU}]} \right)^{-3/2} [{\rm g\,cm^{-2}}], \tag{1.2}$$

and

$$\Sigma_{\rm d} = 7.1 \xi_{\rm ice} \left(\frac{r}{1[{\rm AU}]} \right)^{-3/2} [{\rm g\,cm^{-2}}], \tag{1.3}$$

where $\xi_{\rm ice}$ is the parameter which specifies abundance of condensed water ice. In the MMSN model,

$$\xi_{\rm ice} = \begin{cases} 1 & (r < r_{\rm snow}) \\ 4.2 & (r > r_{\rm snow}) \end{cases}, \tag{1.4}$$

where $r_{\rm snow}$ is the snow line. At $r > r_{\rm snow}$, H_2O becomes water ice. In the MMSN model, temperature, T, is derived from the balance of the radiative heating (from the central star) and the radiative cooling (from the disk approximated by a black body). By assuming that the protoplanetary disk is geometrically and optically thin and that temperature is uniform in the vertical direction, the radial temperature distribution is given by

$$T = 280 \left(\frac{r}{1[{\rm AU}]} \right)^{-1/2} [{\rm K}], \tag{1.5}$$

and the snow line is given by $r_{\rm snow} = 2.7$ AU.

We assume that the disk is symmetric with respect to the midplane. We assume $(r^2 + z^2)^{1/2} \simeq r$ and $\partial \Omega_{\rm K} / \partial z = 0$ for simplicity, since we assume that the protoplanetary disk is geometrically thin.

In this thesis, for the gas surface density and temperature, we adopt equations (1.2) and (1.5), respectively. For the dust surface density, we adopt equation (1.3) with dust abundance parameter, $f_{\rm d}$,

$$\Sigma_{\rm d} = 7.1 f_{\rm d}\, \xi_{\rm ice} \left(\frac{r}{1[{\rm AU}]}\right)^{-3/2} [{\rm g\,cm^{-2}}], \tag{1.6}$$

where $f_{\rm d}$ is the dust abundance parameter. The case with $f_{\rm d} = 1$ corresponds to the MMSN model.

1.2.2 Gas Disk

From equation (1.5), the sound velocity is given by

$$c_{\rm s} = \sqrt{\frac{k_{\rm B}T}{m_\mu}} = 0.99 \left(\frac{r}{1[{\rm AU}]}\right)^{-1/4} [{\rm km\,s^{-1}}], \tag{1.7}$$

where $k_{\rm B}$ is the Boltzmann constant and $m_\mu (= 3.9 \times 10^{-24}$ g) is the mass of gas molecules (the mean molecular weight is 2.34). The mean free path of gas molecules, $l_{\rm g}$, is given by $l_{\rm g} = 1.44$ cm at $r = 1$ AU (Nakagawa et al. 1986).

Gas is affected by the gravitational force from the central star, the centrifugal force, the pressure gradient force, and interaction between gas and dust. For simplicity, in the vertical direction, we assume that the gas component is in hydrostatic equilibrium without self-gravity and is not affected by the motion of dust. In such a case, the equation of motion for gas in the vertical direction is given by

$$0 = -\frac{GM_\odot z}{r^3} - \frac{1}{\rho_{\rm g}}\frac{\partial P_{\rm g}}{\partial z}, \tag{1.8}$$

where $\rho_{\rm g}$ is the gas density and $P_{\rm g} = {c_{\rm s}}^2 \rho_{\rm g}$ is the gas pressure, and $\partial P_{\rm g}/\partial z = {c_{\rm s}}^2 \partial \rho_{\rm g}/\partial z$ because of equation (1.7). From equation (1.8), the gas density is given by

$$\rho_{\rm g}(z) = \frac{\Sigma_{\rm g}}{\sqrt{\pi} H_{\rm g}} \exp\left[-\left(\frac{z}{H_{\rm g}}\right)^2\right], \tag{1.9}$$

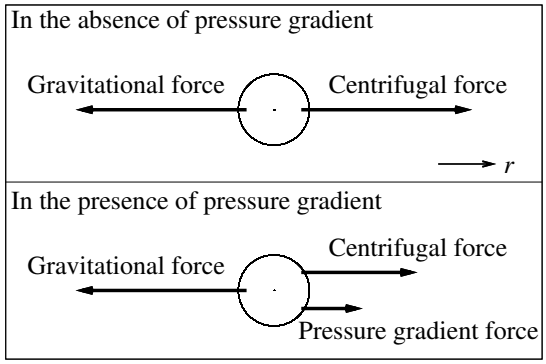

Figure 1.1: Affecting forces (arrowed lines) for gas components (circles) except for interaction between gas and dust for two cases in the absence of the pressure gradient force (upper) and in the presence of the pressure gradient force (lower).

where $H_{\rm g}$ is the scale height of the disk, given by

$$H_{\rm g} \equiv \frac{\sqrt{2}c_{\rm s}}{\Omega_{\rm K}} = 4.7 \times 10^{-2} \left(\frac{r}{1[\mathrm{AU}]} \right)^{5/4} [\mathrm{AU}]. \tag{1.10}$$

From equation (1.10), it is seen that the protoplanetary disk is geometrically thin, $H_{\rm g}/r \ll 1$.

In the radial direction, the gravitational force from the central star is $-GM_{\odot}/r^2 < 0$, and the centrifugal force is ${v_{\rm g\phi}}^2/r > 0$, where $v_{\rm g\phi}$ is the rotational velocity of gas. Hereafter, we consider the case when gas has the circular orbit. If there is no pressure gradient force and no interaction between gas and dust, gas has the Keplerian angular velocity. However, in practice, these forces affect. From equations (1.7), (1.9) and (1.10), $P_{\rm g} \propto r^{-13/4}$. Then the pressure gradient force is $-(1/\rho_{\rm g})(\partial P_{\rm g}/\partial r) > 0$. Thus, gas revolves at a slower velocity than the Keplerian velocity under the balance among the gravitational force, the centrifugal force and the pressure gradient force because of the positive pressure gradient force (Figure 1.1). We define the angular velocity of gas as $(1-\eta)\Omega_{\rm K}$ in the case when there is no interaction between gas and dust. In order to derive η, we consider the disk composed of gas only. Under the balance among the gravitational force, the centrifugal force and the pressure gradient force,

the equation of motion for gas in the radial direction is given by

$$0 = \frac{{v_{g\phi}}^2}{r} - \frac{GM_\odot}{r^2} - \frac{1}{\rho_g}\frac{\partial P_g}{\partial r}. \tag{1.11}$$

From equation (1.11) and $P_g = {c_s}^2 \rho_g$, the rotational velocity of gas is given as

$$v_{g\phi} = \left(\frac{GM_\odot}{r} + \frac{r}{\rho_g}\frac{\partial P_g}{\partial r}\right)^{1/2} = r\left(1 + \frac{{c_s}^2}{{v_K}^2}\frac{\partial \ln P_g}{\partial \ln r}\right)^{1/2}\Omega_K, \tag{1.12}$$

where v_K is the Keplerian velocity. At $r = 1$ AU, the sound velocity c_s is about 1 km s^{-1}, and the Keplerian velocity $v_K = r\Omega_K$ is about 30 km s^{-1}. Then, equation (1.12) is approximated by

$$v_{g\phi} = r\left(1 + \frac{1}{2}\frac{{c_s}^2}{{v_K}^2}\frac{\partial \ln P_g}{\partial \ln r}\right)\Omega_K \equiv r(1-\eta)\Omega_K, \tag{1.13}$$

where

$$\eta \equiv -\frac{1}{2}\frac{{c_s}^2}{{v_K}^2}\frac{\partial \ln P_g}{\partial \ln r} = \frac{13}{16}\left(\frac{H_g}{r}\right)^2 = 1.8\times 10^{-3}\left(\frac{r}{1[\mathrm{AU}]}\right)^{1/2} \ll 1. \tag{1.14}$$

Equation (1.14) shows that the gas component revolves at slightly slower velocity than the Keplerian velocity.

1.2.3 Motion of Dust Particles

Keplerian Rotation

As described in the preceding subsection, the gas component revolves at slightly slower velocity than the Keplerian velocity. On the other hand, the dust component revolves at the Keplerian velocity in the case when there is no interaction between gas and dust and when the dust component has the circular orbit since there is no pressure gradient force.

In the case with taking account of interaction between gas and dust, the drag force acts on gas and dust since gas tends to revolve at slightly slower velocity than dust aggregates.

Drag Force

The characteristic time scale for acceleration of dust aggregates owing to the gas drag force is the stopping time. In this thesis, dust aggregates are assumed to be compact and have a

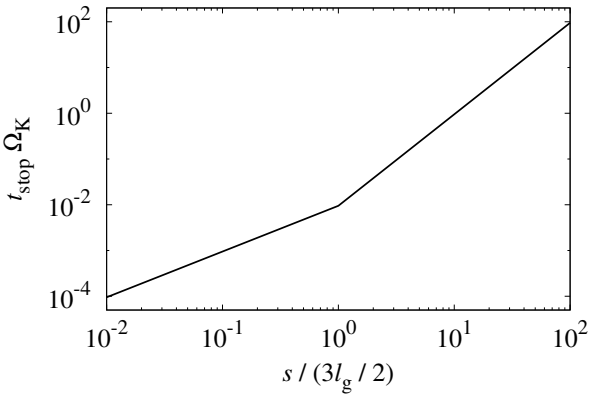

Figure 1.2: The stopping time as a function of the dust size for the case with $\rho_{\rm s} = 3\ {\rm g\,cm^{-3}}$ at $r = 1$ AU. The abscissa is the size of dust aggregates, s, in units of $3l_{\rm g}/2$. The ordinate shows the stopping time, $t_{\rm stop}$, in units of ${\Omega_{\rm K}}^{-1}$.

spherical shape with size (radius) s. In the case with $s \leq 3l_{\rm g}/2$ ($= 2.2$ cm at $r = 1$ AU), the gas drag force is given by Epstein's law (Epstein 1924). In this case, at $r = 1$ AU and $z = 0$, the stopping time, $t_{\rm stop}$, is given by

$$t_{\rm stop} = \frac{\rho_{\rm s}}{\rho_{\rm g}(z)}\frac{s}{c_{\rm s}} = 1.5 \times 10^{-3} \left(\frac{\rho_{\rm s}}{3[{\rm g\,cm^{-3}}]}\right)\left(\frac{s}{2.2[{\rm cm}]}\right)[{\rm yr}], \tag{1.15}$$

where $\rho_{\rm s}$ is the internal density of the dust aggregates. In the case with $s \geq 3l_{\rm g}/2$, gas drag is given by Stokes' law, and the stopping time is given by

$$t_{\rm stop} = \frac{2}{3}\frac{\rho_{\rm s}}{\rho_{\rm g}(z)}\frac{s^2}{l_{\rm g}c_{\rm s}} = 1.5 \times 10^{-3} \left(\frac{\rho_{\rm s}}{3[{\rm g\,cm^{-3}}]}\right)\left(\frac{s}{2.2[{\rm cm}]}\right)^2[{\rm yr}], \tag{1.16}$$

at $r = 1$ AU and $z = 0$. Figure 1.2 shows the dependence of the stopping time on the dust size changes for the case with $\rho_{\rm s} = 3\ {\rm g\,cm^{-3}}$ at $r = 1$ AU. Note that the dependence of the stopping time on the dust size changes at $s = 3l_{\rm g}/2$.

Sedimentation

The equation of motion of a dust aggregate in the vertical direction is given by

$$\frac{dv_z}{dt} = -\frac{v_z}{t_{\rm stop}} - {\Omega_{\rm K}}^2 z, \tag{1.17}$$

where t is the time and v_z is the vertical velocity of the dust aggregate, and we assume that the gas component does not have the vertical velocity. We approximate the vertical velocity of the dust aggregates by the terminal velocity. The validity of this approximation is discussed in the next paragraph. By setting $dv_z/dt = 0$ in equation (1.17), we obtain a terminal sedimentation velocity of a dust aggregate as

$$v_z(z) = -t_{\rm stop}{\Omega_{\rm K}}^2 z. \tag{1.18}$$

The characteristic time scale for sedimentation of dust aggregates is given by

$$t_{\rm sed} \equiv \frac{z}{|v_z(z)|} = \frac{1}{t_{\rm stop}{\Omega_{\rm K}}^2}. \tag{1.19}$$

Figure 1.3 shows the dependence of the sedimentation time on the dust size changes for the case with $\rho_{\rm s} = 3\ {\rm g\,cm^{-3}}$. In figure 1.3, it is shown that, in the case when the stopping time is much smaller than the Keplerian period, $t_{\rm stop}\Omega_{\rm K} \ll 1$, the characteristic time scale of sedimentation is much larger than the Keplerian period, $t_{\rm sed}\Omega_{\rm K} \gg 1$. In the case with $t_{\rm stop}\Omega_{\rm K}$ ($\equiv St$, where St is called as the Stokes number) $\ll 1 \ll t_{\rm sed}\Omega_{\rm K}$, we can approximate the vertical velocity of the dust aggregates by the terminal velocity. In figure 1.3, $t_{\rm stop}\Omega_{\rm K} = t_{\rm sed}\Omega_{\rm K} = 1$ at $s/(3l_{\rm g}/2) \simeq 10$ in the case with $\rho_{\rm s} = 3\ {\rm g\,cm^{-3}}$ at $r = 1$ AU. From equations (1.15), (1.16) and (1.19), the approximation that the vertical velocity of the dust aggregates with $\rho_{\rm s} = 3\ {\rm g\,cm^{-3}}$ is given by the terminal velocity is suggested to be valid in the case with $s \ll 23$ cm at $r = 1$ AU. In subsection 1.4.1, we will show that the terminal velocity approximation is valid during dust sedimentation toward the midplane of the protoplanetary disk.

1.2.4 Radial and Rotational Velocities of Gas and Dust

In this subsection, we summarize velocities of the gas and dust components with taking into account their interaction. Gas is affected by the gravitational force from the central star, the centrifugal force, the pressure gradient force and the drag force between gas and dust. Dust is affected by the gravitational force from the central star, the centrifugal force and the drag

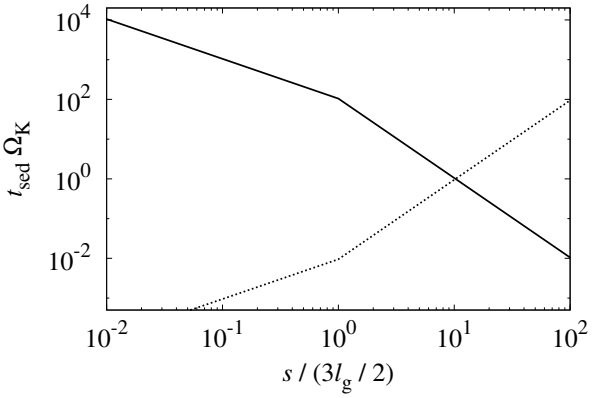

Figure 1.3: The sedimentation time as a function of the dust size for the case with $\rho_{\rm s} = 3\ {\rm g\,cm^{-3}}$ at $r = 1$ AU (solid line). The abscissa is the size of dust aggregates, s, in units of $3l_{\rm g}/2$. The ordinate shows the sedimentation time, $t_{\rm sed}$, in units of ${\Omega_{\rm K}}^{-1}$. The stopping time, $t_{\rm stop}$, is also drawn (dotted line).

force between gas and dust. Then, equations of motion for gas and dust are given by

$$\frac{d\mathbf{v}_{\rm g}}{dt} = -\frac{\rho_{\rm d}}{\rho_{\rm g}}\frac{\mathbf{v}_{\rm g} - \mathbf{v}_{\rm d}}{t_{\rm stop}} - {\Omega_{\rm K}}^2\mathbf{R} - \frac{1}{\rho_{\rm g}}\nabla P_{\rm g}, \tag{1.20}$$

and

$$\frac{d\mathbf{v}_{\rm d}}{dt} = -\frac{\mathbf{v}_{\rm d} - \mathbf{v}_{\rm g}}{t_{\rm stop}} - {\Omega_{\rm K}}^2\mathbf{R}, \tag{1.21}$$

where $\mathbf{v}_{\rm g}$ and $\mathbf{v}_{\rm d}$ are the velocity vectors of the gas and the dust components, $\rho_{\rm d}$ is the dust density and $\mathbf{R}$ is the heliocentric position vector (Nakagawa et al. 1986). For simplicity, we consider the case of steady state with $\partial/\partial t = 0$. From equations (1.20) and (1.21), we obtain the radial and rotational velocities of the gas and the dust components as

$$v_{{\rm g}r} = \frac{\rho_{\rm d}}{\rho_{\rm g} + \rho_{\rm d}}\frac{2D\Omega_{\rm K}}{D^2 + {\Omega_{\rm K}}^2}\eta v_{\rm K}, \tag{1.22}$$

$$v_{{\rm g}\phi} = (1-\eta)v_{\rm K} + \frac{\rho_{\rm d}}{\rho_{\rm g} + \rho_{\rm d}}\frac{D^2}{D^2 + {\Omega_{\rm K}}^2}\eta v_{\rm K}, \tag{1.23}$$

$$v_{{\rm d}r} = -\frac{\rho_{\rm g}}{\rho_{\rm g} + \rho_{\rm d}}\frac{2D\Omega_{\rm K}}{D^2 + {\Omega_{\rm K}}^2}\eta v_{\rm K}, \tag{1.24}$$

and

$$v_{\mathrm{d}\phi} = v_{\mathrm{K}} - \frac{\rho_{\mathrm{g}}}{\rho_{\mathrm{g}} + \rho_{\mathrm{d}}} \frac{D^2}{D^2 + {\Omega_{\mathrm{K}}}^2} \eta v_{\mathrm{K}}, \tag{1.25}$$

where $v_{\mathrm{g}r}$ and $v_{\mathrm{g}\phi}$ are the radial and rotational velocities of the gas components, $v_{\mathrm{d}r}$ and $v_{\mathrm{d}\phi}$ are the radial and rotational velocities of the dust components, and

$$D \equiv \left(1 + \frac{\rho_{\mathrm{d}}}{\rho_{\mathrm{g}}}\right) \frac{1}{t_{\mathrm{stop}}} \tag{1.26}$$

(Nakagawa et al. 1986). We present the derivation of these velocities in the Appendix B. In the case without the dust component, $\rho_{\mathrm{d}} = 0$, equation (1.23) is reduced to equation (1.13). Equations (1.22)-(1.25) show that dust aggregates spiral in towards the central star owing to the transport of angular momentum from dust to gas as a result of the drag force. The radial and rotational velocities vary with the dust size, s, and with the dust fraction, $\rho_{\mathrm{d}}/\rho_{\mathrm{g}}$. From equations (1.24) and (1.26), we have

$$v_{\mathrm{d}r} = -\frac{2 t_{\mathrm{stop}} \Omega_{\mathrm{K}}}{[1 + (\rho_{\mathrm{d}}/\rho_{\mathrm{g}})]^2 + (t_{\mathrm{stop}} \Omega_{\mathrm{K}})^2} \eta v_{\mathrm{K}}. \tag{1.27}$$

In the region with the small dust fraction, $\rho_{\mathrm{d}}/\rho_{\mathrm{g}}$, the radial velocity of dust aggregates becomes large.

From equations (1.22) and (1.24), the radial velocity for mass center of gas and dust is given by zero. From equations (1.23) and (1.25), the rotational velocity for mass center of gas and dust, v_ϕ, is given as

$$v_\phi \equiv \frac{\rho_{\mathrm{g}}}{\rho_{\mathrm{g}} + \rho_{\mathrm{d}}} v_{\mathrm{g}\phi} + \frac{\rho_{\mathrm{d}}}{\rho_{\mathrm{g}} + \rho_{\mathrm{d}}} v_{\mathrm{d}\phi} = \left(1 - \frac{\rho_{\mathrm{g}}}{\rho_{\mathrm{g}} + \rho_{\mathrm{d}}} \eta\right) v_{\mathrm{K}}. \tag{1.28}$$

Equation (1.28) shows that $v_\phi = v_{\mathrm{K}}$ in the case when there is only dust ($\rho_{\mathrm{g}} = 0$), and that $v_\phi = (1 - \eta) v_{\mathrm{K}}$ in the case when there is only gas ($\rho_{\mathrm{d}} = 0$). From equation (1.28), we have

$$\frac{\partial v_\phi}{\partial z} = \left(\frac{\rho_{\mathrm{g}}}{\rho^2} \frac{\partial \rho_{\mathrm{d}}}{\partial z} - \frac{\rho_{\mathrm{d}}}{\rho^2} \frac{\partial \rho_{\mathrm{g}}}{\partial z}\right) \eta v_{\mathrm{K}}, \tag{1.29}$$

where $\rho \equiv \rho_{\mathrm{g}} + \rho_{\mathrm{d}}$ is the total (gas plus dust) density. Note that, according to equation (1.29), it is seen that the vertical shear of the azimuthal velocity, $\partial v_\phi / \partial z$, is proportional to the vertical dust density gradient, $\partial \rho_{\mathrm{d}} / \partial z$, when the vertical gas density gradient, $\partial \rho_{\mathrm{g}} / \partial z$, is small.

1.3 Problems of Core Accretion Model

As described in subsection 1.1.3, in the core accretion model, it is considered that planetesimals (and planets) form from dust growth owing to collisions between dust aggregates. However, there are many problems on the formation of planetesimals. Especially, radial drift and collisional fragmentation of dust are significant problems as described below.

1.3.1 Radial Drift Problem

The protoplanetary disk is composed of gas and dust. As explained in subsections 1.2.2 and 1.2.3, if there is no interaction between gas and dust, dust aggregates have the Keplerian angular velocity, $\Omega_{\rm K}$, in the case with circular orbit. On the other hand, the pressure gradient force acts on gas additionally. From equations (1.13) and (1.14), gas revolves at slightly slower velocity than dust. The velocity difference between gas and dust is given by $\eta v_{\rm K}$ with $\eta \sim 10^{-3}$ at $r = 1$ AU.

If we take account of interaction between gas and dust, headwind acts on dust aggregates and drag force acts on gas and dust as in equations (1.20) and (1.21). As a result of the drag force, angular momentum is transported from dust to gas, and dust aggregates spiral in towards the central star. The drift velocity of dust aggregates is given by equation (1.27). Adachi et al. (1976) investigated the radial drift of the dust aggregate with $\Sigma_{\rm d}/\Sigma_{\rm g} \ll 1$ and $\rho_{\rm d}/\rho_{\rm g} \ll 1$, and the decay time of the spiral orbit, i.e., the time scale of the radial drift of dust aggregates, $t_{\rm drift}$, is given by

$$t_{\rm drift} \equiv \frac{r}{v_{\rm drift}} = \frac{1}{\eta\Omega_{\rm K}} \frac{1 + (t_{\rm stop}\Omega_{\rm K})^2}{2t_{\rm stop}\Omega_{\rm K}}, \tag{1.30}$$

where $v_{\rm drift}$ is the radial drift speed of dust aggregates, $|v_{{\rm d}r}|$, in equation (1.27) with $\rho_{\rm d}/\rho_{\rm g} \ll 1$. Figure 1.4 shows the drift time as the function of the stopping time in the case with $\eta \sim 2{\times}10^{-3}$. In figure 1.4, it is seen that the drift time has the minimum value at $t_{\rm stop}\Omega_{\rm K}(\equiv St) = 1$. The

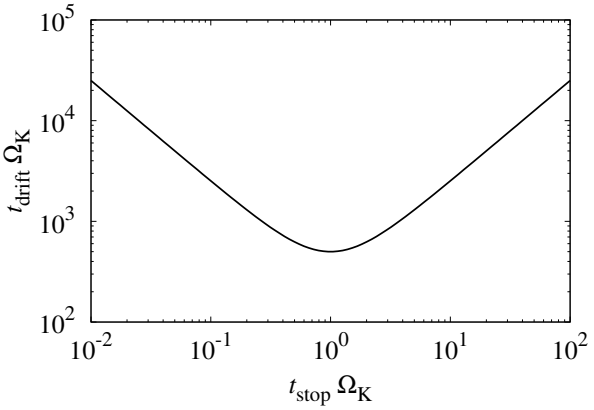

Figure 1.4: The drift time as the function of the stopping time in the case with $\eta \sim 2 \times 10^{-3}$. The abscissa is the drift time, $t_{\rm drift}$, in units of ${\Omega_{\rm K}}^{-1}$. The ordinate shows the stopping time, $t_{\rm stop}$, in units of ${\Omega_{\rm K}}^{-1}$.

minimum value of the drift time, $t_{\rm drift,\,min}$, is given by

$$t_{\rm drift,\,min} = \frac{1}{\eta\Omega_{\rm K}} \sim 10^2 \left(\frac{\eta}{2\times10^{-3}}\right)^{-1} \left(\frac{r}{1[{\rm AU}]}\right) [{\rm yr}], \tag{1.31}$$

and $t_{\rm drift,\,min} \sim 10^2$ yr at $r = 1$ AU. In the case with the internal density of dust aggregates $\rho_{\rm s} \sim 1\ {\rm g\,cm^{-3}}$ and the typical value of the gas density $\rho_{\rm g} \sim 10^{-9}\ {\rm g\,cm^{-3}}$ at $r = 1$ AU, the size of dust aggregate with $t_{\rm drift} \sim 10^2$ yr, i.e., $t_{\rm stop}\Omega_{\rm K} = 1$, is about 1 m from equation (1.16).

If the growth time scale of meter-sized dust aggregates is larger than the drift time, dust aggregates fall onto the central star and can not grow larger. For the hit-and-stick collisions, the growth time scale of dust aggregates corresponds to the mean collision time which is given by

$$t_{\rm growth} = \frac{1}{n_{\rm d}\sigma\Delta v}, \tag{1.32}$$

where $n_{\rm d}$ is the number density of dust aggregates, σ is the collisional cross section, and Δv is the relative speed of the dust-dust collision. In the case with $\Sigma_{\rm d}/\Sigma_{\rm g} \ll 1$ and with $\rho_{\rm d}/\rho_{\rm g} \ll 1$, the maximum relative speed of the dust-dust collision due to the radial motion of dust aggregates is given as $\Delta v_{{\rm d}r,\,\max} \sim v_{\rm drift} = \eta v_{\rm K} \times 2t_{\rm stop}\Omega_{\rm K}/[1 + (t_{\rm stop}\Omega_{\rm K})^2]$ from equation (1.24), and the maximum relative speed due to the azimuthal motion is given as $\Delta v_{{\rm d}\phi,\,\max} \sim$

$\eta v_{\rm K} \times (t_{\rm stop}\Omega_{\rm K})^2/[1+(t_{\rm stop}\Omega_{\rm K})^2]$ from equation (1.25). At $t_{\rm stop}\Omega_{\rm K} \sim 1$, $\Delta v_{{\rm d}r,\,\max} \gtrsim \Delta v_{{\rm d}\phi,\,\max}$. The relative speed due to the vertical motion, Δv_z, depends on z from equation (1.18). It is considered that meter-sized dust aggregates form after dust sedimentation toward the midplane of the protoplanetary disk (Nakagawa et al. 1981, 1986). Near the midplane, it is speculated that $\Delta v_{{\rm d}r,\,\max} \gg \Delta v_{z,\,\max}$. Then, $\Delta v_{\max} \sim \Delta v_{{\rm d}r,\,\max} \sim v_{\rm drift}$. To estimate the growth time scale of meter-sized dust aggregates, we assume $n_{\rm d} \sim \Sigma_{\rm d}/(4/3)\pi\rho_{\rm s}s^3H_{\rm g}$, $\sigma \sim \pi s^2$ and $\Delta v \sim v_{\rm drift}$. Then, the growth time scale at $r = 1$ AU is given as

$$t_{\rm growth} \sim \frac{4}{3}\frac{H_{\rm g}}{r}\frac{\rho_{\rm s}s}{\Sigma_{\rm d}}\frac{r}{v_{\rm drift}} = \left(\frac{\rho_{\rm s}}{3[{\rm g\,cm^{-3}}]}\right)\left(\frac{s}{38[{\rm cm}]}\right)t_{\rm drift}. \tag{1.33}$$

In equation (1.33), we used $t_{\rm drift} \equiv r/v_{\rm drift}$ [equation (1.30)]. From equation (1.33), the growth time scale of meter-sized dust aggregates with the internal density $\rho_{\rm s} \sim 1\ {\rm g\,cm^{-3}}$ is given by $t_{\rm growth} \sim t_{\rm drift}$ at $r = 1$ AU. Thus, meter-sized dust aggregates may fall onto the central star before their growth only by the simple hit-and-stick collisions. This is the radial drift problem.

1.3.2 Collisional Fragmentation Problem

In the core accretion model, dust aggregates grow by their hit-and-stick collisions. According to equations (1.15), (1.16), (1.18), (1.24), (1.25) and (1.26), the relative speed of the dust-dust collision, Δv, results from the difference of sizes between dust aggregates. (The dependence of Δv on the dust size, s, is different for different velocity components, $v_{{\rm d}r}$, $v_{{\rm d}\phi}$ and v_z, and for different gas drag laws, Epstein's law and Stokes' law.) Thus, the relative speed increases with increasing the difference of sizes. However, when the relative speed of the dust-dust collision is too large, dust aggregates can not stick but break catastrophically (Dominik & Tielens 1997; Blum & Wurm 2000; Wada et al. 2009). This prevents dust from growing. This is the collisional fragmentation problem.

The threshold of collision speed for the collisional fragmentation depends on compositions of dust aggregates and on the size of monomers (Wada et al. 2009). It is considered that dust aggregates are mainly composed of rocky particles (at the region near the central star,

$r < r_{\rm snow}$) or icy particles (far from the central star, $r > r_{\rm snow}$). Rocky particles stick owing to the intermolecular force. For rocky particles, e.g., silicate particles, the critical speed is known to be about a few $\mathrm{m\,s^{-1}}$ in the case when the size of monomers is 0.1-1 μm. On the other hand, the critical speed for icy particles is roughly larger than 10 $\mathrm{m\,s^{-1}}$ because icy particles stick owing to the hydrogen bonding additionally. Thus, it is more difficult for icy dust to fragment than for rocky dust.

Note that the realistic dependence of the outcome of the dust-dust collision on the collision speed is less well understood. Even if the collision speed is smaller than these critical speeds, it is suggested that there are the collisional compression (Dominik & Tielens 1997; Wada et al. 2007), the bouncing barrier (Zsom et al. 2010) and the electrostatic barrier (Okuzumi 2009). The outcome of the dust-dust collision varies with the collision speed and is complicated.

Figure 1.5 shows the maximum relative speed of the dust-dust collision for the case with $\rho_{\rm s} = 3\ \mathrm{g\,cm^{-3}}$ at $r = 1$ AU. The maximum collision speed of dust aggregates is about $\eta v_{\rm K} \sim 50\ \mathrm{m\,s^{-1}}$ and is independent of r because $\eta \propto r^{1/2}$ [equation (1.14)] and $v_{\rm K} \propto r^{-1/2}$. The critical speed for fragmentation of icy and porous dust aggregates with 0.1-μm-sized monomers is also about $50\ \mathrm{m\,s^{-1}}$ (Wada et al. 2009). From the detailed numerical simulations, it is shown that icy and porous dust aggregates are able to grow to km-sized planetesimals by hit-and-stick collisions with neither the radial drift problem nor the collisional fragmentation problem in the limited region, $r_{\rm snow} < r \lesssim 10$ AU (Okuzumi et al. 2012). On the other hand, however, it is considered that rocky dust can not grow to planetesimals by hit-and-stick collisions. The radial drift speed of a 5-cm-sized dust aggregate with the internal density $\rho_{\rm s} = 3\ \mathrm{g\,cm^{-3}}$ is about 5 $\mathrm{m\,s^{-1}}$ in the case with the gas density $\rho_{\rm g} \sim 10^{-9}\ \mathrm{g\,cm^{-3}}$ at $r = 1$ AU and is comparable with the critical speed for fragmentation of rocky particles. Even if dust aggregates are porous, the internal density remains $\rho_{\rm s} \gtrsim 10^{-5}\ \mathrm{g\,cm^{-3}}$ at $r = 1$ AU because of the collisional compression (Suyama et al. 2008; Okuzumi et al. 2012). In such a case, the radial drift speed of a 30-m-sized dust aggregate is comparable with the critical speed for fragmentation of rocky particles at $r = 1$ AU. Thus, in the MMSN model, it is expected that rocky dust aggregates

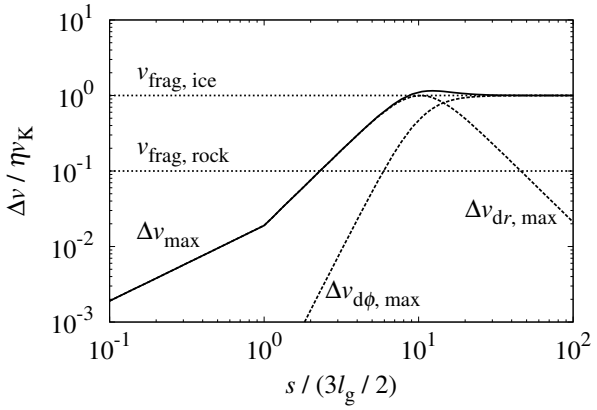

Figure 1.5: The maximum relative speed of the dust-dust collision, $\Delta v_{\rm max} \equiv (\Delta v_{{\rm d}r,\,\rm max}{}^2 + \Delta v_{{\rm d}\phi,\,\rm max}{}^2)^{1/2}$, for the case with $\rho_{\rm s} = 3\ {\rm g\,cm^{-3}}$ at $r = 1$ AU (solid line). The abscissa is the size of dust aggregates, s, in units of $3l_{\rm g}/2$. The ordinate shows the maximum relative speed of the dust-dust collision, $\Delta v_{\rm max}$, in units of $\eta v_{\rm K}$. The maximum collision speed due to the radial motion, $\Delta v_{{\rm d}r,\,\rm max}$, and that due to the azimuthal motion, $\Delta v_{{\rm d}\phi,\,\rm max}$, are also drawn (dashed lines). Dotted lines shows the critical speeds for fragmentation of icy dust, $v_{\rm frag,\,ice}$ ($\sim 50\ {\rm m\,s^{-1}}$), and for rocky dust, $v_{\rm frag,\,rock}$ ($\sim 5\ {\rm m\,s^{-1}}$) (Wada et al. 2009).

are unable to grow to km-sized planetesimals by hit-and-stick collisions before the radial drift problem. As a means of growth of rocky dust aggregates other than the hit-and-stick collision, the gravitational instability of the dust layer (described in the next section) is considered.

1.4 Formation and Fragmentation of Dust Layer

In the laminar gas flow, dust aggregates settle toward the midplane of the protoplanetary disk owing to the gravitational force from the central star. As a result of dust sedimentation, a thin and dense layer of dust, so-called dust layer, forms. The dust layer is composed of 1-10-cm-sized dust aggregates at $r = 1$ AU (Nakagawa et al. 1981, 1986). If the dust layer is dense enough, the dust layer is gravitationally unstable and it fragments into pieces (Goldreich & Ward 1973; Sekiya 1983). We present the stability of the dust layer in the Appendix C. At

$r = 1$ AU, the mass of the piece is about 10^18 g in the MMSN model and the size of the piece is several kilometers in the case when the internal density of the piece is about 1 g cm^{-3}. The pieces have large dust densities and strong self-gravitational forces, then a lot of dust aggregates in the pieces are strongly compressed by strong self-gravitational forces. In such a case, km-sized planetesimals directly form. This is the gravitational instability (GI) of the dust layer. Hereafter, GI refers the gravitational instability of the dust layer. The critical density for GI (Sekiya 1983) is given by

$$\rho_{\rm c} = \frac{0.61 M_\odot}{r^3} = 3.6 \times 10^{-7} \left(\frac{r}{1[{\rm AU}]} \right)^{-3} [{\rm g\,cm^{-3}}], \tag{1.34}$$

and GI is expected to occur when the density in the dust layer is larger than the critical density, $\rho_{\rm c}$. The time scale of the gravitational contraction of the pieces is given by the free-fall time, $t_{\rm ff} \sim (G\rho_{\rm d})^{-1/2}$. In the case with $\rho_{\rm d} = \rho_{\rm c}$, the free-fall time is given by

$$t_{\rm ff} \sim \frac{1}{\sqrt{G\rho_{\rm c}}} = \frac{1}{\sqrt{0.61}\Omega_{\rm K}} \sim 0.2 T_{\rm K} < T_{\rm K}, \tag{1.35}$$

where $T_{\rm K} \equiv 2\pi/\Omega_{\rm K}$ is the period of rotation. Thus, if GI begins, it is expected that the cm-sized dust aggregates collapse to km-sized planetesimals in much a shorter time scale than their drift time onto the central star. In order to form the dust layer with the large dust density, dust aggregates have to settle close to the midplane of the protoplanetary disk. Thus, dust sedimentation is the key to understand GI.

1.4.1 Sedimentation and Growth of Dust Aggregates

Dust aggregates settle toward the midplane at the same time as their radial drift onto the central star. From equations (1.14), (1.19) and (1.30), we have

$$\frac{t_{\rm sed}}{t_{\rm drift}} = \frac{2\eta}{1 + (t_{\rm stop}\Omega_{\rm K})^2} \ll 1. \tag{1.36}$$

Equation (1.36) shows that the fractional change of an orbital radius of a dust aggregate during its sedimentation is significantly small as compared with the orbital radius. Thus, during dust

sedimentation before GI, from equation (1.36), we do not take into account the radial motion of dust aggregates in this thesis.

From equations (1.15), (1.16) and (1.18), the sedimentation velocity of dust aggregates depends on the dust size. Dust aggregates grow during dust sedimentation, and the dust size vary with dust sedimentation (Nakagawa et al. 1981, 1986). During the sedimentation and growth of dust aggregates, evolution of the dust size distribution is described by the coagulation equation described by

$$\begin{aligned}&\frac{\partial}{\partial t}n(m,z)+\frac{\partial}{\partial z}[n(m,z)v_z(m,z)]\\&=-n(m,z)\int_0^\infty A(m,m',z)n(m',z)dm'\\&\quad+\frac{1}{2}\int_0^m A(m-m',m',z)n(m-m',z)n(m',z)dm',\end{aligned}\tag{1.37}$$

where $n(m,z)dm$ is the number density of the dust aggregates with mass between m to $m+dm$ at height z, and $A(m,m',z)$ is the coalescence rate for two dust aggregates with m and m' at z. The second term in the left-hand side of equation (1.37) shows the sedimentation of dust aggregates with m at z. The first term in the right-hand side of equation (1.37) shows the growth of dust aggregates from m to other mass. The second term in the right-hand side of equation (1.37) shows the growth of dust aggregates to m from other mass. The symbol $n(m,z)dz$ gives a mass function in z to $z+dz$. The dust density at z, $\rho_{\rm d}(z)$, is given by

$$\rho_{\rm d}(z)=\int_0^\infty mn(m,z)dm.\tag{1.38}$$

As for the velocity that induces dust-dust collisions during dust sedimentation before GI, we take into account velocities generated during sedimentation and thermal Brownian motion and ignore the radial and azimuthal motions as is the case with Nakagawa et al. (1981). We assume that the coalescence rate, $A(m,m',z)$, is given by

$$A(m,m',z)=\pi(s+s')^2(\Delta v_{\rm s}+\Delta v_{\rm B}),\tag{1.39}$$

where $\Delta v_{\rm s}$ and $\Delta v_{\rm B}$ are the relative velocities of two dust aggregates due to sedimentation and to the thermal motion, respectively, and are given by

$$\Delta v_{\rm s} = |v_z(m,z) - v_z(m',z)|, \tag{1.40}$$

and

$$\Delta v_{\rm B} = \sqrt{k_{\rm B}T}\sqrt{\frac{1}{m}+\frac{1}{m'}}, \tag{1.41}$$

respectively. For simplicity, we ignore the collisional compression (Dominik & Tielens 1997; Wada et al. 2007), the bouncing barrier (Zsom et al. 2010) and the electrostatic barrier (Okuzumi 2009). From equation (1.39), we assume that the coalescence rate, $A(m,m',z)$, is proportional to the relative velocities, $\Delta v_{\rm s}$ and $\Delta v_{\rm B}$. Equation (1.41) shows that $\Delta v_{\rm B}$ is independent of z. On the other hand, $\Delta v_{\rm s}$ increases with increasing z in the case with constant m, m' and $\rho_{\rm s}$ from equations (1.15), (1.16), (1.18) and (1.40). Thus, it is expected that dust aggregates at large z grow faster than at small z.

Integrating equation (1.37) with respect to m, we obtain

$$\frac{\partial}{\partial t}\int_0^\infty mn dm + \frac{\partial}{\partial z}\int_0^\infty mnv_z dm = 0. \tag{1.42}$$

Using equations (1.38) and (1.42), we obtain

$$\frac{\partial}{\partial t}\rho_{\rm d}(z) + \frac{\partial}{\partial z}[\rho_{\rm d}(z)\bar{v}_z(z)] = 0, \tag{1.43}$$

which is the continuity equation for dust aggregates treated as fluid, where the mean sedimentation velocity of dust fluid at z is given by

$$\bar{v}_z(z) = \frac{\int_0^\infty v_z(m,z)\, mn(m,z)dm}{\int_0^\infty mn(m,z)dm}. \tag{1.44}$$

To see the tendency of dust growth, one example of dust density evolution with growth is shown below. Dust density $\rho_{\rm d}(z)$ is assumed to be symmetric with respect to the midplane, and we examine only the region of $z \geq 0$. In this subsection, as an initial condition, the initial density of dust is assumed to be

$$\rho_{\rm d}(z) = \rho_{\rm d0}(0)\exp\left[-\left(\frac{z}{H_{\rm g}}\right)^2\right], \tag{1.45}$$

where

$$\rho_{\rm d0}(0) = \frac{\Sigma_{\rm d}}{\sqrt{\pi} H_{\rm g}}. \tag{1.46}$$

We set $r = 1$ AU. We assume that all dust aggregates have the same initial size, $s_0 = 1.0 \times 10^{-4}$ cm, and that the internal density of dust aggregates, $\rho_{\rm s}$, is 3 g cm^{-3}. The numerical method of this calculation is presented in the Appendix D.

Figures 1.6 and 1.7 show the distributions of dust density and mass functions from $t = 0$ yr to 1000 yr in the case with $f_{\rm d} = 1$. From figure 1.6, it is shown that dust aggregates primarily grow to $s/s_0 \sim 10^3$ in $z/H_{\rm g} \sim 1$ at $t \lesssim 300$ yr. From figure 1.7, it is shown that dust aggregates with $s/s_0 \sim 10^3$ secondly settle toward the midplane, $z = 0$, with growing to $s/s_0 \sim 10^4$, i.e., $s \sim 1$ cm, and that the dense dust layrer with $\rho_{\rm d} \sim \rho_{\rm c}$ finally forms near the midplane. This result shows that dust aggregates before GI are so small that the stopping times of dust aggregates are much shorter than the Keplerian period [equation (1.15)]. Thus, the approximation of the terminal velocity used in equations (1.18) and (1.22)-(1.25) is reasonable. These tendencies are similar to the results in Nakagawa et al. (1981, 1986).

From figure 1.7, the peak of the distribution of dust density, $\rho_{\rm d}$, appears at $z > 0$ while dust aggregates settle from $z/H_{\rm g} \sim 1$ to the midplane. For reference, in the case without dust growth, the peak of $\rho_{\rm d}$ remains at $z = 0$ during the dust sedimentation (Garaud & Lin 2004, and section 2.3). In summary, dust growth strongly influences the dust sedimentation and time evolutions of the profile of the dust density. This tendency is similar to the result in Tanaka et al. (2005).

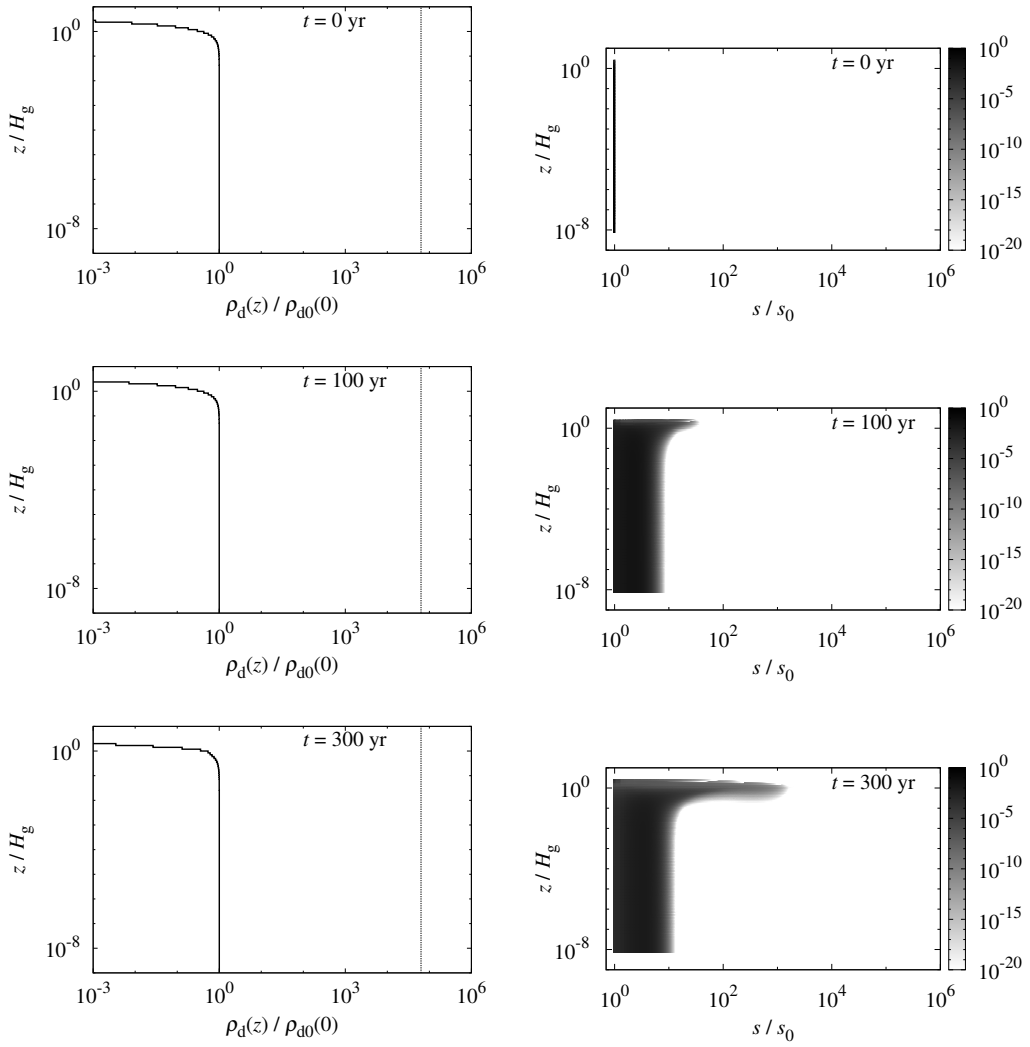

Figure 1.6: The distributions of dust density (left side) and mass functions (right side) in the case with $f_{\rm d} = 1$ at $t = 0$ yr (the top), 100 yr (the center) and 300 yr (the bottom). For the distributions of dust density (left side), the abscissas show the dust density, $\rho_{\rm d}(z)$, in unit of $\rho_{\rm d0}(0)$. The ordinates show z coordinates in unit of $H_{\rm g}$. The critical density, $\rho_{\rm c}$, is also drawn (dotted line). For the distributions of mass functions (right side), the abscissas show the dust size, s, in unit of s_0. The ordinates show z coordinates in unit of $H_{\rm g}$. The contrasting density of the color shows the mass function, $mn(m, z)$, in unit of $\rho_{\rm d0}(0)/m_0$, where $m_0 = (4/3)\pi\rho_{\rm s}{s_0}^3$.

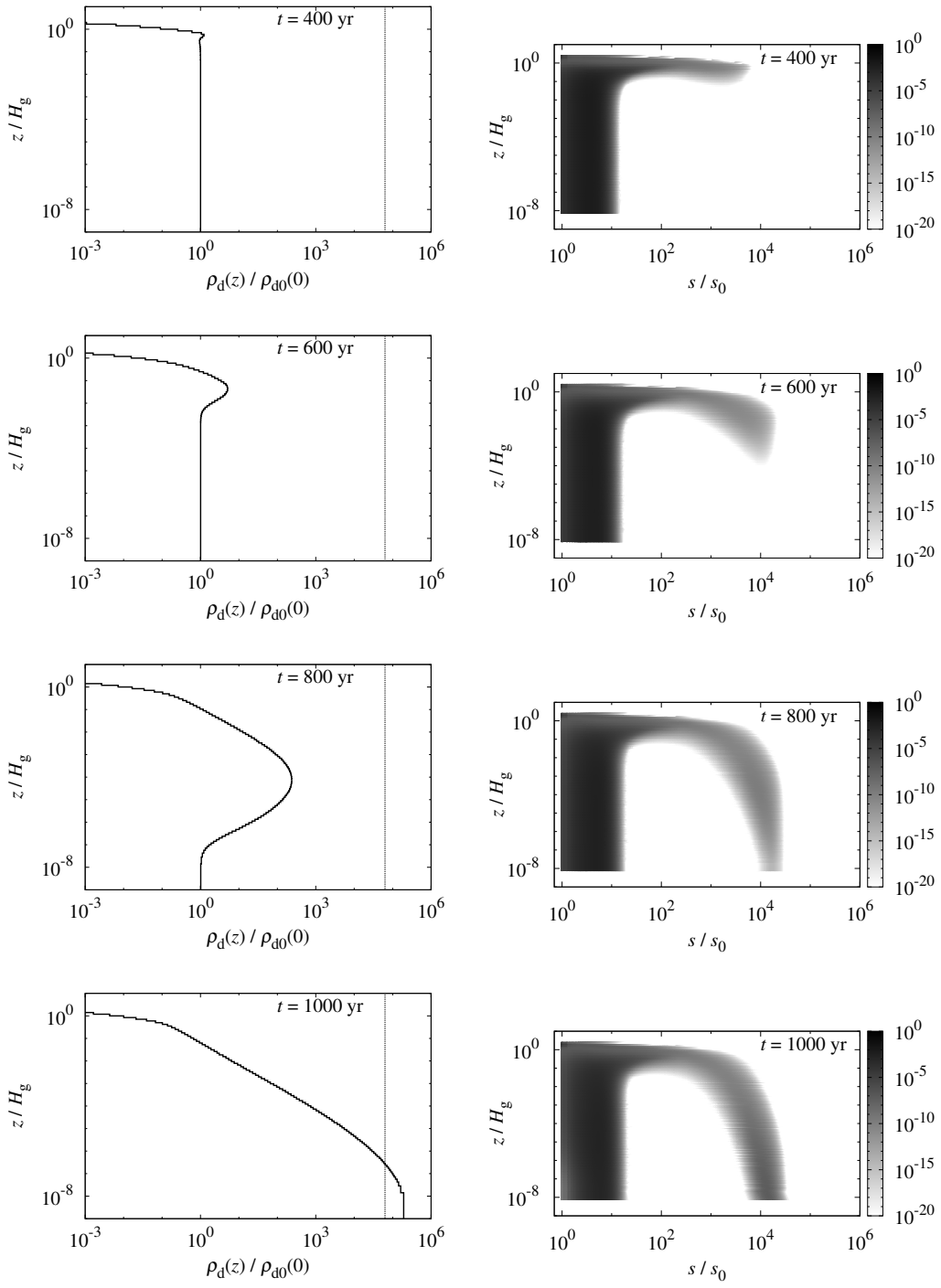

Figure 1.7: Same as figure 1.6, but for the case at $t = 400$ yr (the top), 600 yr (the second from the top), 800 yr (the second from the bottom) and 1000 yr (the bottom).

1.5 Problem of Shear-driven Turbulence in Planetesimal Formation

1.5.1 Strong Shear by Dust Sedimentation

Before the onset of GI, dust aggregates are so small that the stopping times of dust aggregates are much smaller than the Keplerian period (Nakagawa et al. 1981, 1986). Then, dust aggregates are small enough to couple strongly to gas on the rotational time scale. In such a case, the mixture of gas and dust is often treated as the one component fluid for the azimuthal motion. For small dust aggregates, the sedimentation times are much larger than the Keplerian period. On the rotational time scale, we regard the vertical motion of dust aggregates as being smaller than their azimuthal motion. In such a case, the flow of the mixed fluid is assumed to be laminar on the rotational time scale. Thus, in this section, we regard the mixture of gas and dust as the one component fluid with laminar flow and consider the azimuthal motion of the mixed fluid.

The rotational velocity of the mixed fluid of gas and dust depends on a ratio of gas to dust density as shown in equation (1.28), and the vertical shear of the rotational velocity is given by equation (1.29). Equation (1.28) shows that $v_\phi = v_{\rm K}$ in the case when there is only dust ($\rho_{\rm g} = 0$), and that $v_\phi = (1-\eta)v_{\rm K}$ in the case when there is only gas ($\rho_{\rm d} = 0$).

As dust aggregates settle toward the midplane, the dust-rich region forms near the midplane and dust-poor regions form outside. Then, the absolute value of the vertical dust density gradient, $|\partial\rho_{\rm d}/\partial z|$, increases with dust sedimentation. In this case, according to equation (1.29), the vertical shear of the rotational velocity of the mixed fluid, $|\partial v_\phi/\partial z|$, increases, and the strong shear is expected. The emergence of the strong shear flow reminds us of the Kelvin-Helmholtz instability (KHI) (Chandrasekhar 1961). We explain about KHI in the next subsection. KHI is suggested to induce shear-driven turbulence and that turbulence due to KHI prevents dust aggregates from settling further toward the midplane (Cuzzi et al. 1993;

Sekiya 1998). If KHI occur and dust aggregates are stirred up sufficiently, the condition for GI in section 1.4 is possibly violated. Thus, KHI has the possibility to be an important problem for the formation of planetesimals by GI.

1.5.2 Kelvin-Helmholtz Instability

In this subsection, we present a brief description of the process of the onset of KHI. For simplicity, we consider the case when there are laminar flows of two superposed fluids with a relative horizontal velocity. If fluctuation exists at the plane interface between the two fluids, regions with different velocities exist alternately at the same height where the plane interface exist in the unperturbed state. In such a case, the regions with different velocities at the same height tend to mix, i.e., the different velocities tend to become the same velocity owing to the momentum transfer between the regions. Then, the surplus kinetic energy is caused as the result of the mixing (Chandrasekhar 1961). Then, the amplitude of fluctuation is more amplified owing to the surplus kinetic energy. In consequence, amplification of fluctuation occurs repeatedly. Iterations of the amplification of fluctuation result from the relative horizontal velocity between the fluids, i.e., the shear of the velocity between the fluids. This instability of laminar flows induced by the shear of the velocity is the Kelvin-Helmholtz instability (KHI). KHI induce turbulence. To understand the detail of KHI and shear-driven turbulence, we have to perform the linear stability analysis and/or the numerical simulation. The basic linear stability analysis for KHI is presented in the Appendix E, and the linear stability analysis for the more realistic case for the protoplanetary disk is presented in chapter 4.

1.5.3 Richardson Number

As described in subsection 1.5.2, KHI induces amplification of the amplitude of fluctuation in the direction of z owing to the surplus kinetic energy. For the purpose, the surplus kinetic energy should be larger than the work to transfer fluid elements. From this request, a condition

for instability of the laminar flow of the incompressible and inviscid fluid with velocity v_ϕ and density ρ is given as

$$-\frac{g_z}{\rho}\frac{\partial \rho}{\partial z}\left(\frac{\partial v_\phi}{\partial z}\right)^{-2} \equiv J < J_{\rm c}, \tag{1.47}$$

where g_z is the z component of the acceleration due to the gravitational force. The symbol J is the Richardson number that is known as an indicator to discuss the possibility of KHI (Chandrasekhar 1961). If J is smaller than a critical value, $J_{\rm c}$, KHI is expected to be induced. For the laminar flow of the incompressible, inviscid and one component fluid with no rotation, the critical Richardson number is known as $J_{\rm c} = 0.25$ (Chandrasekhar 1961). For other laminar flows, on the other hand, it is considered that the critical Richardson number is not 0.25 as described in subsection 1.5.4.

1.5.4 Previous Studies and Remained Problems

Investigations of KHI and the turbulence are essential for understanding the processes of the planetesimal formation, and there are many previous studies (Weidenschilling 1980; Cuzzi et al. 1993; Sekiya 1998; Dobrovolskis et al. 1999; Sekiya & Ishitsu 2000, 2001; Ishitsu & Sekiya 2002, 2003; Johansen et al. 2006; Michikoshi & Inutsuka 2006; Bai & Stone 2010). Cuzzi et al. (1993) numerically calculated the gravitational sedimentation and turbulent diffusion of two fluid that are gas and single-sized dust. They showed that the dust layer turns out to be a quasi-steady state by the balance of the gravitational sedimentation and turbulent diffusion and that GI does not occur as long as dust aggregates are roughly smaller than 1 m. Sekiya (1998) considered a case that the Richardson number is forced to be nearly equal to the critical value, $J_{\rm c} = 0.25$, at the whole region, and derived the analytical solution of dust density distribution in the quasi-stationary state. Sekiya (1998) showed that GI is expected to occur in the case when the dust abundance in the protoplanetary disk is 20 times larger than that in MMSN model. Sekiya & Ishitsu (2001) and Ishitsu & Sekiya (2003) calculated the growth rate of KHI by performing the linear stability analysis with regarding the mixture

of gas and dust as one component fluid. They assumed that the dust density is given by the hybrid density distribution that is composed of an inner region with a constant density and outer sinusoidal transition regions. They showed that the growth rate of the unstable mode decreases with increasing the dust abundance in the protoplanetary disk. Michikoshi & Inutsuka (2006) performed the linear stability analysis with regarding the two-component fluid that are gas and single-sized dust. They used the same dust density profile as Sekiya & Ishitsu (2001). They showed that GI does not occur as long as dust aggregates are roughly smaller than 10 m for MMSN model.

However, above previous studies did not take account of dust growth. As described in subsection 1.4.1 and Nakagawa et al. (1981), dust growth strongly influences the dust sedimentation and time evolutions of the profile of the dust density. It is expected that the site of occurrence of KHI will differ according to the presence or absence of dust growth since equations (1.29) and (1.47) show that the vertical dust density gradient is related to the condition for KHI. Thus, dust growth is essential to understand not only the dust sedimentation but also the occurrence of KHI. Dust aggregates grow due to dust-dust collisions while they settle toward the midplane (Nakagawa et al. 1981, 1986). Nakagawa et al. (1986) shows that the law of gas drag force on dust aggregates is changed from Epstein to Stokes as a result of dust sedimentation with dust growth. They also show that the change of the law of gas drag has an influence on the sedimentation process. Therefore, to investigate KHI in the settled dust layer, it is important to take account of dust growth.

As described in subsection 1.5.3, Chandrasekhar (1961) showed that the critical Richardson number is 0.25. However, such a classical Richardson number criterion, $J_c = 0.25$, is derived only for the case with the incompressible, inviscid and laminar fluid, and an effect of the rotation is neglected. There are many previous studies of the Richardson number criterion (RNC) and the critical Richardson number in the protoplanetary disk (Sekiya & Ishitsu 2000; Garaud & Lin 2004; Gómez & Ostriker 2005; Chiang 2008; Barranco 2009; Lee et al. 2010). They show that the critical Richardson number depends on the assumed density profile and varies with

the dust abundance in the protoplanetary disk and with the rotation of the protoplanetary disk. If the possible dust density resulting from KHI with $J_c \neq 0.25$ is totally different from the dust density with the classical RNC, $J_c = 0.25$, then the classical RNC is not ensured to discuss KHI for general cases in the protoplanetary disk. Thus, we should calculate the critical Richardson number at the onset of KHI without using the classical RNC, and we should clarify how the possible dust density before KHI calculated without using the classical RNC is different from that calculated with using the classical RNC.

1.6 Purpose of This Thesis

In this thesis, we focus on the effects of dust sedimentation with dust growth on the Kelvin-Helmholtz instability. The best way to investigate the planetesimal formation is to calculate all of the related physical processes: e.g., viscous diffusion of gas, motion of turbulent gas, interaction between gas and dust through drag force, sedimentation and radial drift of dust, motion of dust stirred up by turbulence, dust growth, dust fragmentation, time evolutions of the size distribution and internal structure of dust, gravitational instability of dust layer, and so on. However, it is difficult to simulate all physical processes numerically at the same time because of the computer performance.

In the case with dust growth, there is a size distribution of dust aggregates, and the size distribution changes with time due to dust growth. To focus on and to investigate the effects of dust growth on the possibility of KHI, we take account of sedimentation, growth and the size distribution of dust aggregates only, and discuss the possibility of KHI by using the dust density distribution consistent with their sedimentation history in the disk. The classical RNC, $J_c = 0.25$, is used first for simplicity. Later, the classical RNC is reinvestigated. In this thesis, we adopt the following approach.

1. First, we consider the case without dust growth in order to evince the effects of dust growth on the possibility of KHI. We investigate two cases without and with an initial

size distribution of dust aggregates. We calculate dust sedimentation and discuss the possibility of KHI by using the dust density distribution consistent with their sedimentation.

2. Next, we consider the case with dust growth. We calculate dust sedimentation and dust growth, and discuss the possibility of KHI by using the dust density distribution consistent with their sedimentation. We show the effects of dust growth on the possibility of KHI with comparing the case without dust growth to the case with dust growth.

3. To discuss the validity of the classical Richardson number criterion $J_c = 0.25$ used above, we perform the linear analysis of KHI. The conditions of the onset of KHI derived from the linear analysis are compared with the conditions derived from the classical Richardson number criterion.

1.7 Content of This Thesis

In chapter 2, we show numerical results for sedimentation of dust grains without growth. In chapter 3, results are shown for the case with dust growth. In chapter 4, we show results for the growth rate and the critical Richardson number, and we discuss the validity of the classical Richardson number criterion. In chapter 5, summary and future prospects are presented.

Chapter 2

Sedimentation of Dust Aggregates without Growth

In this thesis, we focus on the effects of dust sedimentation in the sense of the density profile and dust growth on the possibility of KHI. In order to clarify the effects of dust growth, we first consider the case without dust growth in the protoplanetary disk to compare with the case with dust growth.

This chapter is mainly based on our paper, Hasegawa & Tsuribe (2013).

2.1 Models

In this thesis, we assume that the mass of the central star is given by $1M_{\odot}$. Since radial drift is small during sedimentation time [equation (1.36)], we neglect the radial motion of dust aggregates and we set $r = 1$ AU for simplicity. We assume that the protoplanetary disk is axisymmetric with respect to the rotational axis of the disk and is symmetric with respect to the midplane of the disk. In this chapter, we adopt the cylindrical coordinate system (r, ϕ, z) at rest. The gas surface density, $\Sigma_{\rm g}$, the dust surface density, $\Sigma_{\rm d}$ and temperature, T, are assumed to be equations (1.2), (1.6) and (1.5), respectively. The sound velocity, $c_{\rm s}$, is given

by equation (1.7). The scale height of the disk, $H_{\rm g}$, is given by equation (1.10). The value of η is given by equation (1.14). For simplicity, we assume $(r^2+z^2)^{1/2} \simeq r$ and $\partial\Omega_{\rm K}/\partial z = 0$. We assume that all dust aggregates are so small (μm-cm) that the stopping time is always given by equation (1.15) and that $t_{\rm stop}\Omega_{\rm K} \ll 1 \ll t_{\rm sed}\Omega_{\rm K}$ [from equations (1.15) and (1.19)]. As described in subsection 1.4.1, we approximate velocities of the gas and dust components by the terminal velocity given as equations (1.18) and (1.22)-(1.25). To discuss the possibility of KHI, we calculate the Richardson number given by equation (1.47) with $g_z = {\Omega_{\rm K}}^2 z$, $\rho = \rho_{\rm g}+\rho_{\rm d}$ and $J_{\rm c} = 0.25$, for simplicity (Sekiya & Ishitsu 2001). For the revolutions of gas and dust, we treat the mixture of gas and dust as one component fluid with laminar flow as described in subsection 1.5.1, and we give the azimuthal velocity of mixed fluid of gas and dust as equation (1.28). Since we focus on the phase before KHI, we assume that there is no turbulence in the disk.

According to equations (1.29) and (1.47), the Richardson number strongly depends on the distribution of the dust density. We calculate the Richardson number for the dust density given by numerical calculations at each time.

2.2 Sedimentation of Single-sized Dust Aggregates

First, we consider the sedimentation of single-sized dust aggregates. We assume the gas density, $\rho_{\rm g}(z)$, as equation (1.9).

2.2.1 The Initial Condition

Dust density, $\rho_{\rm d}(z)$, is assumed to be symmetric with respect to the midplane, and we examine only the region of $z \geq 0$. As an initial condition, the initial density of dust is assumed to be

$$\rho_{\rm d}(z) = \frac{\Sigma_{\rm d}}{\sqrt{\pi}H_{\rm d}} \exp\left[-\left(\frac{z}{H_{\rm d}}\right)^2\right], \tag{2.1}$$

where $H_{\rm d}$ is the time dependent scale height of the dust density profile with $H_{\rm d} = H_{\rm g}$ at $t = 0$. At $t = 0$, equation (2.1) corresponds to equation (1.45).

We assume the same initial functional form for $\rho_{\rm g}(z)$ and $\rho_{\rm d}(z)$, and we neglect the dependence of $v_{\rm K}$ on z. At $t = 0$, $\partial\rho_{\rm g}/\partial z = -(2z/{H_{\rm g}}^2)\rho_{\rm g}$ and $\partial\rho_{\rm d}/\partial z = -(2z/{H_{\rm g}}^2)\rho_{\rm d}$. Then, $\partial v_\phi/\partial z = 0$ from equation (1.29), and the rotational velocity of the mixed fluid of gas and dust aggregates, v_ϕ, at $t = 0$ is independent of z. Thus, $J = \infty$ at $t = 0$ from equation (1.47), i.e., the initial state is stable against KHI.

2.2.2 Vertical Shear of the Rotational Velocity

We assume that all dust aggregates are small enough ($s \lesssim 1$ cm), and that the drag force is given by Epstein's law [equation (1.15)]. From equations (1.15) and (1.19), it is shown that the characteristic time scale of sedimentation is much larger than the Keplerian period, $t_{\rm sed}\Omega_{\rm K} \gg 1$, when the stopping time is much smaller than the Keplerian period, $t_{\rm stop}\Omega_{\rm K} \ll 1$. In such a case, for single-sized dust aggregates without growth, the profile of the dust density evolves in a self-similar manner (Garaud & Lin 2004). Then, we do not have to solve equation (1.37) numerically and can derive the dust density distribution analytically. Here, during the sedimentation of dust, the distribution of the gas density is assumed to remain constant as equation (1.9). When the time evolution of the dust density proceeds in a self-similar manner, the dust density profile in $t > 0$ is also given by equation (2.1) with a temporally decreasing scale height of the dust density profile, $H_{\rm d}(t)$, with $0 < H_{\rm d}(t) \leq H_{\rm g}$. Using equations (1.9), (1.28), and (2.1), we have

$$\frac{\partial v_\phi}{\partial z} = 2\eta z v_{\rm K}\left(\frac{1}{{H_{\rm g}}^2} - \frac{1}{{H_{\rm d}}^2}\right)\frac{\rho_{\rm g}(z)\rho_{\rm d}(z)}{[\rho_{\rm g}(z) + \rho_{\rm d}(z)]^2}. \tag{2.2}$$

Substituting (1.14) and (2.2) into (1.47), an analytical formula for Richardson number can be derived as

$$J = \frac{1}{2}\left(\frac{H_{\rm g}}{\eta r}\right)^2 \frac{(H_{\rm d}/H_{\rm g})^4}{[1-(H_{\rm d}/H_{\rm g})^2]^2}\left[\rho_{\rm g} + \left(\frac{H_{\rm d}}{H_{\rm g}}\right)^{-2}\rho_{\rm d}\right]\frac{(\rho_{\rm g}+\rho_{\rm d})^3}{{\rho_{\rm g}}^2{\rho_{\rm d}}^2}. \tag{2.3}$$

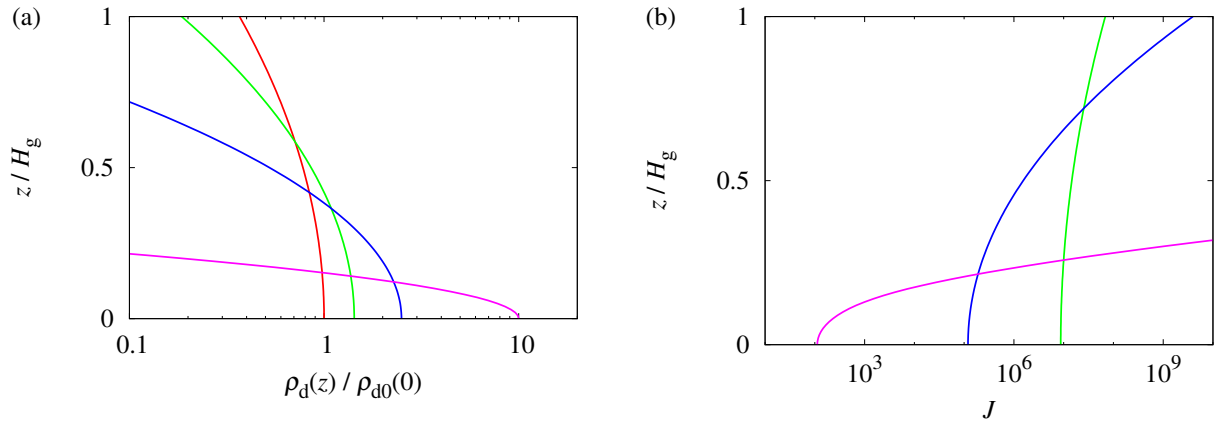

Figure 2.1: Dust density and Richardson number at $r = 1$ AU for the case with single-sized dust aggregates with $f_d = 1$ where H_d/H_g are 1 (red), 0.7 (green), 0.4 (blue) and 0.1 (magenta), respectively. [In the case with $s = 1$ cm and with $\rho_s = 3\ \mathrm{g\,cm^{-3}}$, $t \sim 0$ yr (red), 10 yr (green), 30 yr (blue) and 80 yr (magenta), respectively.] (a) The distribution of dust density (solid line). The abscissa shows the dust density, $\rho_d(z)$, in unit of $\rho_{d0}(0)$. The ordinate shows z coordinates in unit of H_g. (b) The distribution of Richardson number (solid line). The abscissa shows Richardson number. The ordinate shows z coordinates in unit of H_g.

Figure 2.1 shows the time evolution of dust density and the Richardson number for the case with $f_d = 1$. In figure 2.1, it is seen that the maximum value of dust density increases and the minimum value of the Richardson number decreases with dust sedimentation.

Since the profile of the dust density evolves in a self-similar manner, the results shown in this section are independent of the dust size as long as the stopping time is given by Epstein's law [equation (1.15)], and the time scale is renormalized.

2.2.3 Results

Figure 2.2 shows results of the distributions of the dust density and the Richardson number when $\rho_d(0) \simeq 160\rho_{d0}(0)$ for the case with $f_d = 1$, where H_d is $0.0062H_g$. In figure 2.2, it is seen that dust density at the midplane is much smaller than the critical density for

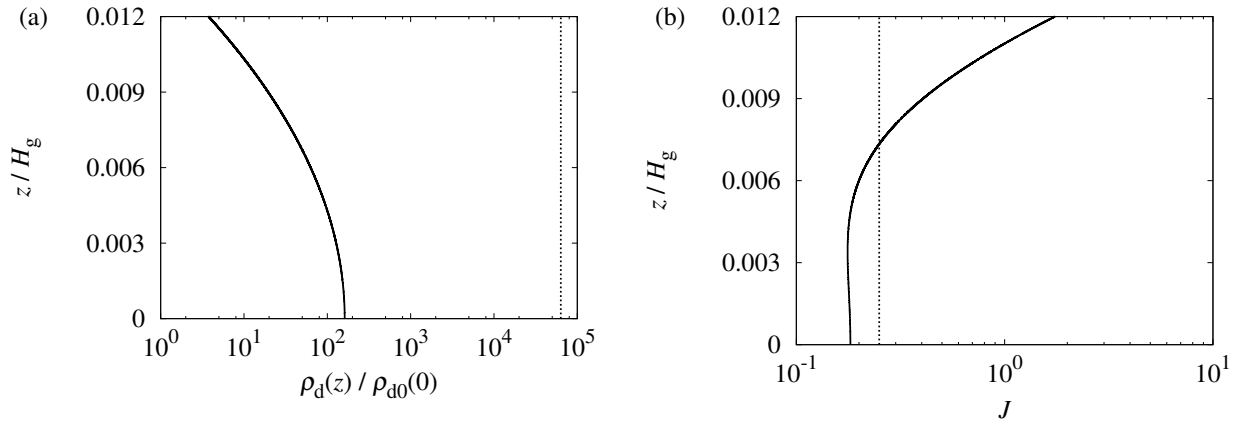

Figure 2.2: Dust density and Richardson number at $r = 1$ AU for the case with single-sized dust aggregates with $f_d = 1$ where H_d is $0.0062 H_g$. The abscissa and the ordinate show the same as ones of figure 2.1. (a) The distribution of dust density (black solid line). The critical density ρ_c is also drawn (dotted line). (b) The distribution of Richardson number (black solid line). The critical value J_c is also drawn (dotted line). This figure was presented in Hasegawa & Tsuribe (2013) as figure 1.

GI, $\rho_c = 6.3 \times 10^4 \rho_{d0}(0)$ [equation (1.34)], and that the Richardson number is smaller than $J_c = 0.25$ around the midplane ($z/H_g \lesssim 0.0075$). Thus, KHI is expected before GI in this case with $f_d = 1$ at $r = 1$ AU.

In the previous study, it is indicated that GI tends to occur if the dust abundance in the protoplanetary disk is much larger than that according to the MMSN model (Sekiya 1998). This result is based on the assumption of equilibrium condition for KHI everywhere. In this thesis, we used a non-equilibrium time-dependent density profile during sedimentation in order to consider the possibility for GI in the case with a large f_d. We seek the condition of the dust abundance, f_d, by which GI occurs before the onset of KHI. In figure 2.2a, it can be seen that the distribution of dust density has the maximum in the midplane. When f_d is larger than 1, the dotted line in figure 2.2a moves to left (compare the dotted lines in figures 2.2a, 2.3a and 2.4a), because the abscissa is proportional to $[\rho_{d0}(0)]^{-1} \propto {f_d}^{-1}$. The dust density at the midplane is the first to reach the critical density for GI, because the time development of the dust density proceeds in a self-similar manner. A characteristic H_d when the dust density at

the midplane attains ρ_c can be obtained from equation (2.1). We define the characteristic H_d as H_c. With using $z = 0$, $H_d = H_c$ and $\rho_d(z) = \rho_c$ in equation (2.1), respectively, H_c is given by

$$H_c = \frac{\Sigma_d}{\sqrt{\pi}\rho_c} = 1.6 \times 10^{-5} f_d H_g \propto f_d. \tag{2.4}$$

In figure 2.2b, it is seen that the distribution of the Richardson number has a local minimum value at $z/H_g = 3.5 \times 10^{-3} = z_c/H_g$, where z_c is the height where the distribution of the Richardson number takes the local minimum value. At $z = z_c$, from $\partial J/\partial z|_{z=z_c} = 0$, we find

$$\rho_g(z_c) = 2\rho_d(z_c), \tag{2.5}$$

by assuming $H_d/H_g \ll 1$ because KHI begins when the dust layer becomes thin. From equation (2.5), z_c is given as

$$z_c = \left[\ln\left(\frac{2\Sigma_d}{\Sigma_g}\frac{H_g}{H_d}\right)\right]^{1/2} H_g. \tag{2.6}$$

The Richardson number at $z = z_c$ is given by

$$J(z = z_c) = \frac{27}{8}\left(\frac{H_d}{\eta r}\right)^2, \tag{2.7}$$

by assuming $H_d/H_g \ll 1$. From equations (2.4), (2.5) and (2.7), the condition of the dust abundance, f_d, which is necessary for GI to occur before KHI is derived as

$$f_d = \left[\frac{8\pi}{27}J(z = z_c)\right]^{1/2} \eta r \rho_c \left(\frac{\Sigma_d}{f_d}\right)^{-1} \geq 6.6 \times 10^2 \equiv f_{dc}, \tag{2.8}$$

at $r = 1$ AU. Note that $\Sigma_d \propto f_d$.

In figure 2.3, results of the distributions of the dust density and the Richardson number for the case with $f_d = 6.6 \times 10^2$ are shown. In figure 2.3, it can be seen that the dust density at the midplane indeed attains the critical density, ρ_c, and that Richardson number remains marginally larger than the critical alue, J_c. Thus, in the case with single-sized dust aggregates without growth at $r = 1$ AU, GI is expected to occur before KHI only if the dust surface density is much larger than the gas surface density.

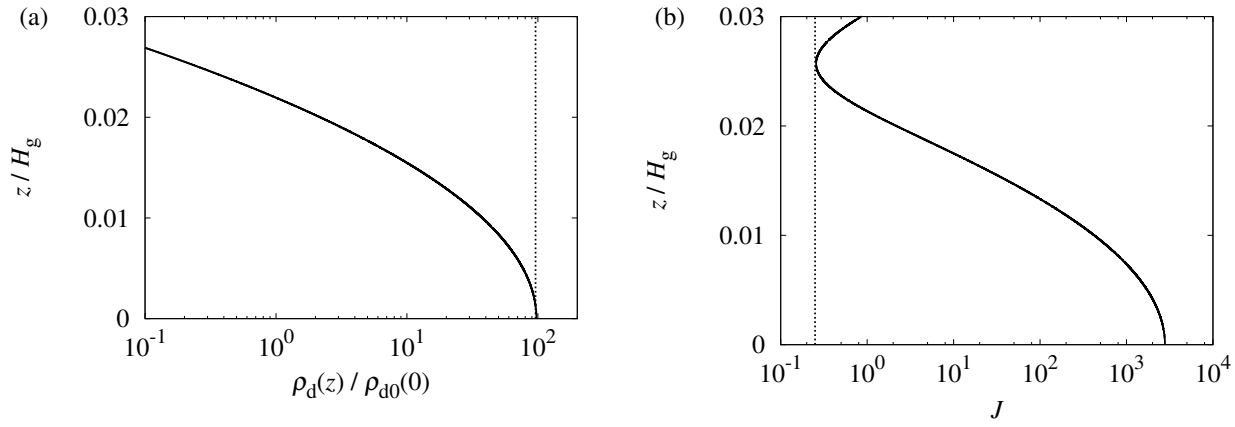

Figure 2.3: Same as Figure 2.2, but for the case with $f_d = 6.6 \times 10^2$ where H_d is H_c. This figure was presented in Hasegawa & Tsuribe (2013) as figure 2.

This tendency is similar to the result of Sekiya (1998), but the value of f_{dc} given here ($f_{dc} = 6.6 \times 10^2$) is larger than the value given in Sekiya (1998) ($f_{dc} = 16.8$). The value of f_{dc} in Sekiya (1998) corresponds to the condition that the protoplanetary disk is in a quasi-equilibrium state for KHI. On the other hand, the value of f_{dc} given here corresponds to the condition that GI occurs before KHI during sedimentation. The condition used here is more stringent than that used in Sekiya (1998). This is why the value of f_{dc} derived here is larger than the value in Sekiya (1998).

2.3 Effect of Size Distribution

Result given in section 2.2 are independent of the dust size as long as the stopping time is given by Epstein's law [equation (1.15)], provided that the time scale is renormalized, since the profile of the dust density evolves in a self-similar manner. The characteristic time scale for the sedimentation of the dust aggregates in equation (1.19) depends on size of the dust aggregates. Thus, even for the same time, the scale height of the dust density profile for different sizes of dust aggregates is different. Therefore, it is expected that the total dust density profile

will change from the initial Gaussian profile if dust aggregates have a size distribution. From equations (1.29) and (1.47), the gradient of the dust density is the essential quantity for the condition of KHI. Thus, it is expected that the condition required for GI to occur before KHI in the case with the initial size distribution of dust aggregates is expected to be different from that in the case without the size distribution. Next, we consider the sedimentation of multi-sized dust aggregates without growth. We consider $N_{\rm d}$ kinds of dust sizes. We consider the case when s is given by integer multiples of the minimum size of dust aggregates, $s_{\rm min}$, and when the maximum value, $s_{\rm max}$, is given by $N_{\rm d}s_{\rm min}$. For simplicity, we assume that all dust aggregates are so small that the stopping time is always given by Epstein's law [equation (1.15)].

2.3.1 Dust Density Profile Consistent with Dust Sedimentation

We assume the initial dust density distribution to be equation (1.45). The distribution of the total dust density, $\rho_{\rm d}(z)$, is given as

$$\rho_{\rm d}(z) = \sum_{i=1}^{N_{\rm d}} \rho_{{\rm d},\, s_i}(z), \tag{2.9}$$

where $\rho_{{\rm d},\, s_i}(z)$ is the density of dust aggregates in the ith bin of size coordinates, s_i, at z. We consider the case when $\rho_{{\rm d},\, s_i}(z)$ is given as

$$\rho_{{\rm d},\, s_i}(z) \propto \frac{1}{H_{{\rm d},\, s_i}} \exp\left[-\left(\frac{z}{H_{{\rm d},\, s_i}} \right)^2 \right], \tag{2.10}$$

where $H_{{\rm d},\, s_i}$ is the scale height of the dust density profile for dust aggregates with size s_i. At $t = 0$, $H_{{\rm d},\, s_i} = H_{\rm g}$ for all s_i.

We assume that gas density is uniform and that $\rho_{\rm g}(z) = \rho_{\rm g}(0)$ at any z, for simplicity. According to equation (1.15), the stopping time of dust aggregates, $t_{\rm stop} = (\rho_{\rm s}/\rho_{\rm g})(s/c_{\rm s})$, is proportional to s, and is constant with z. We assume that the internal density of all dust aggregates is the same. Then, the sedimentation velocity (in the vertical direction) of dust

aggregates, $v_z(z) \propto t_{\rm stop} z$, is proportional to s and to z. From the time evolution of $z(t)$ with different size of dust aggregates with $z = H_{\rm g}$ at $t = 0$, the formula for $H_{{\rm d},\, s_i}$ can be derived as

$$\frac{H_{{\rm d},\, s_i}}{H_{\rm g}} = \left(\frac{H_{{\rm d},\, s_{\rm min}}}{H_{\rm g}} \right)^{s_i / s_{\rm min}} . \tag{2.11}$$

In equation (2.11), it is seen that $H_{{\rm d},\, s_i}$ is determined only by $H_{{\rm d},\, s_{\rm min}}$ and $s_i / s_{\rm min}$, instead of s_i, because the sizes of all dust aggregates are normalized by the smallest dust aggregates.

For simplicity, the initial size distribution is assumed to be a power law of dust size,

$$n_{{\rm d},\, s_i}(z) = n_{{\rm d},\, s_{\rm min}}(z) \left(\frac{s_i}{s_{\rm min}} \right)^p , \tag{2.12}$$

where $n_{{\rm d},\, s_i}(z)$ is the initial condition of the number density in the ith bin at z with a power index p. We assume $p = -3$ for simplicity. In the case with $p = -3$, ${s_i}^3 n_{{\rm d},\, s_i}(z)$ is equal to ${s_{\rm min}}^3 n_{{\rm d},\, s_{\rm min}}(z)$ from equation (2.12). Then, the initial condition of $\rho_{{\rm d},\, s_i}(z)$ is given by

$$\rho_{{\rm d},\, s_i}(z) = \frac{4}{3} \pi \rho_{\rm s} {s_i}^3 n_{{\rm d},\, s_i}(z) = \frac{4}{3} \pi \rho_{\rm s} {s_{\rm min}}^3 n_{{\rm d},\, s_{\rm min}}(z) = \rho_{{\rm d},\, s_{\rm min}}(z). \tag{2.13}$$

In the case with $p = -3$, equation (2.13) shows that the initial dust densities in different bins are the same. In this case, $\rho_{{\rm d},\, s_i}(z)$ is given by

$$\rho_{{\rm d},\, s_i}(z) = \frac{1}{N_{\rm d}} \rho_{\rm d}(z) = \frac{1}{N_{\rm d}} \frac{\Sigma_{\rm d}}{\sqrt{\pi} H_{{\rm d},\, s_i}} \exp \left[- \left(\frac{z}{H_{{\rm d},\, s_i}} \right)^2 \right] . \tag{2.14}$$

In the case without dust growth, $\rho_{{\rm d},\, s_i}(z)$ with different i evolves independently, with different $H_{{\rm d},\, s_i}$. From equations (2.9), (2.11) and (2.14), we can derive analytical solutions of $\rho_{\rm d}(z)$ by summation of $\rho_{{\rm d},\, s_i}(z)$ for all i. We assume $N_{\rm d} = 1000$.

The dependence of $H_{{\rm d},\, s_i}$ and $n_{{\rm d},\, s_i}$ on $s_i / s_{\rm min}$ shows that the results shown in this section are independent of the size of individual dust aggregates, s_i, provided that the time scale is renormalized, and are dependent on the size ratio, $s_i / s_{\rm min}$, as long as the stopping time is given by Epstein's law [equation (1.15)].

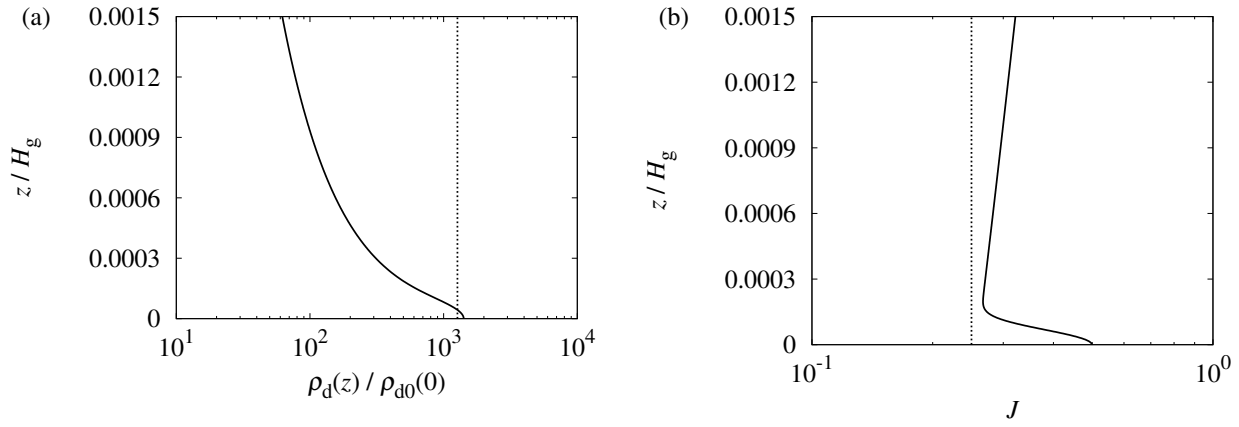

Figure 2.4: Dust density and the Richardson number at $r = 1$ AU for the case with multi-sized dust aggregates with $f_d = 50$. The lines, abscissas, and ordinates show the same as ones in figure 2.2. This figure was presented in Hasegawa & Tsuribe (2013) as figure 3.

2.3.2 Results

Figure 2.4 shows the dust density and the Richardson number for the case with $f_d = 50$. In figure 2.4, it can be seen that the dust density at the midplane attains the critical density for GI, ρ_c [equation (1.34)], and that the Richardson number remains larger than the critical value. This demonstrates that a dust fraction 50-times larger than that of the MMSN model induces GI before KHI in the case with multi-sized dust without growth. Note that this dust fraction is about 10-times smaller than that for single-sized dust (figure 2.3). We found that this tendency is seen in two cases with $p = -2$ and $p = -4$. We also checked the dependence on N_d, and found that this is the case with $N_d \gtrsim 2$. Thus, it is seen that KHI tends to be inhibited before GI if dust aggregates is multi-sized even with the same f_d.

Figure 2.5 shows the dust density in the midplane at the onset of KHI for both cases with single- and multi-sized dust. The symbol $\rho_{d,KH}$ is the dust density in the midplane at the onset of KHI. It is seen that dust density in the midplane at the onset of KHI increases with increasing the dust abundance in both cases with single- and multi-sized dust. Especially, it is seen that the condition $\rho_{d,KH} = \rho_c$ is attained by a smaller dust abundance, $f_d \simeq 50$, in the

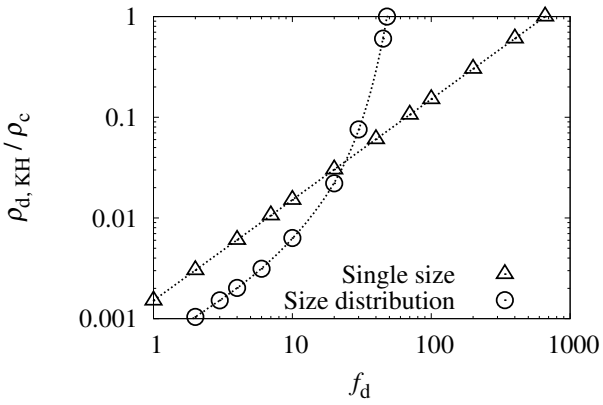

Figure 2.5: Dust density in the midplane and in $r = 1$ AU at the onset of KHI for the case with single-sized dust aggregates (triangles), and for the case with multi-sized dust aggregates (circles). The abscissa shows dust abundance, $f_{\rm d}$, and the ordinate shows the dust density, $\rho_{\rm d,KH}$, in units of $\rho_{\rm c}$. The approximated curves are also drawn (dotted lines). This figure was presented in Hasegawa & Tsuribe (2013) as figure 4.

case with multi-sized dust, rather than single-sized dust, $f_{\rm d} \simeq 700$. On the other hand, in the case with $f_{\rm d} \lesssim 20$, the dust density in the case with multi-sized dust is smaller than that in the case with single-sized dust. We explain this result below.

In this section, we assume that $\partial\rho_{\rm g}/\partial z = 0$. From equations (1.29) and (1.47), the Richardson number is given as

$$J = \frac{z}{\eta r}\left(1 + \frac{\rho_{\rm d}}{\rho_{\rm g}}\right)^3 \left(-\frac{\eta r}{\rho_{\rm g}}\frac{\partial\rho_{\rm d}}{\partial z}\right)^{-1}. \tag{2.15}$$

Equation (2.15) shows that KHI tends to occur in the cases with the small dust density, $\rho_{\rm d}$, and/or with the large absolute value of the vertical dust density gradient, $\partial\rho_{\rm d}/\partial z$. In the case with multi-sized dust, the larger dust aggregates can settle quickly while the smaller dust aggregates still remain almost in the initial state. Then, the values of the dust density and the absolute value of the vertical dust density gradient near the midplane become larger than the case with single-sized dust. In the case with $f_{\rm d} \sim 1$, the absolute value of the vertical dust density gradient becomes too large though the dust density does not become large yet. Thus,

in the case with $f_{\rm d} \sim 1$, the dust density at the onset of KHI in the case with multi-sized dust becomes smaller than that in the case with single-sized dust. On the other hand, in the case with $f_{\rm d} \gg 1$, the dust density can become large before the absolute value of the vertical dust density gradient becomes large because the characteristic scale of dust height, $H_{{\rm d},s_i}$, is different for different i for multi-sized dust. Therefore, in the case with $f_{\rm d} \gg 1$, the dust density at the onset of KHI in the case with multi-sized dust becomes larger, i.e., easier for GI to occur than that in the case with single-sized dust. This tendency is seen in cases with $p = -2$ and $p = -4$.

2.4 Summary

In the case without dust growth, the results are summarized as follows:

1. In the case when the abundance of dust aggregates is given as MMSN model, KHI is expected to occur when the dust density at the midplane is still much smaller than the critical density for GI.

2. GI tends to occur if the abundance of dust aggregates is larger.

3. In the case with multi-sized dust aggregates, the required abundance of dust for GI has a possibility to be smaller than that in the case with single-sized dust aggregates.

The above results are based on the assumption that multi-sized dust aggregates settle without growth. However, in actual protoplanetary disks, dust aggregates are expected to collide mutually and to grow during sedimentation. If dust aggregates grow, the size distribution and the largest size of dust aggregates will change with time. In order to understand the actual condition for GI before KHI, the dust density distribution for multi-sized dust with dust growth during sedimentation is required. Next, we consider the case with dust growth.

Chapter 3

The Case with Dust Growth

In this chapter, we consider the condition for GI before KHI with taking account of the sedimentation and growth of multi-sized dust aggregates.

This chapter is mainly based on our paper, Hasegawa & Tsuribe (2013).

3.1 Models and Methods

In this thesis, we assume that the mass of the central star is given by $1M_{\odot}$. As is the case with chapter 2, we neglect the radial motion of dust aggregates and we set $r = 1$ AU for simplicity. We assume that the protoplanetary disk is axisymmetric with respect to the rotational axis of the disk and is symmetric with respect to the midplane of the disk. In this chapter, we adopt the cylindrical coordinate system (r, ϕ, z) at rest. The gas surface density, $\Sigma_{\rm g}$, the dust surface density, $\Sigma_{\rm d}$ and temperature, T, are assumed to be equations (1.2), (1.6) and (1.5), respectively. The sound velocity, $c_{\rm s}$, is given by equation (1.7). We assume the gas density, $\rho_{\rm g}(z)$, as equation (1.9). The scale height of the disk, $H_{\rm g}$, is given by equation (1.10). The value of η is given by equation (1.14). For simplicity, we assume $(r^2 + z^2)^{1/2} \simeq r$ and $\partial\Omega_{\rm K}/\partial z = 0$. The stopping time of dust aggregates is given by equations (1.15) or (1.16). As described in subsection 1.4.1, we approximate velocities of the gas and dust components by the terminal

velocity given as equations (1.18) and (1.22)-(1.25). In order to calculate the growth and sedimentation of dust aggregates, we numerically solve the coagulation equation (1.37). The coalescence rate is given by equations (1.39), (1.40) and (1.41). To discuss the possibility of KHI, we calculate the Richardson number given by equation (1.47) with $g_z = {\Omega_{\rm K}}^2 z$, $\rho = \rho_{\rm g} + \rho_{\rm d}$ and $J_{\rm c} = 0.25$, for simplicity (Sekiya & Ishitsu 2001). For the revolutions of gas and dust, we treat the mixture of gas and dust as one component fluid with laminar flow as described in subsection 1.5.1, and we give the azimuthal velocity of mixed fluid of gas and dust as equation (1.28). Since we focus on the phase before KHI, we assume that there is no turbulence in the disk.

Dust density, $\rho_{\rm d}(z)$, is assumed to be symmetric with respect to the midplane, and we examine only the region of $z \geq 0$. As the initial condition, the initial density of dust is given by equations (1.45) and (1.46). We assume that all dust aggregates have the same initial size, $s_0 = 1.0 \times 10^{-4}$ cm, and that the internal density of dust aggregates, $\rho_{\rm s}$, is 3 $\mathrm{g\,cm^{-3}}$. The numerical methods of calculations are presented in the Appendix D.

3.2 Results

3.2.1 Possibilities of KHI in the Early Stage

Figure 3.1 shows the distribution of the dust density and the Richardson number at $t = 25$ yr. In figure 3.1, although the distribution of the dust density changes little from the initial state in this short period, it can be seen that the Richardson number becomes small enough for small z, especially at $z/H_{\rm g} \lesssim 10^{-4} \ll 1$. This rapid decline of J did not appear in the case without the growth of dust aggregates, described in chapter 2. We suppose that the growth of dust aggregates is the origin of this rapid decline in the Richardson number at $z/H_{\rm g} \ll 1$ and at $t/t_{\rm sed} \ll 1$.

Equations (1.29) and (1.47) show that the Richardson number is a function of the gradient

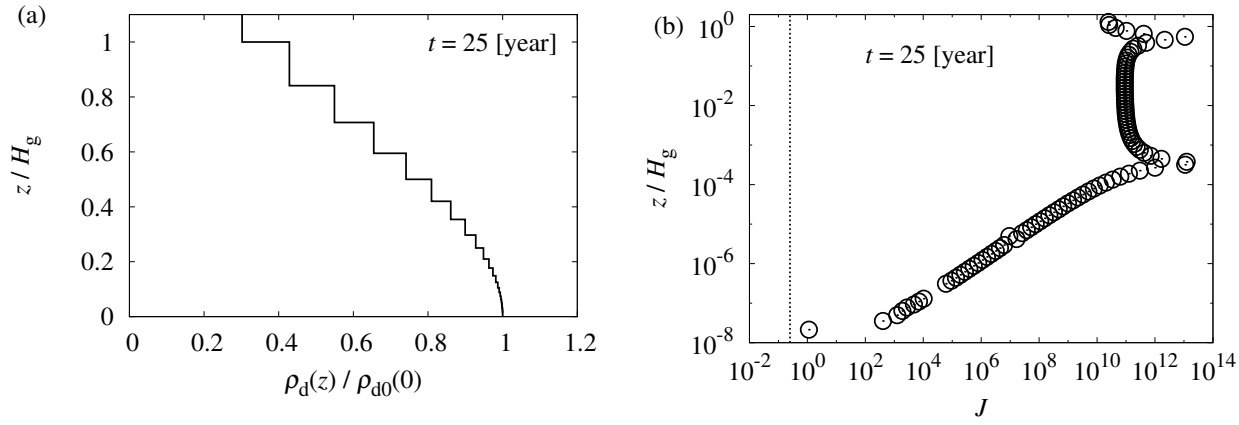

Figure 3.1: (a) The distribution of dust density at $r = 1$ AU and at $t = 25$ yr. The line, the abscissa, and the ordinate show the same as ones of figure 2.2a. (b) The distribution of the Richardson number at $t = 25$ yr. The abscissa shows Richardson number. The ordinate shows z coordinate in units of $H_{\rm g}$. The critical value $J_{\rm c}$ is also drawn (dotted line). This figure was presented in Hasegawa & Tsuribe (2013) as figure 6.

of the dust density, $\partial\rho_{\rm d}(z)/\partial z$. Thus, we focus on $\partial\rho_{\rm d}(z)/\partial z$ and compare the cases with and without dust growth. In order to clarify the effect of dust growth, we first look at the case without the growth of dust aggregates. We consider the case when all dust aggregates have a single size as an initial condition as is the case with dust growth. In the case with single-sized dust aggregates without growth, the typical size of the dust aggregates, $\bar{s}(z)$, which is defined as

$$\bar{s}(z) \equiv \frac{\int_0^\infty s\, mn(m,z)dm}{\int_0^\infty mn(m,z)dm}, \tag{3.1}$$

is equal to s_0, and is independent of z. Garaud and Lin (2004) showed that the time dependence of the dust density profile proceeds in a self-similar manner in the case without the growth of dust aggregates. In this case, the gradient of the dust density is given by

$$\frac{\partial\rho_{\rm d}(z)}{\partial z} = -\frac{2\Sigma_{\rm d} z}{\sqrt{\pi}{H_{\rm d}}^3} \propto z \to 0 \quad (z \to 0). \tag{3.2}$$

In order to compare with the case including the growth of dust aggregates, we consider the mean sedimentation velocity of dust at z, $\bar{v}_z(z)$, which is derived from equations (1.18), (1.44),

and (3.1). At $z/H_{\rm g} \ll 1$ and at $t/t_{\rm sed} \ll 1$, $\bar{v}_z(z)$ is given by

$$\bar{v}_z(z) \equiv -\frac{\rho_{\rm s}}{\rho_{\rm g}(z)} \frac{\bar{s}(z)}{c_{\rm s}} {\Omega_{\rm K}}^2 z. \tag{3.3}$$

In the case without the growth of dust aggregates, $\bar{v}_z(z) \propto z$ at $z/H_{\rm g} \ll 1$, because $\bar{s}(z) = s_0$.

Second, we consider the case with the growth of dust aggregates. In this case, the typical size of dust aggregates, $\bar{s}(z)$, is a linear function of z at $z/H_{\rm g} \ll 1$ and at $t/t_{\rm sed} \ll 1$, owing to collisions due to sedimentation (see the Appendix F for the reason). In such a case, $\bar{v}_z(z)$ has a quadratic term of z because the typical size of dust aggregates is a linear function of z [equation (3.3)]. By comparing the functional form of $\bar{v}_z(z)$ with that in the case without dust growth, at $z/H_{\rm g} \ll 1$ and at $t/t_{\rm sed} \ll 1$, it is suggested that the gradient of the dust density is given by

$$\frac{\partial \rho_{\rm d}(z)}{\partial z} = \delta_1 z + \delta_2 \to \delta_2 \quad (z \to 0), \tag{3.4}$$

where $\delta_1 (< 0)$ and $\delta_2 (> 0)$ are appropriate values.

Figure 3.2 shows the distribution of the gradient of the dust density at $z/H_{\rm g} \ll 1$ and at $t = 25$ yr for cases with and without dust growth. From figure 3.2, it is confirmed that the distribution of the gradient of the dust density can be approximated by equation (3.4) with $\delta_2 > 0$ in the case with dust growth. We can approximate $\partial \rho_{\rm d}(z)/\partial z \simeq [-2.0(z/H_{\rm g}) + 1.0 \times 10^{-5}][\rho_{\rm d0}(0)/H_{\rm g}]$ (figure 3.2). This indicates that the distribution of the dust density has a local maximum value at $z/H_{\rm g} \sim 5 \times 10^{-6}$ in the case with the growth of dust aggregates. This can be confirmed by noting that figure 3.3 that shows the distribution of the dust density in $z/H_{\rm g} \ll 1$ and at $t = 25$ yr in the case with dust growth. By approximating $\rho_{\rm g}(z)$ as $\rho_{\rm g}(0)$ and $\rho_{\rm d}(z)$ as $\rho_{\rm d0}(0)$, the Richardson number for $z/H_{\rm g} \ll 1$ is given by

$$\begin{aligned} J &= \left(\frac{16}{13}\right)^2 \left(\frac{r}{H_{\rm g}}\right)^2 \left(\frac{\Sigma_{\rm g}}{\Sigma_{\rm d}}\right)^{-2} \left(\frac{\Sigma_{\rm g}}{\Sigma_{\rm d}} + 1\right)^3 \\ &\quad \times \frac{z}{H_{\rm g}} \left[\frac{2\Sigma_{\rm g}}{\Sigma_{\rm d}} \frac{z}{H_{\rm g}} - \frac{\partial \rho_{\rm d}(z)}{\partial z} \frac{H_{\rm g}}{\rho_{\rm d0}(0)}\right] \left[\frac{2z}{H_{\rm g}} + \frac{\partial \rho_{\rm d}(z)}{\partial z} \frac{H_{\rm g}}{\rho_{\rm d0}(0)}\right]^{-2} \\ &= 1.7 \times 10^5 \ \tilde{z} \left[4.8 \times 10^2 \ \tilde{z} - \frac{\partial \tilde{\rho}_{\rm d}(\tilde{z})}{\partial \tilde{z}}\right] \left[2 \, \tilde{z} + \frac{\partial \tilde{\rho}_{\rm d}(\tilde{z})}{\partial \tilde{z}}\right]^{-2}, \end{aligned} \tag{3.5}$$

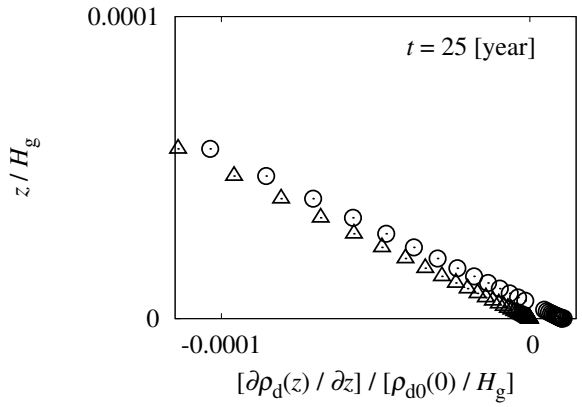

Figure 3.2: Distribution of the gradient of dust density in $r = 1$ AU and $z/H_{\rm g} \ll 1$ at $t = 25$ yr. The abscissa shows the gradient of the dust density $\partial\rho_{\rm d}(z)/\partial z$ in units of $\rho_{\rm d0}(0)/H_{\rm g}$. The ordinate shows z coordinate in units of $H_{\rm g}$. Circles show the case with dust growth, and triangles show that without dust growth. This figure was presented in Hasegawa & Tsuribe (2013) as figure 7.

where $\tilde{z} \equiv z/H_{\rm g}$ and $\tilde{\rho}_{\rm d} \equiv \rho_{\rm d}/\rho_{\rm d0}(0)$. Figure 3.4 shows the distribution of the Richardson number at $z/H_{\rm g} \ll 1$ and at $t = 25$ yr in the case with the growth of dust aggregates. In figure 3.4, it can be seen that the numerical solutions of the Richardson number are sufficiently close to the approximate equation (3.5). Figure 3.4 shows that the Richardson number drawn by the solid line is smaller than the critical value, $J_{\rm c}$, around the midplane at $t = 25$ yr.

However, it is doubtful for KHI to occur. Figure 3.3 shows that the distribution of the dust density has a local maximum value at $z \neq 0$. Under the local maximum point, the Rayleigh-Taylor instability (RTI) is suspected to occur because the distribution of the gradient of total density, $\rho = \rho_{\rm g} + \rho_{\rm d}$, becomes positive near the midplane (Chandrasekhar 1961). If RTI occurs, the distribution of the total density in this region is expected to be adjusted as to be constant (Watanabe & Yamada 2000; Sekiya & Ishitsu 2001). If it is assumed that the growth rate of RTI is larger than that of KHI, and that the distribution of the total density becomes constant around the midplane, the gradient of the total density becomes zero near the midplane. In this case, the Richardson number near the midplane becomes infinite. Then, it is indicated

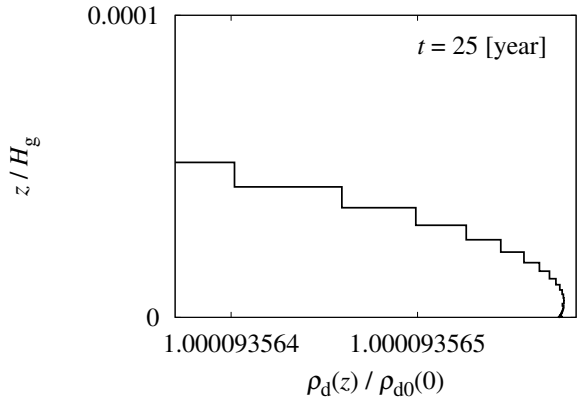

Figure 3.3: Distribution of dust density in $r = 1$ AU and $z/H_{\rm g} \ll 1$ at $t = 25$ yr in the case with the growth of dust aggregates. The line, abscissa, and ordinate show the same situation as in figure 2.2a. This figure was presented in Hasegawa & Tsuribe (2013) as figure 8.

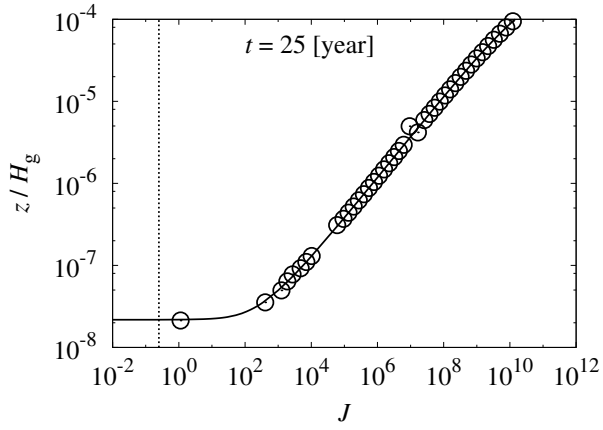

Figure 3.4: Distribution of the Richardson number in $r = 1$ AU and $z/H_{\rm g} \ll 1$ at $t = 25$ yr in the case with growth of dust aggregates. The circles, the dotted line, the abscissa, and the ordinate show the same situation as in figure 3.1b. The solid line is given by equation (3.5). This figure was presented in Hasegawa & Tsuribe (2013) as figure 9.

that KHI does not occur. Thus, below, the possibility of KHI near the midplane in the early phase, as indicated in figure 3.1b, is not considered further.

3.2.2 The Dust Density at the Onset of KHI for the Case with Dust Growth

Figure 3.5 shows the dust density distribution at the onset of KHI in the case with dust growth with $f_{\rm d} = 1$. In figure 3.5a, the distribution of the dust density has a local maximum value at $z = z_{\rm RT} \sim 10^{-3} H_{\rm g}$, and there is a region where the gradient of the dust density becomes positive. As discussed in subsection 3.2.1, in this case, the distribution of the dust density is expected to be adjusted to be constant by RTI in the region $z \lesssim z_{\rm RT}$. Assuming this adjustment by RTI, we modify the distribution of dust density as figure 3.5b with mass conservation. Note that this treatment for RTI is crude, and that a more accurate treatment should be addressed in the future. Hereafter, the same modification is always applied for the density near the midplane.

Figure 3.6 shows the modified dust density at the onset of KHI as a function of the dust abundance parameter. Figure 3.6 corresponds to figure 2.5 with dust growth. Since it is difficult to numerically calculate the case with large $f_{\rm d}$ because of the computer performance, results only for the case with $f_{\rm d} \leq 4$ are plotted. In figure 3.6, it can be seen that dust density at KHI, $\rho_{\rm d,KH}$, increases with increasing the dust abundance parameter, $f_{\rm d}$, for the case with $f_{\rm d} < 2$ as is seen in figure 2.5. On the other hand, in the case with $f_{\rm d} > 2$, the dust density at KHI decreases with increasing dust abundance. These tendencies are qualitatively different from figure 2.5. In figure 3.6, our results show that dust density in the midplane at the onset of KHI for the case with $f_{\rm d} = 4$ is about the same as that for the case with $f_{\rm d} = 1$. As the physical origin of the decline of $\rho_{\rm d,KH}$ for $f_{\rm d} > 2$, we consider the difference in property of gas drag. After dust aggregates grow, the law of gas drag changes from Epstein's law to Stokes' law. Figure 3.7 shows the mass function, where the dust density distribution takes a local

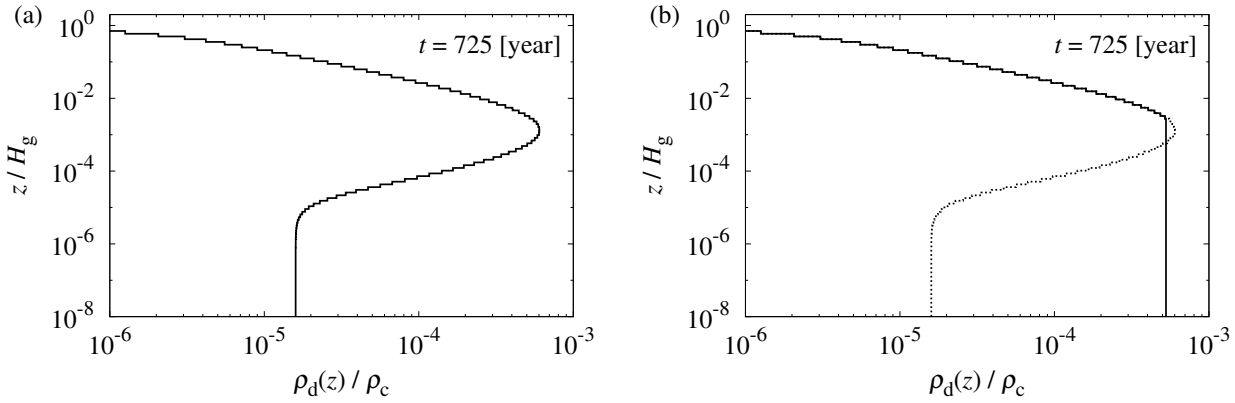

Figure 3.5: Dust density in $r = 1$ AU at the onset of KHI for the case with dust growth and $f_{\rm d} = 1$. (a) Dust density obtained by numerical calculations. (b) Dust density adjusted as to be constant (solid line) and the dust density not adjusted (dotted line). The dust density not adjusted is equal to that obtained by numerical calculations. For both (a) and (b), the abscissas show the dust densities $\rho_{\rm d}(z)$'s in units of $\rho_{\rm c}$, and the ordinates show z coordinates in units of $H_{\rm g}$. This figure was presented in Hasegawa & Tsuribe (2013) as figure 10.

maximum value at the onset of KHI for the case with $f_{\rm d} = 1$ and $f_{\rm d} = 4$, respectively. For the case with $f_{\rm d} = 1$, the mass function has two peaks at $m/m_0 \sim 10^2$ and at $m/m_0 \sim 10^{12}$, and the typical size of dust aggregates, $\bar{s}$ [equation (3.1)], is 0.9 cm. (The mass of dust aggregates with this typical size is about $10^{12} m_0$.) On the other hand, for the case with $f_{\rm d} = 4$, the mass function has two peaks at $m/m_0 \sim 10^2$ and at $m/m_0 \sim 10^{14}$, and the typical size of dust aggregates, $\bar{s}$, is 4 cm. (The mass of dust aggregates with this typical size is about $10^{14} m_0$.) In the case with $s \geq 3l_{\rm g}/2 = 2.2$ cm, the stopping time is given by Stokes' law. By a comparison of these results, it is suggested that the decrease of the dust density at KHI for $f_{\rm d} > 2$ in figure 3.6 originates from a change in the law of gas drag due to dust growth.

To confirm this possibility, for reference, we recalculated sedimentation of dust aggregates with growth using Epstein's law for all sizes. The solids line in figure 3.8 shows the dust density at the onset of KHI, $\rho_{\rm d,KH}$, for this case. It can be clearly seen that the dust density at the onset of KHI, $\rho_{\rm d,KH}$, is large for the large dust abundance parameter, $f_{\rm d}$. By comparing the

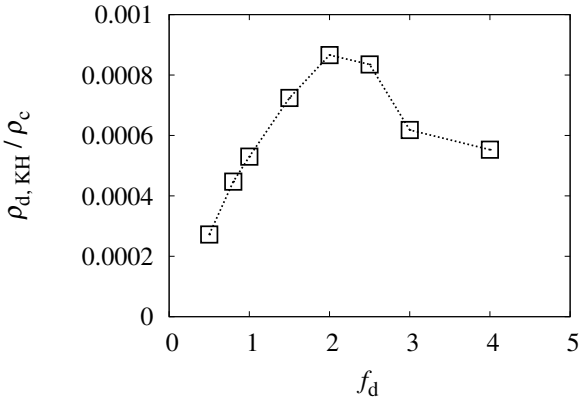

Figure 3.6: Modified dust density in $r = 1$ AU at the onset of KHI for the case with dust growth. The abscissa and the ordinate show the same as situation in figure 2.5. This figure was presented in Hasegawa & Tsuribe (2013) as figure 11.

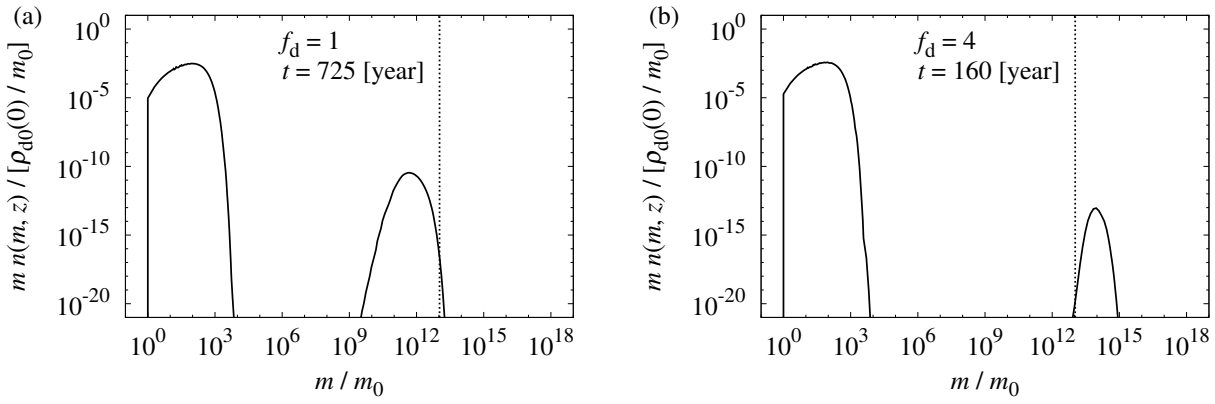

Figure 3.7: (a) Mass function in the case with $f_{\mathrm{d}} = 1$ at $z = 1.5 \times 10^{-3} H_{\mathrm{g}}$ and $r = 1$ AU, where the distributions of the dust density take a local maximum value at the onset of KHI. (b) Mass function in the case with $f_{\mathrm{d}} = 4$ at $z = 3.8 \times 10^{-4} H_{\mathrm{g}}$ and $r = 1$ AU, where the distributions of dust density takes a local maximum value at the onset of KHI. In both diagrams (a) and (b), the abscissa shows the dust mass, m, in units of m_0. The ordinate shows the mass function, $mn(m, z)$, in units of $\rho_{\mathrm{d0}}(0)/m_0$. The dotted lines show the border line, where the stopping time changes from Epstein's law to Stokes' law. This figure was presented in Hasegawa & Tsuribe (2013) as figure 12.

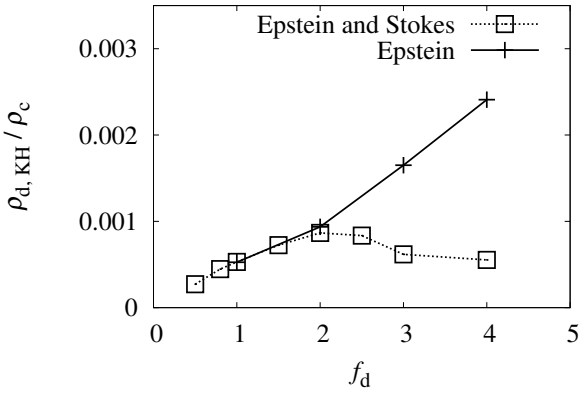

Figure 3.8: Modified dust density in $r = 1$ AU at the onset of KHI for the case with dust growth in cases of using both Epstein's law and Stokes' law (dotted line and squares), and using only Epstein's law for all size (solid line and crosses). The abscissa and the ordinate show the same as ones of figure 2.5. This figure was presented in Hasegawa & Tsuribe (2013) as figure 13.

two lines in figure 3.8, it is clear that the physical origin for the decline of $\rho_{\mathrm{d,KH}}$ for $f_{\mathrm{d}} > 2$ (dotted line) is the change of the gas drag from Epstein's law to Stokes' law. Therefore, it is significant for us to take into account the dust size dependence of the stopping time as well as dust growth when we investigate the shear-driven turbulence in the protoplanetary disk.

3.3 Discussion

3.3.1 Dependence on the Heliocentric Distance

We now estimate the dependence of the required abundance of dust for GI before KHI on the heliocentric distance, r. First, we consider the case without dust growth. For simplicity, we consider the case when all dust aggregates have a single size. The scale height of the dust density profile at the onset of KHI can be obtained from equation (2.7), and we define the scale height as H_{KHI}. By substituting J_{c} and H_{KHI} for $J(z = z_{\mathrm{c}})$ and H_{d} in equation (2.7),

respectively, $H_{\rm KHI}$ is given by

$$H_{\rm KHI} = \left(\frac{8J_{\rm c}}{27}\right)^{1/2} \eta r = 1.0 \times 10^{-2} H_{\rm g} \left(\frac{r}{1[{\rm AU}]}\right)^{1/4}. \tag{3.6}$$

Equation (3.6) shows that $H_{\rm KHI}$ is independent of $f_{\rm d}$. The dependence of $H_{\rm c}$ [defined in equation (2.4)] on r is given by $H_{\rm c} = 1.6 \times 10^{-5} f_{\rm d}\, \xi_{\rm ice}\, H_{\rm g} (r/1\ [{\rm AU}])^{1/4}$, and we have

$$\frac{H_{\rm KHI}}{H_{\rm c}} = 6.6 \times 10^2 \left(\frac{f_{\rm d}}{1}\right)^{-1} \left(\frac{\xi_{\rm ice}}{1}\right)^{-1}. \tag{3.7}$$

The parameter of condensed water ice, $\xi_{\rm ice}$, is given by 1 (at $r < 2.7$ AU) or 4.2 (at $r > 2.7$ AU) (Hayashi 1981). Equation (3.7) shows the possibility that the required abundance of dust for GI before KHI is smaller outside the snow line than inside. Next, we consider the case with dust growth. At the onset of KHI, most of the dust aggregates with the typical size calculated in subsection 3.2.2 [defined in equation (3.1)] have settled near the midplane. Thus, the typical size of dust at the onset of KHI can be obtained as the size of dust aggregates that have settled from high altitudes to the midplane. We have $dm = 4\pi s^2 \rho_{\rm s} ds \sim -\pi (2s)^2 \rho_{\rm d} dz$. Assuming that $s = s_0$ at $z = +\infty$ and that $s = s_{\rm f} \gg s_0$ at $z = 0$, we derive $s_{\rm f}$ as

$$s_{\rm f} \sim \frac{\Sigma_{\rm d}}{2\rho_{\rm s}} \sim \left(\frac{f_{\rm d}}{1}\right) \left(\frac{\xi_{\rm ice}}{1}\right) \left(\frac{r}{1[{\rm AU}]}\right)^{-3/2} [{\rm cm}]. \tag{3.8}$$

The typical sizes of dust at the onset of KHI calculated in subsection 3.2.2 were 0.9 cm and 4 cm in the case with $f_{\rm d} = 1$ and $f_{\rm d} = 4$, respectively, and consistent with equation (3.8). Equation (3.8) shows that the typical size of dust at the onset of KHI is smaller for larger r. On the other hand, the mean free path of gas molecules scales as $l_{\rm g} \propto {\rho_{\rm g}}^{-1} \propto H_{\rm g} {\Sigma_{\rm g}}^{-1} \propto r^{11/4}$, and $l_{\rm g}$ is larger for larger r. Thus, the gas drag force tends to be given by Epstein's law in the outer region of a protoplanetary disk, even for a large $f_{\rm d}$. The solid line in figure 3.8 shows that the dust density at the onset of KHI is larger for larger $f_{\rm d}$ in the Epstein regime. Therefore, the outer region of the protoplanetary disk might be more suitable for GI than the inner region.

The above discussion is different from that in Takeuchi et al. (2012), which shows that the inner part of the protoplanetary disk is more suitable for GI. They are based on a different

condition from ours. They used the scale height of the dust layer, which is determined by the balance between sedimentation and the diffusion of dust aggregates, while we used the scale height of the dust density profile at the onset of KHI.

3.3.2 Treatment for Rayleigh-Taylor instability

In this chapter, we took into account the effect of RTI. However, the treatment for RTI used in this chapter was crude, and the detail of convection induced by RTI did not take into account. In future work, we should address a more accurate treatment for RTI in the case with multi-sized dust with growth.

3.3.3 Possibilities of the Streaming Instability

Youdin & Goodman (2005) and Johansen & Youdin (2007) showed that the dynamics in the midplane is dominated by the streaming instability (SI). Bai & Stone (2010) showed that dust aggregates with $\tau_{\rm s} \equiv \Omega_{\rm K} t_{\rm stop} > 0.01$ trigger SI before KHI. In our model, at $r = 1$ AU, $\tau_{\rm s} > 0.01$ corresponds to $s > 2$ cm. In our calculations, for the case with dust growth and $f_{\rm d} > 2$, the typical size of dust aggregates at the maximum density is larger than 2 cm. Therefore, in the dust layer governed by Stokes' law, SI would occur before KHI and GI. If SI occurs, it is expected that dust aggregates accumulate toward dense regions of dust. Then, dense clumps of dust aggregates form in the disk (Johansen & Youdin 2007). In the dense clumps, dust abundance is much larger than the MMSN model. In future work, we should address SI in the case with multi-sized dust with growth.

3.3.4 Possibility after Kelvin-Helmholtz Instability

In this chapter, we found that KHI tends to occur before GI even in the case with large dust abundance during sedimentation with dust growth. This result suggests that small dust aggregates tend to be suffered from stirring up by shear-driven turbulence induced by KHI during

their sedimentation at least once. However, this suggestion does not exclude the possibility for GI. If dust aggregates have larger collisional velocities owing to the shear-driven turbulence than owing to sedimentation and radial drift, dust aggregates have the possibility to grow quickly or fragment. If the dust size distribution becomes a quasi-equilibrium distribution as a result of iterations of collisional growth and fragmentation of dust, then the state may be similar to that in the case with multi-sized dust aggregates without growth. Then, GI might occur in the case with large dust abundance. However,it is not known if the quasi-equilibrium size distribution of dust aggregates arises. To understand this possibility, we must take account of dust-dust collisions with shear-driven turbulence induced by KHI. In future work, we will study this possibility.

3.4 Summary

In the case with dust growth, the dust density at the onset of KHI decreases for increasing dust abundance for $f_{\rm d} > 2$. This result is qualitatively different from that in the case without dust growth. The reason is that gas drag changes from Epstein's law to Stokes' law for larger dust aggregates that grow up in advance. Thus, we stress that, for studying of shear-driven turbulence, the change of the law of gas drag from Epstein's law to Stokes' law as well as dust growth is required to be taken into account.

For the formation of planetesimals, it has been suggested in the literature that in order to occur GI before an inward drift of dust, dust aggregates have to settle toward the midplane, and it is suggested to be possible with large dust abundance. However, in this thesis, it is concluded that KHI tends to occur before GI even in the case with large dust abundance during sedimentation with dust growth. This result suggests that small dust aggregates tend to be suffered from stirring up by shear-driven turbulence induced by KHI during their sedimentation at least once. However, this conclusion does not exclude the possibility for GI. If dust aggregates have larger collisional velocities owing to the shear-driven turbulence than

owing to sedimentation and radial drift, dust aggregates have the possibility to grow quickly or fragment. This effect was not included in this thesis. To understand this possibility, we must take account of dust-dust collisions under the condition with shear-driven turbulence induced by KHI. In future work, we should develop a more realistic model by calculating the effect of KHI, RTI and SI directly.

Chapter 4

Validity of the Classical RNC

In chapter 2 and 3, in order to investigate dust densities in the midplane at the onset of KHI, we used the classical Richardson number criterion (RNC) (Chandrasekhar 1961). However, as described in subsection 1.5.4, the classical RNC is not ensured to discuss KHI in the protoplanetary disk.

In this chapter, we discuss the validity of the classical RNC. To that end, we directly perform the linear stability analysis for KHI. The growth rate of KHI is calculated using the linear stability analysis in order to detect instability with the dust density distribution consistent with dust sedimentation, and the dust density required for GI before KHI is calculated. By comparing the result estimated by the linear stability analysis for the onset of KHI with that estimated by the classical RNC, we discuss the validity of the classical RNC.

For simplicity, we consider multi-sized dust but neglect dust growth in this chapter.

This chapter is mainly based on our paper, Hasegawa & Tsuribe (2014).

4.1 Models and Equations

In this chapter, we investigate the stability for the series of the density distribution induced by sedimentation. Actually, the stability analysis with the time-dependent evolution of the

dust density can not be reduced to the eigenvalue problem. However, in this chapter, density distributions for each instant of time are approximated as quasi-equilibrium distributions since we assume in subsection 4.1.1 that dust sedimentation is significantly slow. In such a case, the dust density profile evolves in a self-similar manner with single-sized dust without growth (Garaud & Lin 2004). On the other hand, in the case with multi-sized dust, the dust density profile is not self-similar during dust sedimentation as described in section 2.3.

In this chapter, we perform the linear stability analysis for KHI. In this section, we present the models of the unperturbed state and the linear perturbation equation.

4.1.1 Models of Unperturbed State

In this thesis, we assume that the mass of the central star is given by $1M_\odot$. As is the case with chapter 2, we neglect the radial motion of dust aggregates and we set $r = 1$ AU for simplicity. We assume that the unperturbed quantities are axisymmetric with respect to the rotational axis of the disk and are symmetric with respect to the midplane of the disk. In this chapter, we adopt the local Cartesian coordinate system (x, y, z) at $r = 1$ AU rotating around the central star with the azimuthal velocity $(1 - \eta)v_{\rm K}$ (Sekiya & Ishitsu 2000). The gas surface density, $\Sigma_{\rm g}$, the dust surface density, $\Sigma_{\rm d}$ and temperature, T, are assumed to be equations (1.2), (1.6) and (1.5), respectively. The sound velocity, $c_{\rm s}$, is given by equation (1.7). For simplicity, we assume that the gas density is uniform in the dust layer because the dust layer is geometrically thin and that $\rho_{\rm g}(z) = \rho_{\rm g}(0)$ at any z. Then, the gas density is assumed as

$$\rho_{\rm g} = \frac{\Sigma_{\rm g}}{\sqrt{\pi} H_{\rm g}} = 1.4 \times 10^{-9} \, [{\rm g \, cm^{-3}}]. \tag{4.1}$$

The scale height of the disk, $H_{\rm g}$, is given by equation (1.10), and $H_{\rm g} = 4.7 \times 10^{-2}$ AU. The value of η is given by equation (1.14). For simplicity, we assume $(r^2 + z^2)^{1/2} \simeq r$ and $\partial \Omega_{\rm K} / \partial z = 0$. We assume that all dust aggregates are so small that the stopping time is always given by equation (1.15) and that $t_{\rm stop} \Omega_{\rm K} \ll 1 \ll t_{\rm sed} \Omega_{\rm K}$ from equations (1.15) and (1.19). For the revolutions of gas and dust, we treat the mixture of gas and dust as one component fluid, and

the unperturbed azimuthal velocity of mixed fluid of gas and dust is given as

$$v_0 = \left(1 - \frac{\rho_{\rm g}}{\rho_0}\right) \eta v_{\rm K}, \tag{4.2}$$

where v_0 is the unperturbed azimuthal velocity of the mixed fluid of gas and dust and $\rho_0 \equiv \rho_{\rm g} + \rho_{\rm d0}(z)$, where $\rho_{\rm d0}(z)$ is the unperturbed dust density. In this chapter, subscript 0 refers the unperturbed quantities, and subscript 1 refers the perturbed quantities. Equation (4.2) corresponds to equation (1.28) with $\rho = \rho_0$.

We adopt the initial dust density distribution that is the same as the unperturbed dust density distribution in Sekiya & Ishitsu (2001), and that is given by

$$\rho_{\rm d0}(z) = \begin{cases} (\rho_{\rm ini}/2)\left[1 + \cos\left(\pi z/z_{\rm d}\right)\right] & (|z| < z_{\rm d}) \\ 0 & (|z| \geq z_{\rm d}) \end{cases}, \tag{4.3}$$

where $z_{\rm d}$ is the time dependent scale height of the dust density profile with $z_{\rm d} = H_{\rm g}$ at the initial state, and $\rho_{\rm ini}$ is the initial dust density at the midplane and is given by

$$\rho_{\rm ini} = \frac{\Sigma_{\rm d}}{H_{\rm g}}. \tag{4.4}$$

We consider $N_{\rm d}$ kinds of sizes (radii) for dust aggregates. In this case, the dust density distribution $\rho_{\rm d0}(z)$ is given by

$$\rho_{\rm d0}(z) = \sum_{i=1}^{N_{\rm d}} \rho_{{\rm d0},\, s_i}(z), \tag{4.5}$$

where $\rho_{{\rm d0},\, s_i}(z)$ is the density of dust component with size s_i at z. Equation (4.5) corresponds to equation (2.9) with $\rho_{\rm d} = \rho_{\rm d0}$ and $\rho_{{\rm d},\, s_i} = \rho_{{\rm d0},\, s_i}$. For simplicity, we assume that the initial size distribution is given by

$$\rho_{{\rm d0},\, s_i}(z) = \rho_{{\rm d0},\, s_{\rm min}}(z) = \frac{\rho_{\rm d0}(z)}{N_{\rm d}}, \tag{4.6}$$

where $s_{\rm min}$ is the minimum size of dust aggregates. Equation (4.6) corresponds to equations (2.13) and (2.14) with $\rho_{\rm d} = \rho_{\rm d0}$ and $\rho_{{\rm d},\, s_i} = \rho_{{\rm d0},\, s_i}$. In this case, $\rho_{{\rm d0},\, s_i}(z)$ is given by

$$\rho_{{\rm d0},\, s_i}(z) = \begin{cases} (\rho_{\rm ini}/2N_{\rm d})(H_{\rm g}/z_{{\rm d},\, s_i})\left[1 + \cos\left(\pi z/z_{{\rm d},\, s_i}\right)\right] & (|z| < z_{{\rm d},\, s_i}) \\ 0 & (|z| \geq z_{{\rm d},\, s_i}) \end{cases}, \tag{4.7}$$

where $z_{\mathrm{d},\,s_i}$ is the scale height of the dust density profile for dust with size s_i, and $z_{\mathrm{d},\,s_i}$ is derived as

$$\frac{z_{\mathrm{d},\,s_i}}{H_{\mathrm{g}}} = \left(\frac{z_{\mathrm{d},\,s_{\mathrm{min}}}}{H_{\mathrm{g}}} \right)^{s_i/s_{\mathrm{min}}}, \tag{4.8}$$

where $z_{\mathrm{d},\,s_{\mathrm{min}}}$ is the scale height of the dust density profile for minimum dust aggregates. The symbol $z_{\mathrm{d},\,s_{\mathrm{min}}}$ corresponds to z_{d} [equation (4.3)]. Equation (4.8) corresponds to equation (2.11) with $H_{\mathrm{d},\,s_i} = z_{\mathrm{d},\,s_i}$. We assume $N_{\mathrm{d}} = 11$ since we checked that the dependence of dust density at the onset of KHI estimated by the classical RNC on dust abundance is affected by the dust size distribution in the case with $N_{\mathrm{d}} \gtrsim 2$. We assume that s_i is given by s_{min}, $1.1 s_{\mathrm{min}}$, $1.2 s_{\mathrm{min}}$, ..., and $2 s_{\mathrm{min}}$. If the values of f_{d} and $z_{\mathrm{d},\,s_{\mathrm{min}}}$ are given, the dust density distribution $\rho_{\mathrm{d}0}(z)$ is obtained from equations (1.6), (4.4), (4.5), (4.7) and (4.8).

As described in subsection 2.3.1, the results shown in this chapter are independent of the size of individual dust aggregates, s_i, provided that the time scale is renormalized, and are dependent on the size ratio, s_i/s_{min}, as long as the stopping time is given by Epstein's law [equation (1.15)].

For comparison for the onset of KHI, we calculate the Richardson number given by

$$J = -\frac{g_z}{\rho_0} \frac{\partial \rho_{\mathrm{d}0}(z)}{\partial z} \left(\frac{\partial v_0}{\partial z} \right)^{-2}, \tag{4.9}$$

where $g_z = {\Omega_{\mathrm{K}}}^2 z$. For simplicity, we adopt $J_{\mathrm{c}} = 0.25$. Equation (4.9) corresponds to equation (1.47) with $v_\phi = v_0$, $\rho = \rho_0$ and $\partial \rho_{\mathrm{g}}/\partial z = 0$. From equations (4.2) and (4.9), we obtain

$$J = -\frac{z}{\eta^2 r^2} \frac{{\rho_0}^3}{{\rho_{\mathrm{g}}}^2} \left[\frac{\partial \rho_{\mathrm{d}0}(z)}{\partial z} \right]^{-1}. \tag{4.10}$$

Equation (4.10) corresponds to equation (2.15) with $\rho = \rho_0$.

4.1.2 Linear Perturbation Equation

We calculate the growth rate of KHI for the case with the unperturbed dust density described in subsection 4.1.1. To calculate the growth rate, we solve the linear perturbation equation

derived by Sekiya & Ishitsu (2000). Perturbed quantities are assumed to have the form as $F_1 = \hat{F}_1(z)\exp[i(ky - \omega t)]$, where k is the azimuthal wave number, y is the azimuthal coordinate, and $\omega = \omega_r + i\omega_i$ is the complex angular frequency. For perturbed quantities, we restrict ourselves to the case with the radial wave number to be zero because this is the most unstable mode. Hereafter $\hat{}$ is omitted, and the perturbation equation is given by

$$\frac{d^2 w_1}{dz^2} + \frac{1}{\rho_0}\frac{d\rho_0}{dz}\frac{dw_1}{dz} - \left(k^2 + \frac{1}{\bar{v}}\frac{d^2 v_0}{dz^2} + \frac{1}{\rho_0}\frac{d\rho_0}{dz}\frac{1}{\bar{v}}\frac{dv_0}{dz} + \frac{{\Omega_{\rm K}}^2 z}{\bar{v}^2}\frac{1}{\rho_0}\frac{d\rho_0}{dz}\right) w_1 = 0, \tag{4.11}$$

where w_1 is the perturbed vertical velocity, and $\bar{v} \equiv v_0 - \omega/k$. Boundary conditions at the midplane of the disk, i.e., at $z = 0$ are given by

$$w_1 = 0 \text{ at } z = 0 \text{ (odd mode)}, \tag{4.12}$$

and

$$\frac{dw_1}{dz} = 0 \text{ at } z = 0 \text{ (even mode)}. \tag{4.13}$$

Boundary condition at the boundary surface between the dust layer and the gas layers, i.e., at $z = z_{\rm d}$ is given by

$$\frac{dw_1}{dz} + \left(k - \frac{1}{\bar{v}}\frac{dv_0}{dz}\right) w_1 = 0 \text{ at } z = z_{\rm d}. \tag{4.14}$$

We present the detailed derivation of the linear perturbation equation (4.11) and the boundary conditions in the Appendix G.

In order to solve the linear perturbation equation (4.11), we assume the dust abundance parameter, $f_{\rm d}$, the azimuthal wave number, k, and the dust density at the midplane, $\rho_{\rm d0}(0)$. Then, we can solve the linear perturbation equation (4.11) numerically with the boundary condition (4.14) for the odd mode (4.12) and the even mode (4.13), respectively. At fixed dust abundance, $f_{\rm d}$, and the dust density, $\rho_{\rm d0}(0)$, we obtain eigenvalues, ω_r and ω_i, as functions of the wave number, k, respectively. At fixed dust abundance, $f_{\rm d}$, the maximum growth rate, $\omega_{i,\max}$, is given by a function of the dust density. Especially, we regard the minimum dust density for $\omega_{i,\max} \geq 0$ as the possible dust density reachable without KHI, then the possible dust density at the midplane, $\rho_{\rm d0}(0)$, is finally derived as a function of dust abundance, $f_{\rm d}$.

In this chapter, we compare the following two cases. The case with single-sized dust without the size distribution is labeled with A, and the case with multi-sized dust with the size distribution is labeled with B.

4.2 Results and Discussion

It is found that even modes are more unstable than odd modes except for two cases: case B with $f_{\rm d} = 1$ and $\rho_{\rm d0}(0) < 0.33\rho_{\rm g}$, and case B with $f_{\rm d} = 2$ and $\rho_{\rm d0}(0) < 0.61\rho_{\rm g}$.

Figure 4.1 shows the maximum growth rates of KHI as functions of the dust density at the midplane. From Figure 4.1, the crossing point of each line with $\omega_{i,\rm max} = 0$ is the possible dust density attained before KHI. As seen in Figure 4.1, it is seen that the dust density in the case with $\omega_{i,\rm max} = 10^{-3}\Omega_{\rm K}$ approximates the dust density in the case with $\omega_{i,\rm max} = 0$. Since it is technically difficult to calculate the case with exactly $\omega_{i,\rm max} = 0$ especially in the case with the large dust abundance parameter $f_{\rm d}$, we use the dust density for $\omega_{i,\rm max} = 10^{-3}\Omega_{\rm K}$ instead of that for $\omega_{i,\rm max} = 0$ except for case B with $f_{\rm d} = 1$ and B with $f_{\rm d} = 2$. For the two cases B with $f_{\rm d} = 1$ and B with $f_{\rm d} = 2$, we use the dust density for $\omega_{i,\rm max} = 10^{-5}\Omega_{\rm K}$ instead of that for $\omega_{i,\rm max} = 0$.

Figure 4.2 shows dust densities in the midplane as functions of dust abundance. A label A-J refers the case A (with single-sized dust) with $J_{\rm min} = 0.25$, a label A-ω_i refers the case A with $\omega_{i,\rm max} = 10^{-3}\Omega_{\rm K}$, a label B-J refers the case B (with multi-sized dust) with $J_{\rm min} = 0.25$, and a label B-ω_i refers the case B with $\omega_{i,\rm max} = 10^{-5}\Omega_{\rm K}$ (case B-1) or $\omega_{i,\rm max} = 10^{-3}\Omega_{\rm K}$ (other cases). From Figure 4.2, it is found that for both cases A and B the dust abundance parameters significantly coincide between the cases with $\omega_{i,\rm max} \sim 0$ and with $J_{\rm min} = 0.25$. Especially, the dust density at the midplane $\rho_{\rm d0}(0)$ in the case B-ω_i with $f_{\rm d} \leq 20$ remarkably coincides with that in the case B-J, and the dotted and solid lines look like overlapping.

In Figure 4.2, it is seen that dust abundance parameters required to achieve $\rho_{\rm d0}(0)/\rho_{\rm c} = 1$ for the case with $J_{\rm min} = 0.25$ are $f_{\rm d} = 2.5 \times 10^3$ in the case A-J and $f_{\rm d} = 74$ in the case B-J.

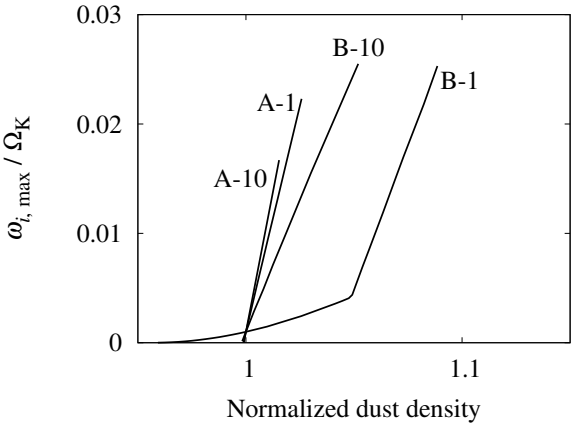

Figure 4.1: Maximum growth rates of KHI $\omega_{i,\mathrm{max}}$ normalized by the Keplerian angular velocity Ω_K as functions of the dust density at the midplane normalized by that in the case with $\omega_{i,\mathrm{max}} = 10^{-3}\Omega_\mathrm{K}$. A-1 means the case A with $f_\mathrm{d} = 1$, A-10 means the case A with $f_\mathrm{d} = 10$, B-1 means the case B with $f_\mathrm{d} = 1$, and B-10 means the case B with $f_\mathrm{d} = 10$. This figure was presented in Hasegawa & Tsuribe (2014) as figure 1.

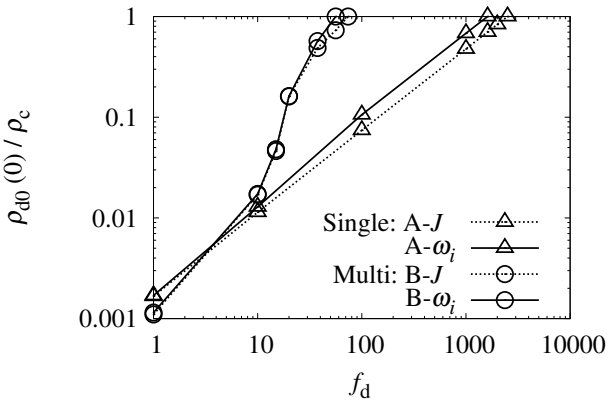

Figure 4.2: Dust densities at the midplane $\rho_{\mathrm{d}0}(0)$ normalized by the critical density for GI ρ_c as functions of the dust abundance parameter f_d for the cases A (triangles) and B (circles). Dotted lines show the densities with the minimum value of the Richardson number distribution $J_\mathrm{min} = 0.25$. Solid lines show the densities with the maximum growth rate of KHI $\omega_{i,\mathrm{max}} = 10^{-5}\Omega_\mathrm{K}$ (case B-1) or $10^{-3}\Omega_\mathrm{K}$ (other cases). This figure was presented in Hasegawa & Tsuribe (2014) as figure 2.

On the other hand, in the case with $\omega_{i,\max} \sim 0$, it is seen that dust abundance parameters required for $\rho_{\rm d0}(0)/\rho_{\rm c} = 1$ are $f_{\rm d} = 1.6 \times 10^3$ in the case A-ω_i and $f_{\rm d} = 56$ in the case B-ω_i. In above results, values of dust abundance parameters $f_{\rm d}$ are larger than values in chapter 2 that are $f_{\rm d} = 6.6 \times 10^2$ in the case A-J and $f_{\rm d} < 50$ in the case B-J. This is because the initial dust density distribution in this chapter is different from the Gaussian profile used in chapter 2. From equation (4.10), the Richardson number distribution depends strongly on the dust density profile, so dust abundance required for GI varies with the initial dust density distribution even with the same $J_{\rm min}$.

In figure 4.2, it is found that dust abundance parameters required to achieve $\rho_{\rm d0}(0)/\rho_{\rm c} = 1$ in the case with multi-sized dust is much smaller than these in the case with single-sized dust. This tendency is similar to the result in chapter 2. We suggest the possibility that this tendency is independent on the initial distribution of the dust density.

In summary, it is found that, for both cases with single-sized dust and with multi-sized dust, the dust abundance parameters significantly coincide between the cases with $\omega_{i,\max} \sim 0$ and with $J_{\rm min} = 0.25$ within a factor of 2. Thus, it is seen that dust abundance parameters that we calculated in chapter 2 using the classical RNC are reasonable within a factor of 2.

From figure 4.2, for both cases with single-sized dust and with multi-sized dust, dust densities at the onset of KHI calculated by $\omega_{i,\max} \sim 0$ are well in accord with those calculated by $J_{\rm min} = 0.25$ in the cases with $f_{\rm d} < 10$. This result suggests that the classical RNC is safely used in the case with dust growth as in chapter 3. We should confirm this possibility using more cases in future work.

For the case with fixed $f_{\rm d}$ and $\omega = \omega_{i,\max}$, we calculate the spatial profile of a Richardson number as a function of z. Then we name the minimum value of the Richardson number in this profile as the critical Richardson number. Figure 4.3 shows the critical Richardson numbers in the case with $\omega_{i,\max} = 10^{-5}\Omega_{\rm K}$ (cases B-1 and B-2) or $\omega_{i,\max} = 10^{-3}\Omega_{\rm K}$ (other cases) as functions of the dust abundance parameter, $f_{\rm d}$. For the case A (with single-sized dust), the critical Richardson number tends to decrease with increasing the dust abundance parameter,

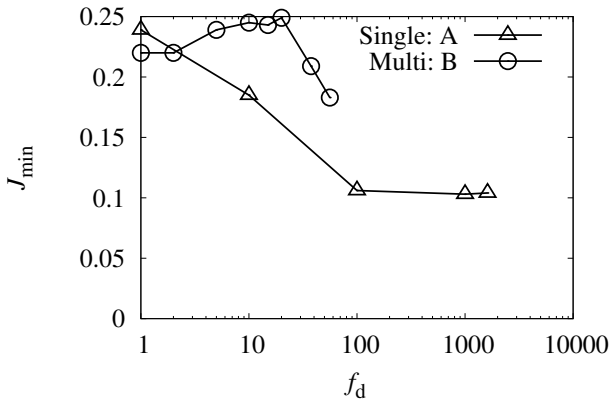

Figure 4.3: Minimum Richardson numbers in the case with $\omega_{i,\max} = 10^{-5}\Omega_{\rm K}$ (cases B-1 and B-2) or $\omega_{i,\max} = 10^{-3}\Omega_{\rm K}$ (other cases) as functions of the dust abundance parameter $f_{\rm d}$ for the case A (triangles) and for the case B (circles). This figure was presented in Hasegawa & Tsuribe (2014) as figure 3.

$f_{\rm d}$. On the other hand, for the case B (with multi-sized dust), the critical Richardson number tends to increase with the dust abundance parameter, $f_{\rm d}$, in the case with $f_{\rm d} \leq 20$ and to approach 0.25 in the case with $5 \leq f_{\rm d} \leq 20$. This result is different from that in the case A. From these results for multi-sized dust, the critical Richardson number is approximated by 0.25, and $J_{\rm min} = 0.25$ condition is applicable in the case with $5 \lesssim f_{\rm d} \lesssim 20$.

The Coriolis and tidal forces are not included in the linear perturbation equation (4.11). Ishitsu & Sekiya (2003) performed the linear stability analysis including these forces and found that the tidal force plays an important role in the stabilization. However, as a first step to focus on the effect of the dust size distribution, in this thesis we ignore the Coriolis and tidal forces for simplicity.

4.3 Summary

In this chapter, we have calculated the growth rate of the Kelvin-Helmholtz instability using the dust density distribution that is consistent with sedimentation of dust aggregates without

growth. We assumed the thin dust layer and the uniform gas density. Dust aggregates were assumed to be small, and the mixture of gas and dust aggregates was treated as one component fluid. We considered the dust size distribution without the dust growth. We have solved the linear perturbation equation to calculate the growth rate, and we have examined the dust abundance required for the gravitational instability of the dust layer before KHI.

Our study shows the following results: (1) For the dust abundance required for the gravitational instability, in the both cases with single- and multi-sized dust, the dust abundance for the case with $\omega_{i,\max} \sim 0$ is about the same as that derived by the condition $J_{\min} = 0.25$. Thus, it is seen that dust abundance parameters calculated in chapters 2 and 3 using the classical Richardson number criterion, $J_{\min} = J_{\rm c} = 0.25$, are reasonable within errors of a factor of 2. (2) The critical Richardson number is affected by the dust size distribution. In the case with single-sized dust, the critical Richardson number tends to decrease with increasing dust abundance. On the other hand, in the case with multi-sized dust, the critical Richardson number tends to increase and approach 0.25 with increasing dust abundance in the case with $5 \lesssim f_{\rm d} \lesssim 20$. Thus, it is indicated that $J_{\min} = 0.25$ condition is applicable in the case with multi-sized dust with $5 \lesssim f_{\rm d} \lesssim 20$.

Chapter 5

Summary and Future Prospects

5.1 Summary

In this thesis, we have investigated the possibility of the onset of the Kelvin-Helmholtz instability (KHI) during dust sedimentation in the protoplanetary disk. Since property of KHI strongly depends on the dust density profile, in order to understand correct outcome after dust sedimentation correctly, it is important to consider appropriate density distribution with sedimentation and growth of dust. However, previous works did not take into account the appropriate distribution of dust density, which is consistent with their sedimentation and growth. In this thesis, we consider the KHI based on the dust density distributions that are consistent with their growth and sedimentation.

In order to clarify the effects of dust growth, we first considered the cases without dust growth to compare with the case with dust growth. As cases without dust growth, we considered two cases: the case with the single-sized dust and the case with the multi-sized dust. As the condition for the onset of KHI, we used the classical Richardson number criterion (RNC) by which KHI occurs when the Richardson number is less than 0.25. As a result, it was found that the gravitational instability (GI) of the settled dust layer tends to occur before the onset of KHI if the dust abundance is larger than $\sim$ 1000 times (for the single-sized dust) or $\sim$ 100

times (for the multi-sized dust) that in the minimum mass solar nebula model. This result shows that, in the multi-sized dust, the dust abundance required for GI is much smaller than that in the single-sized dust. In the case with single-sized dust, the dust density profile has a characteristic scale. In the case with multi-sized dust, on the other hand, the characteristic scale is diffused out to produce more stabilized profile. Thus, in the case with multi-sized dust aggregates, the required abundance of dust for GI has a possibility to be smaller than that in the case with single-sized dust aggregates.

Next, we considered the case with dust growth. In this case, although dust has the continuous size distribution, with dust growth, we find numerically that KHI tends to occur before GI even in the case with large dust abundance. The reason of this qualitative change is found to originate from the change of gas drag law from Epstein's law to Stokes' law owing to dust growth. Thus, we stress that, in the study of shear-driven turbulence, the change of the law of gas drag from Epstein's law to Stokes' law, as well as dust growth, is required to be taken into account, although none of previous works on the KHI in the protoplanetary disk has.

In the above investigation, we used the classical RNC with a constant critical value, 0.25, which is not ensured to discuss KHI for general cases in the protoplanetary disk. We directly performed the linear stability analysis for KHI to discuss the validity of the classical RNC. For the dust density distribution consistent with dust sedimentation, the growth rates of KHI were calculated, and the dust density required for GI before KHI was clarified. By comparing the result estimated by the linear stability analysis with that estimated by the classical RNC, we found that dust density estimated from the linear stability analysis agreed well with that estimated by the classical RNC within errors of a factor of 2. Especially, it is found that the classical RNC tended to be more applicable in the case with the multi-sized dust than in the case with the single-sized dust. These results suggest the possibility that the classical RNC is useful even for the case with dust growth.

The main conclusion of the present thesis is that KHI tends to occur before GI even in the case with large dust abundance during sedimentation of growing dust aggregates in the

protoplanetary disk. This means that small dust aggregates with growth tend to be suffered from stirring up by shear-driven turbulence induced by KHI during their sedimentation at least once. However, this conclusion does not exclude the possibility for GI. If dust aggregates have larger collisional velocities owing to the shear-driven turbulence than owing to sedimentation and radial drift, dust aggregates have the possibility to grow quickly or fragment. This effect was not included in this thesis. To understand this possibility, we will have to take account of dust-dust collisions under the condition with shear-driven turbulence induced by KHI.

5.2 Future Prospects

To take account of dust-dust collisions with shear-driven turbulence induced by KHI, we should develop a more realistic model by calculating the effect of KHI directly. Then, we have to address the non-linear growth of KHI numerically in the future work.

Other than dust-dust collisions in shear-driven turbulence, there are many effects neglected in this thesis. In this thesis, dusts were assumed to be compact and to have a spherical shape. However, since dusts grow due to dust-dust collisions, large dusts are aggregates of small dusts. Both laboratory and numerical experiments showed that aggregates are not at all compact and spherical, but have a fluffy structure (Wurm & Blum 1998; Kempf et al. 1999; Okuzumi et al. 2009). With the same mass, the size of the fractal aggregate is larger than the size of the compact and spherical dust aggregate and varies with the porosity of the aggregate. Therefore, the time evolutions of porosity during the growth of dust aggregates are essential to investigate dust sedimentation, time scale of dust growth and motion of dust aggregates stirred up. We will address this effect in the future work.

We neglected the streaming instability (Youdin & Goodman 2005; Johansen & Youdin 2007). Bai & Stone (2010) showed that dust aggregates with $\tau_{\rm s} \equiv \Omega_{\rm K} t_{\rm stop} > 0.01$ trigger a streaming instability before KHI. In our model, at $r = 1$ AU, $\tau_{\rm s} > 0.01$ corresponds to $s > 2$ cm. In our calculations, for the case with dust growth and $f_{\rm d} > 2$, the typical size of dust

aggregates at the maximum density is larger than 2 cm. Therefore, in the dust layer governed by Stokes' law, the streaming instability would occur before KHI and GI. We will address this problem in the future work.

Appendix A

Toomre's Stability Criterion

We present the linear analysis of local stability of an infinitely thin, rotating disk (Toomre 1964; Binney & Tremaine 1987). We consider that the disk is composed of ideal fluid and is axisymmetric with respect to the rotational axis of the disk. We consider that there is no motion perpendicular to the disk. The governing equations are given as

$$\frac{\partial \Sigma}{\partial t} + \nabla \cdot (\Sigma \mathbf{v}) = 0, \tag{A.1}$$

$$\frac{\partial \mathbf{v}}{\partial t} + (\mathbf{v} \cdot \nabla)\mathbf{v} = -\frac{{c_\mathrm{s}}^2}{\Sigma}\nabla\Sigma - \nabla\Psi|_{z=0}, \tag{A.2}$$

and

$$\nabla^2 \Psi = 4\pi G \Sigma \delta(z), \tag{A.3}$$

where t is the time, Σ is the surface density of the disk, $\mathbf{v}$ is the velocity vector of the fluid, c_s is the sound velocity, Ψ is the gravitational potential, G is the gravitational constant, and $\delta(z)$ is the Dirac delta function. We adopt the cylindrical coordinate system (r, ϕ, z) at rest. From equations (A.1) and (A.2), we have

$$\frac{\partial \Sigma}{\partial t} + \frac{\partial}{\partial r}(\Sigma v_r) + \frac{\Sigma v_r}{r} = 0, \tag{A.4}$$

$$\frac{\partial v_r}{\partial t} + v_r \frac{\partial v_r}{\partial r} - \frac{{v_\phi}^2}{r} = -\frac{{c_\mathrm{s}}^2}{\Sigma}\frac{\partial \Sigma}{\partial r} - \left.\frac{\partial \Psi}{\partial r}\right|_{z=0}, \tag{A.5}$$

and

$$\frac{\partial v_\phi}{\partial t} + v_r \frac{\partial v_\phi}{\partial r} - \frac{v_r v_\phi}{r} = 0, \tag{A.6}$$

where (v_r, v_ϕ) are the (r, ϕ) components of the velocity.

We assume that the unperturbed surface density is steady and uniform, and that the r component of the unperturbed velocity is zero. We assume that the angular velocity of the disk, Ω ($\equiv v_{\phi 0}/r$, where subscript 0 refers the unperturbed quantities), is proportional to $r^{-3/2}$. For the unperturbed state, from equation (A.5), we obtain the balance of the centrifugal force and the gravity,

$$\frac{{v_{\phi 0}}^2}{r} = \left.\frac{\partial \Psi_0}{\partial r}\right|_{z=0}. \tag{A.7}$$

From equation (A.3), we have

$$\nabla^2 \Psi_0 = 4\pi G \Sigma_0 \delta(z). \tag{A.8}$$

To obtain the linear perturbation equations, we give the quantities as $f = f_0 + f_1$, where subscript 1 refers the perturbed quantities, and neglect the second-order terms and higher-order terms of the perturbed quantities. For the perturbed state, from equations (A.3)-(A.8), we have

$$\frac{\partial \Sigma_1}{\partial t} + \Sigma_0 \frac{\partial v_{r1}}{\partial r} + \frac{\Sigma_0 v_{r1}}{r} = 0, \tag{A.9}$$

$$\frac{\partial v_{r1}}{\partial t} - 2 v_{\phi 1} \Omega = -\frac{{c_{\rm s}}^2}{\Sigma_0} \frac{\partial \Sigma_1}{\partial r} - \left.\frac{\partial \Psi_1}{\partial r}\right|_{z=0}, \tag{A.10}$$

$$\frac{\partial v_{\phi 1}}{\partial t} - \frac{v_{r1}\Omega}{2} = 0, \tag{A.11}$$

and

$$\nabla^2 \Psi_1 = 4\pi G \Sigma_1 \delta(z). \tag{A.12}$$

For simplicity, for perturbed quantities, Σ_1 and $\mathbf{v}_1$ are assumed to have the form as $f_1 = \hat{f} \exp[i(kr - \omega t)]$, where k is the wave number in the direction of r, and ω is the angular frequency. At $z \neq 0$, equation (A.12) is given as $\nabla^2 \Psi_1 = 0$. To satisfy this equation, we assume Ψ_1 as

$$\Psi_1 = \hat{\Psi} \exp[i(kr - \omega t)] \exp(-|kz|). \tag{A.13}$$

Integrating equation (A.12) with respect to z from $z = -\epsilon$ to $z = +\epsilon$ and taking the limit of $\epsilon \to +0$, we obtain

$$\begin{aligned}\lim_{\epsilon\to+0}\int_{-\epsilon}^{+\epsilon}\nabla^2\Psi_1 dz &= \lim_{\epsilon\to+0}\int_{-\epsilon}^{+\epsilon}\frac{\partial^2\Psi_1}{\partial z^2}dz \\ &= \lim_{\epsilon\to+0}\left(\left.\frac{\partial\Psi_1}{\partial z}\right|_{z=+\epsilon} - \left.\frac{\partial\Psi_1}{\partial z}\right|_{z=-\epsilon}\right) \\ &= -2k\hat{\Psi}\exp[i(kr-\omega t)] \\ &= 4\pi G\hat{\Sigma}\exp[i(kr-\omega t)]. \end{aligned} \tag{A.14}$$

From equation (A.14), we obtain

$$\hat{\Psi} = -\frac{2\pi G}{k}\hat{\Sigma}. \tag{A.15}$$

We consider the local stability of the disk, then we assume that $kr \gg 1$. From equations (A.9)-(A.11), (A.13) and (A.15), we have

$$-i\omega\hat{\Sigma} + ik\Omega_0\hat{v}_r = 0, \tag{A.16}$$

$$-i\omega\hat{v}_r - 2\hat{v}_\phi\Omega = -ik{c_{\rm s}}^2\frac{\hat{\Sigma}}{\Sigma_0} + 2\pi iG\hat{\Sigma}, \tag{A.17}$$

and

$$-i\omega\hat{v}_\phi + \frac{1}{2}\hat{v}_r\Omega = 0. \tag{A.18}$$

From equations (A.16)-(A.18), we obtain the dispersion relation as

$$\omega^2 = {c_{\rm s}}^2k^2 - 2\pi G\Sigma_0 k + \Omega^2 = {c_{\rm s}}^2\left(k - \frac{\pi G\Sigma_0}{{c_{\rm s}}^2}\right)^2 + \Omega^2 - \left(\frac{\pi G\Sigma_0}{c_{\rm s}}\right)^2. \tag{A.19}$$

From equation (A.19), the condition when the gravitational instability of the disk occurs is given by

$$\frac{c_{\rm s}\Omega}{\pi G\Sigma_0} \equiv Q < 1. \tag{A.20}$$

From equation (A.20), it is indicated that the disk fragmentation tends to occur in the case with the small central star and/or with the cold protoplanetary disk.

Appendix B

Radial and Rotational Velocities of Gas and Dust Components

We present the derivation of the radial and rotational velocities of the gas and the dust components. This chapter is mainly based on Nakagawa et al. (1986). We consider that the disk is axisymmetric with respect to the rotational axis of the disk. We adopt the cylindrical coordinate system (r, ϕ, z) at rest. In this coordinate system, the temporal differentiation of the velocity vector, $d\mathbf{v}/dt$, is given by

$$\frac{d\mathbf{v}}{dt} = \frac{d}{dt}(v_r \mathbf{e}_r + v_\phi \mathbf{e}_\phi + v_z \mathbf{e}_z) = \left(\frac{dv_r}{dt} - \frac{{v_\phi}^2}{r} \right) \mathbf{e}_r + \left(\frac{dv_\phi}{dt} + \frac{v_r v_\phi}{r} \right) \mathbf{e}_\phi + \frac{dv_z}{dt} \mathbf{e}_z, \tag{B.1}$$

where (v_r, v_ϕ, v_z) are the (r, ϕ, z) components of the velocity, and $\mathbf{e}_r$, $\mathbf{e}_\phi$ and $\mathbf{e}_z$ are basis vectors. In equation (B.1), we use $v_\phi \equiv r(d\phi/dt)$.

For simplicity, we assume that the protoplanetary disk is geometrically thin, then we assume $(r^2 + z^2)^{1/2} \simeq r$ and $\partial \Omega_{\rm K}/\partial z = 0$. We set the velocity $(v_r, v_\phi, v_z) \equiv (0, v_{\rm K}, 0) + (V_r, V_\phi, V_z)$, where $v_{\rm K} = r\Omega_{\rm K}$ is the Keplerian velocity. Then, we have

$$\begin{aligned} \frac{dv_r}{dt} - \frac{{v_\phi}^2}{r} &= \frac{\partial v_r}{\partial t} + v_r \frac{\partial v_r}{\partial r} + \frac{v_\phi}{r} \frac{\partial v_r}{\partial \phi} + v_z \frac{\partial v_r}{\partial z} - \frac{{v_\phi}^2}{r} \\ &= \frac{\partial V_r}{\partial t} + V_r \frac{\partial V_r}{\partial r} + V_z \frac{\partial V_r}{\partial z} - \frac{{V_\phi}^2}{r} - 2\Omega_{\rm K} V_\phi - {\Omega_{\rm K}}^2 r, \end{aligned} \tag{B.2}$$

and

$$\frac{dv_\phi}{dt} + \frac{v_r v_\phi}{r} = \frac{\partial V_\phi}{\partial t} + v_r\frac{\partial V_\phi}{\partial r} + \frac{v_\phi}{r}\frac{\partial V_\phi}{\partial \phi} + v_z\frac{\partial V_\phi}{\partial z} + \frac{dv_{\rm K}}{dt} + \frac{V_r(V_\phi + v_{\rm K})}{r}$$
$$= \frac{\partial V_\phi}{\partial t} + V_r\frac{\partial V_\phi}{\partial r} + V_z\frac{\partial V_\phi}{\partial z} + \frac{1}{2}\Omega_{\rm K}V_r + \frac{V_r V_\phi}{r}. \tag{B.3}$$

We assume that $|V_r|, |V_\phi|$ and $|V_z| \ll v_{\rm K}$, and we neglect the second-order terms of V_r, V_ϕ and V_z, then we have

$$\frac{d\mathbf{v}}{dt} = \left(\frac{\partial V_r}{\partial t} - 2\Omega_{\rm K}V_\phi - {\Omega_{\rm K}}^2 r\right)\mathbf{e}_r + \left(\frac{\partial V_\phi}{\partial t} + \frac{1}{2}\Omega_{\rm K}V_r\right)\mathbf{e}_\phi + \frac{dv_z}{dt}\mathbf{e}_z. \tag{B.4}$$

The equations of motion for gas and dust are given by

$$\frac{d\mathbf{v}_{\rm g}}{dt} = -\frac{\rho_{\rm d}}{\rho_{\rm g}}\frac{\mathbf{v}_{\rm g} - \mathbf{v}_{\rm d}}{t_{\rm stop}} - {\Omega_{\rm K}}^2\mathbf{R} - \frac{1}{\rho_{\rm g}}\nabla P_{\rm g}, \tag{B.5}$$

and

$$\frac{d\mathbf{v}_{\rm d}}{dt} = -\frac{\mathbf{v}_{\rm d} - \mathbf{v}_{\rm g}}{t_{\rm stop}} - {\Omega_{\rm K}}^2\mathbf{R}, \tag{B.6}$$

where t is the time, $\mathbf{v}_{\rm g}$ and $\mathbf{v}_{\rm d}$ are the velocity vectors of the gas and the dust components, $\rho_{\rm g}$ and $\rho_{\rm d}$ is the densities of the gas and the dust components, $t_{\rm stop}$ is the stopping time, $\Omega_{\rm K}$ is the Keplerian angular velocity, $\mathbf{R}$ is the heliocentric position vector and $P_{\rm g} = {c_{\rm s}}^2\rho_{\rm g}$ is the gas pressure, where $c_{\rm s}$ is the sound velocity. From equations (B.4)-(B.6), we have

$$\frac{\partial V_{{\rm g}r}}{\partial t} = -\frac{\rho_{\rm d}}{\rho_{\rm g}}\frac{V_{{\rm g}r} - V_{{\rm d}r}}{t_{\rm stop}} + 2\Omega_{\rm K}V_{{\rm g}\phi} - \frac{1}{\rho_{\rm g}}\frac{\partial P_{\rm g}}{\partial r}, \tag{B.7}$$

$$\frac{\partial V_{{\rm g}\phi}}{\partial t} = -\frac{\rho_{\rm d}}{\rho_{\rm g}}\frac{V_{{\rm g}\phi} - V_{{\rm d}\phi}}{t_{\rm stop}} - \frac{1}{2}\Omega_{\rm K}V_{{\rm g}r}, \tag{B.8}$$

$$\frac{\partial V_{{\rm d}r}}{\partial t} = -\frac{V_{{\rm d}r} - V_{{\rm g}r}}{t_{\rm stop}} + 2\Omega_{\rm K}V_{{\rm d}\phi}, \tag{B.9}$$

and

$$\frac{\partial V_{{\rm d}\phi}}{\partial t} = -\frac{V_{{\rm d}\phi} - V_{{\rm g}\phi}}{t_{\rm stop}} - \frac{1}{2}\Omega_{\rm K}V_{{\rm d}r}. \tag{B.10}$$

Setting $\partial/\partial t = 0$ in equations (B.7)-(B.10) for simplicity, we obtain the (terminal) velocities in radial and azimuthal direction of the gas and the dust components as

$$v_{{\rm g}r} = \frac{\rho_{\rm d}}{\rho_{\rm g} + \rho_{\rm d}}\frac{2D\Omega_{\rm K}}{D^2 + {\Omega_{\rm K}}^2}\eta v_{\rm K}, \tag{B.11}$$

$$v_{\mathrm{g}\phi} = (1-\eta)v_{\mathrm{K}} + \frac{\rho_{\mathrm{d}}}{\rho_{\mathrm{g}}+\rho_{\mathrm{d}}}\frac{D^2}{D^2+{\Omega_{\mathrm{K}}}^2}\eta v_{\mathrm{K}}, \tag{B.12}$$

$$v_{\mathrm{d}r} = -\frac{\rho_{\mathrm{g}}}{\rho_{\mathrm{g}}+\rho_{\mathrm{d}}}\frac{2D\Omega_{\mathrm{K}}}{D^2+{\Omega_{\mathrm{K}}}^2}\eta v_{\mathrm{K}}, \tag{B.13}$$

and

$$v_{\mathrm{d}\phi} = v_{\mathrm{K}} - \frac{\rho_{\mathrm{g}}}{\rho_{\mathrm{g}}+\rho_{\mathrm{d}}}\frac{D^2}{D^2+{\Omega_{\mathrm{K}}}^2}\eta v_{\mathrm{K}}, \tag{B.14}$$

where

$$D \equiv \left(1+\frac{\rho_{\mathrm{d}}}{\rho_{\mathrm{g}}}\right)\frac{1}{t_{\mathrm{stop}}}. \tag{B.15}$$

Appendix C

Linear Stability Analysis of Dust Layer for GI

We present the linear stability analysis of the dust layer. This chapter is mainly based on Sekiya (1983). We consider that the disk is axisymmetric with respect to the rotational axis of the disk. We adopt the cylindrical coordinate system (r, ϕ, z) at rest. For simplicity, we assume that the protoplanetary disk is geometrically thin, then we assume $(r^2 + z^2)^{1/2} \simeq r$ and $\partial\Omega_{\rm K}/\partial z = 0$. We assume the polytropic equation of state for the gad fluid, given by

$$P_{\rm g} = \chi_{\rm g}{\rho_{\rm g}}^{\gamma}. \tag{C.1}$$

Before GI, dust aggregates are so small that the stopping times of dust aggregates are much smaller than the Keplerian period (Nakagawa et al. 1981, 1986). Then, dust aggregates are small enough to couple strongly to gas, and the mixture of gas and dust can be treated as one component fluid. Then, governing equations are given as

$$\frac{\partial U}{\partial t} + U\frac{\partial U}{\partial r} + W\frac{\partial U}{\partial z} - \frac{V^2}{r} = -{\Omega_{\rm K}}^2 r - \frac{\partial \psi}{\partial r} - \frac{1}{\rho}\frac{\partial P}{\partial r}, \tag{C.2}$$

$$\frac{\partial V}{\partial t} + U\frac{\partial V}{\partial r} + W\frac{\partial V}{\partial z} + \frac{UV}{r} = 0, \tag{C.3}$$

$$\frac{\partial W}{\partial t} + U\frac{\partial W}{\partial r} + W\frac{\partial W}{\partial z} = -{\Omega_{\rm K}}^2 z - \frac{\partial \psi}{\partial z} - \frac{1}{\rho}\frac{\partial P}{\partial z}, \tag{C.4}$$

$$\frac{\partial \rho}{\partial t} + \frac{\partial}{\partial r}(\rho U) + \frac{\partial}{\partial z}(\rho W) + \frac{\rho U}{r} = 0, \tag{C.5}$$

$$P = \chi \rho^\gamma, \tag{C.6}$$

and

$$\left(\frac{1}{r}\frac{\partial}{\partial r} r \frac{\partial}{\partial r} + \frac{\partial^2}{\partial z^2}\right)\psi = 4\pi G\rho, \tag{C.7}$$

where (U, V, W) are the (r, ϕ, z) components of the velocity, ψ is the gravitational potential, $P = P_{\rm g}$ is the pressure, $\rho = \rho_{\rm g} + \rho_{\rm d}$ is the density and $\chi = \chi_{\rm g}(1 + \rho_{\rm d}/\rho_{\rm g})^{-1}$.

Hereafter, subscript 0 refers the unperturbed quantities, and subscript 1 refers the perturbed quantities. We assume that the unperturbed quantities are symmetric with respect to the midplane of the disk. We assume $\partial\rho_0/\partial r = 0$, $\partial P_0/\partial r = 0$ and $\partial\psi_0/\partial r = 0$. We integrate equation (C.7) with respect to z from 0 to z, then we have

$$\frac{d\psi_0}{dz} = 2\pi G\sigma_0(z), \tag{C.8}$$

where

$$\sigma_0(z) \equiv 2\int_0^z \rho_0 dz. \tag{C.9}$$

At $z = h$, where h is the scale height of the dust layer, $\sigma_0(h)$ is the surface density of the dust layer. We assume that the angular velocity of the mixed fluid of gas and dust is the Keplerian angular velocity, and that the unperturbed velocity (U_0, V_0, W_0) is given by $(0, \Omega_{\rm K} r, 0)$. Then, $\partial V_0/\partial r = -\Omega_{\rm K}/2$. From equations (C.2) and (C.4)-(C.6), we have

$$-\frac{{V_0}^2}{r} = -{\Omega_{\rm K}}^2 r, \tag{C.10}$$

$$0 = -{\Omega_{\rm K}}^2 z - \frac{\partial \psi_0}{\partial z} - \frac{1}{\rho_0}\frac{\partial P_0}{\partial z}, \tag{C.11}$$

and

$$P_0 = \chi {\rho_0}^\gamma. \tag{C.12}$$

To obtain the linear perturbation equations, we give the quantities as $F = F_0 + F_1$ and neglect the second-order terms and higher-order terms of the perturbed quantities. For the perturbed state, from equations (C.2)-(C.12), we have

$$\frac{\partial U_1}{\partial t} - 2\Omega_{\rm K} V_1 = -\frac{\partial}{\partial r}\left(\psi_1 - \frac{P_1}{\rho_0}\right), \tag{C.13}$$

$$\frac{\partial V_1}{\partial t} + \frac{1}{2}\Omega_{\rm K} U_1 = 0, \tag{C.14}$$

$$\frac{\partial W_1}{\partial t} = -\frac{\partial}{\partial z}\left(\psi_1 - \frac{P_1}{\rho_0}\right), \tag{C.15}$$

$$\frac{\partial \rho_1}{\partial t} + \rho_0 \frac{\partial U_1}{\partial r} + \frac{\partial}{\partial z}(\rho_0 W_1) + \frac{\rho_0 U_1}{r} = 0, \tag{C.16}$$

$$P_1 = {c_0}^2 \rho_1, \tag{C.17}$$

and

$$\left(\frac{1}{r}\frac{\partial}{\partial r} r \frac{\partial}{\partial r} + \frac{\partial^2}{\partial z^2}\right)\psi_1 = 4\pi G \rho_1, \tag{C.18}$$

where $c_0 \equiv (\chi\gamma{\rho_0}^{\gamma-1})^{1/2}$ is the sound velocity. We assume $\partial c_0/\partial r = 0$. For simplicity, perturbed quantities are assumed to have the form as $F_1 = \tilde{F}(z) J_1(kr)\exp(-i\omega t)$, where k is the wave number in the direction of r, ω is the angular frequency and J_1 is the first-order Bessel function of the first kind. From equations (C.13)-(C.18), we obtain

$$-i\omega\tilde{U} - 2\Omega_{\rm K}\tilde{V} = \tilde{f}, \tag{C.19}$$

$$-i\omega\tilde{V} + \frac{1}{2}\Omega_{\rm K}\tilde{U} = 0, \tag{C.20}$$

$$-i\omega\tilde{W}_r = \frac{d\tilde{f}}{dz}, \tag{C.21}$$

$$-i\omega\tilde{\rho}_r - k^2\rho_0\tilde{U} + \frac{d}{dz}\left(\rho_0\tilde{W}_r\right) = 0, \tag{C.22}$$

$$\tilde{g} - \tilde{f} = \frac{{c_0}^2}{\rho_0}\tilde{\rho}_r, \tag{C.23}$$

and

$$\left(-k^2 + \frac{d^2}{dz^2}\right)\tilde{g} = -4\pi G\tilde{\rho}_r, \tag{C.24}$$

where

$$f_1 \equiv -\frac{\partial}{\partial r}\left(\psi_1 - \frac{P_1}{\rho_0}\right), \tag{C.25}$$

$$g_1 \equiv -\frac{\partial \psi_1}{\partial r}, \tag{C.26}$$

$$W_r \equiv \frac{\partial W_1}{\partial r}, \tag{C.27}$$

and

$$\rho_r \equiv \frac{\partial \rho_1}{\partial r}. \tag{C.28}$$

We assume that the mixed fluid of gas and dust is incompressible, i.e., that $c_0 = \infty$, $\tilde{\rho}_r = 0$ and $d\rho_0/dz = 0$. Then, from equation (C.9), the surface density of the dust layer is given by

$$\sigma_0(h) = 2\rho_0 h. \tag{C.29}$$

From equations (C.22) and (C.24), we obtain

$$-k^2\tilde{U} + \frac{d\tilde{W}_r}{dz} = 0, \tag{C.30}$$

and

$$\left(-k^2 + \frac{d^2}{dz^2}\right)\tilde{g} = 0. \tag{C.31}$$

To obtain a dispersion relation, we consider the boundary conditions between the dust layer and the gas layers. In the perturbed state, the boundary surface becomes slightly deformed. We define the displacement of the boundary surface perpendicular to the midplane by h_1. For the displacement of the boundary, h_1, we have

$$\frac{\partial h_1}{\partial t} = W_1(z = h_0 + h_1) = W_1(z = h_0) + \left.\frac{\partial W_1}{\partial z}\right|_{z=h_0} h_1 = W_1(z = h_0), \tag{C.32}$$

then

$$\frac{\partial^2 h_1}{\partial t^2} = \left.\frac{\partial W_1}{\partial t}\right|_{z=h_0}. \tag{C.33}$$

We put $\partial h_1/\partial r \equiv h_r = \tilde{h}_r J_1(kr)\exp(-i\omega t)$. From equations (C.21) and (C.33), we have

$$-\omega^2 \tilde{h}_r = \left.\frac{d\tilde{f}}{dz}\right|_{z=h_0}. \tag{C.34}$$

At the boundary surface, the pressure is continuous between the dust layer and the gas layers. The boundary condition is given by

$$P(h_0 + h_1) = P_{\rm ge}, \tag{C.35}$$

where $P_{\rm ge}$ is the gas pressure at the boundary. We assume that $P_{\rm ge}$ is constant even if there is the displacement of the boundary surface. Then we have

$$P(h_0) = P_0(h_0) + P_1(h_0) = P_{\rm ge} + P_1(h_0) = P(h_0 + h_1) + P_1(h_0). \tag{C.36}$$

The equation of motion of a fluid element in the range $h_0 < z < h_0 + h_1$ is given by

$$\rho_0 \frac{dW}{dt} = \rho_0 \left(-\frac{\partial \psi}{\partial z} - {\Omega_{\rm K}}^2 z \right) - \frac{\partial P}{\partial z}. \tag{C.37}$$

We integrate equation (C.37) with respect to z from $z = h_0$ to $z = h_0 + h_1$ and neglect the second-order terms of the perturbed quantities. For the left-hand side of equation (C.37), we obtain

$$\int_{h_0}^{h_0+h_1} \rho_0 \frac{dW}{dt} dz = \rho_0 \int_{h_0}^{h_0+h_1} \frac{dW_1}{dt} dz = \rho_0 \left. \frac{dW_1}{dt} \right|_{z=h_0} h_1 = 0. \tag{C.38}$$

For the right-hand side of equation (C.37), from equation (C.36), we have

$$\begin{aligned} &\int_{h_0}^{h_0+h_1} \left[\rho_0 \left(-\frac{\partial \psi}{\partial z} - {\Omega_{\rm K}}^2 z \right) - \frac{\partial P}{\partial z} \right] dz \\ &= -\rho_0 \left. \left(\frac{\partial \psi}{\partial z} + {\Omega_{\rm K}}^2 z \right) \right|_{z=h_0} h_1 - [P(h_0 + h_1) - P(h_0)] \\ &= -\rho_0 \left(\left. \frac{\partial \psi_0}{\partial z} \right|_{z=h_0} + {\Omega_{\rm K}}^2 h_0 \right) h_1 + P_1(h_0). \end{aligned} \tag{C.39}$$

From equations (C.37)-(C.39), $P_1(h_0)$ is given as

$$P_1(h_0) = \rho_0 \left(\left. \frac{\partial \psi_0}{\partial z} \right|_{z=h_0} + {\Omega_{\rm K}}^2 h_0 \right) h_1. \tag{C.40}$$

From equations (C.8) and (C.29), we have

$$\left. \frac{\partial \psi_0}{\partial z} \right|_{z=h_0} = 4\pi G \rho_0 h_0. \tag{C.41}$$

From equations (C.40) and (C.41), $P_1(h_0)$ is given by

$$P_1(h_0) = \rho_0 h_1 (4\pi G\rho_0 + {\Omega_{\rm K}}^2) h_0. \tag{C.42}$$

From equations (C.25), (C.26) and (C.42), we obtain

$$\tilde{g}(h_0) - \tilde{f}(h_0) = \tilde{h}_r (4\pi G\rho_0 + {\Omega_{\rm K}}^2) h_0. \tag{C.43}$$

At the boundary surface, the gravitational potential is also continuous between the dust layer and the gas layers (Goldreich & Lynden-Bell 1965). The boundary condition is given by

$$\psi_1(z = h_0+) = \psi_1(z = h_0-). \tag{C.44}$$

From equation (C.7), we have

$$\left.\frac{\partial \psi_1}{\partial z}\right|_{z=h_0+} - \left.\frac{\partial \psi_1}{\partial z}\right|_{z=h_0-} = 4\pi G\rho_0 h_1. \tag{C.45}$$

At $|z| \to \pm\infty$, ψ_1 should become zero. To satisfy this condition, we assume that $\tilde{\psi}$ as

$$\tilde{\psi}(z) \propto \exp(-k|z|). \tag{C.46}$$

From equations (C.44)-(C.46), we have

$$\left.\frac{d\tilde{\psi}}{dz}\right|_{z=h_0-} + 4\pi G\rho_0 \tilde{h} + k\tilde{\psi}(z = h_0-) = 0. \tag{C.47}$$

From equations (C.26) and (C.47), the condition at $z = h_0$ in the dust layer is given as

$$\left.\frac{d\tilde{g}}{dz}\right|_{z=h_0} - 4\pi G\rho_0 \tilde{h}_r + k\tilde{g}(z = h_0) = 0. \tag{C.48}$$

From equations (C.19)-(C.21), (C.30), (C.31), (C.34), (C.43) and (C.48), we obtain the dispersion relation as

$$\frac{\omega^2}{{\Omega_{\rm K}}^2} = \left[1 + \left(1 - \frac{1 + e^{-2K}}{2K}\right) \frac{4\pi G\rho_0}{{\Omega_{\rm K}}^2}\right] nK \tanh(nK), \tag{C.49}$$

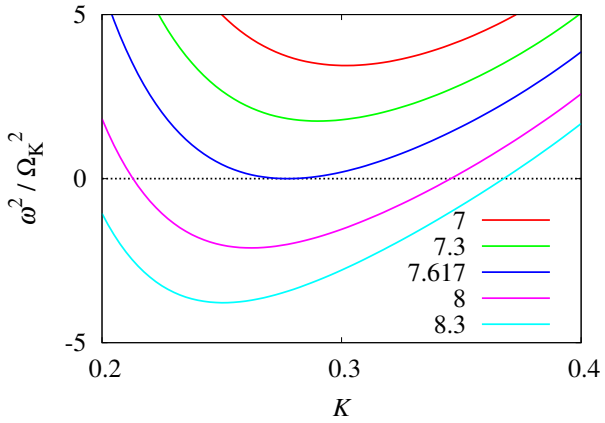

Figure C.1: Angular frequencies as functions of the wave number given by equation (C.50). Solid lines shows $\omega^2/{\Omega_\mathrm{K}}^2$ for cases with $4\pi G\rho_0/{\Omega_\mathrm{K}}^2 = 7$ (red), 7.3 (green), 7.617 (blue), 8 (magenta) and 8.3 (cyan), respectively.

where $n^2 \equiv (1 - {\Omega_\mathrm{K}}^2/\omega^2)^{-1}$ and $K \equiv kh_0$. To obtain the condition with $\omega^2 < 0$, we consider the case with $|\omega^2/{\Omega_\mathrm{K}}^2| \ll 1$. Using $\tanh(0 + x) = x - x^3/3$, from equation (C.49), we have

$$\frac{\omega^2}{{\Omega_\mathrm{K}}^2} = -\left\{1 + \left[1 + \left(1 - \frac{1 + e^{-2K}}{2K}\right)\frac{4\pi G\rho_0}{{\Omega_\mathrm{K}}^2}\right]^{-1} K^{-2}\right\} 3K^{-2}. \tag{C.50}$$

Figure C.1 shows the angular frequencies as functions of the wave number given by equation (C.50). In figure C.1, solid lines shows $\omega^2/{\Omega_\mathrm{K}}^2$ for cases with $4\pi G\rho_0/{\Omega_\mathrm{K}}^2 = 7$ (red), 7.3 (green), 7.617 (blue), 8 (magenta) and 8.3 (cyan), respectively. From figure C.1, in the case with $4\pi G\rho_0/{\Omega_\mathrm{K}}^2 = 7.617$, i.e.,

$$\rho_0 = \frac{0.61 M_*}{r^3} \equiv \rho_\mathrm{c}, \tag{C.51}$$

the angular frequency becomes zero at $K = 0.2775$, and in the case with $\rho_0 > \rho_\mathrm{c}$, the unstable mode exists. Then, the dust layer fragments into pieces if the unstable mode exists in the system (Goldreich & Ward 1973). In the MMSN model, the mode with $\rho_0 = \rho_\mathrm{c}$ and $K = 0.2775$ has the wavelength given by 2.2×10^8 cm at $r = 1$ AU. Then, the mass of the fragment is about 10^{18} g and the size of the fragment is several kilometers if the internal density of the piece is about 1 g cm^{-3}. This is shown that the mass of this fragment corresponds to the planetesimal.

Appendix D

Methods of Numerical Calculations

We present methods of numerical calculations performed in subsection 1.4.1 and in chapter 3.

D.1 Coordinates of Space and Mass

The range of calculations ($0 \leq z \lesssim 3H_{\rm g}$) along the z coordinates are logarithmically divided into 106 spaced grids as z_j. The grids are set to be rest and are given as

$$z_j = \begin{cases} (2j+1)/(10{\delta_z}^{95})H_{\rm g} & (0 \leq j \leq 4) \\ (\delta_z + 1)/(2{\delta_z}^{100-j})H_{\rm g} & (5 \leq j \leq 105) \end{cases}, \tag{D.1}$$

where $\delta_z = 2^{1/4}$. The thickness of the grid is given as

$$\Delta z_j = \begin{cases} 1/(5{\delta_z}^{95})H_{\rm g} & (0 \leq j \leq 4) \\ (\delta_z - 1)/({\delta_z}^{100-j})H_{\rm g} & (5 \leq j \leq 105) \end{cases}. \tag{D.2}$$

The thickness of the nearest grid to the midplane, Δz_0, is $1.4 \times 10^{-8} H_{\rm g}$. Using this spatial resolution, the dust scale height when GI occurs is sufficiently resolved. From equations (D.1) and (D.2), $z_{105} + \Delta z_{105}/2 = 2.8 H_{\rm g}$.

Mass coordinates, m_i, are logarithmically divided into 400 mass bins. The mass coordinate

varies with time, and the initial mass coordinate is given as

$$m_i = \begin{cases} (i+1)m_0 & (0 \leq i \leq 9) \\ \delta_m m_{i-1} & (10 \leq i \leq 399) \end{cases}, \tag{D.3}$$

where $\delta_m = 1.1$. At $t = 0$, $m_{399} = 1.4 \times 10^{17} m_0$. If $s_0 \equiv (3m_0/4\pi\rho_{\rm s})^{1/3} = 1$ μm, then $s_{399} \equiv (3m_{399}/4\pi\rho_{\rm s})^{1/3} = 52$ cm. The width of the grid is given as

$$\Delta m_i = \frac{m_{i+1} - m_{i-1}}{2}. \tag{D.4}$$

We always assume $m_{-1} = 0$ and $m_{400} = \delta_m m_{399}$.

D.2 Numerical Method for Dust Sedimentation

In our numerical calculations, the TVD scheme (Roe 1986) is applied to calculate the sedimentation of dust aggregates.

D.2.1 Detail of Scheme

The equation of continuity for a physical quantity, f, with a velocity, v, in one direction, x, is given by

$$\frac{\partial}{\partial t} f(t,x) + \frac{\partial}{\partial x}[f(t,x)v(x)] = 0. \tag{D.5}$$

Equation (D.5) corresponds to equation (1.37) without dust growth. Using the explicit method, we obtain

$$f_j^{n+1} = f_j^n - \left(\tilde{f}_{j+1/2}^n v_{j+1/2} - \tilde{f}_{j-1/2}^n v_{j-1/2} \right) \frac{\Delta t}{\Delta x_j}, \tag{D.6}$$

where $f_j^n \equiv f(t_n, x_j)$, $f_j^{n+1} \equiv f(t_n + \Delta t, x_j)$, $v_{j+1/2} \equiv v(x_j + \Delta x_j/2)$, $v_{j-1/2} \equiv v(x_j - \Delta x_j/2)$ and Δt is the time interval of the numerical calculation. In the first-order upwind difference scheme, $\tilde{f}_{j+1/2}^n$ is given by

$$\tilde{f}_{j+1/2}^n = \begin{cases} f_j^n & (v_{j+1/2} > 0) \\ f_{j+1}^n & (v_{j+1/2} < 0) \end{cases}. \tag{D.7}$$

On the other hand, in the TVD scheme (Roe 1986), $\tilde{f}^n_{j+1/2}$ is given by

$$\tilde{f}^n_{j+1/2} = f^n_j + \mathrm{minmod}\left(\frac{f^n_{j+1}-f^n_j}{x_{j+1}-x_j}, \frac{f^n_j - f^n_{j-1}}{x_j - x_{j-1}}\right)\frac{\Delta x_j}{2} \quad \text{(for the case with } v_{j+1/2} > 0\text{)}, \quad \text{(D.8)}$$

or

$$\tilde{f}^n_{j+1/2} = f^n_{j+1} - \mathrm{minmod}\left(\frac{f^n_{j+2}-f^n_{j+1}}{x_{j+2}-x_{j+1}}, \frac{f^n_{j+1} - f^n_j}{x_{j+1} - x_j}\right)\frac{\Delta x_{j+1}}{2} \quad \text{(for the case with } v_{j+1/2} < 0\text{)}, \quad \text{(D.9)}$$

where

$$\mathrm{minmod}(a,b) = \begin{cases} a & (ab \geq 0 \text{ and } |a| \leq |b|) \\ b & (ab \geq 0 \text{ and } |a| > |b|) \\ 0 & (ab < 0) \end{cases} . \quad \text{(D.10)}$$

D.2.2 Test Calculation

As a test calculation, we adopt the initial condition that is given by

$$f(t=0,x) = \begin{cases} \exp\{-[(x-20)/10]^2\} & (0 \leq x \leq 40) \\ 0 & (40 < x < 60) \\ 1 & (60 \leq x \leq 100) \\ 0 & (100 < x < 120) \end{cases} . \quad \text{(D.11)}$$

We adopt the periodic boundary condition that is given by

$$f(t,x) = f(t,x+120). \quad \text{(D.12)}$$

We set $v = 1$, $x_j = j$, $\Delta x = 1$ and $\Delta t = 0.2$. Figure D.1 shows the results with our numerical method for the advection (corresponding to the sedimentation of dust aggregates) at $t = 120$. In figure D.1, it is seen that result of the calculation using the TVD scheme is better than that using the first-order upwind difference scheme.

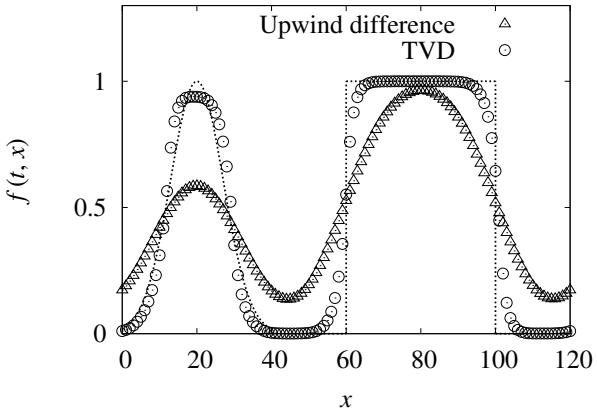

Figure D.1: Results of the numerical advection test (corresponding to the sedimentation of dust aggregates in this thesis) at $t = 120$. Numerical results calculated using the first-order upwind difference scheme (triangles) and the TVD scheme (circles) are compared with the analytic solution (dotted line).

D.3 Numerical Method for Dust Growth

In our numerical calculations, the method with moving meshes (Wetherill & Stewart 1989) is applied for dust growth.

D.3.1 Detail of Scheme

The coagulation equation for a mass function, f, with a mass of bodies, m, is given by

$$\frac{\partial}{\partial t}f(t,m) = -f(t,m)\int_0^\infty K(m,m')f(t,m')dm' + \frac{1}{2}\int_0^m K(m-m',m')f(t,m-m')f(t,m')dm', \tag{D.13}$$

where $K(m,m')$ is the coalescence rate for bodies with m and m'. Equation (D.13) corresponds to equation (1.37) without dust sedimentation. Hereafter, we consider the case when f is the mass function described in equation (1.37). Using the explicit method, the term in the left-

hand side of equation (D.13) is replaced by

$$\frac{f_i^{n+1} - f_i^n}{\Delta t}, \tag{D.14}$$

where $f_i^n \equiv f(t_n, m_i)$ and $f_i^{n+1} \equiv f(t_n + \Delta t, m_i)$. The second term in the right-hand side of equation (D.13) is replaced by

$$\sum_{l \geq k} \frac{K_{lk}}{1 + \delta_{kl}} f_l^n f_k^n \Delta m_k \equiv \sum_{l \geq k} \nu_{kl}, \tag{D.15}$$

where $K_{lk} \equiv K(m_l, m_k)$, δ_{kl} is the Kronecker delta function, and k and l are given as

$$\frac{1}{2}(m_i + m_{i-1}) \leq m_k + m_l < \frac{1}{2}(m_{i+1} + m_i), \tag{D.16}$$

Using equations (D.14) and (D.15), we approximate the coagulation equation by

$$f_i^{n+1} = f_i^n + \left(-\sum_{k=0}^{\infty} \nu_{ki} + \sum_{l \geq k} \nu_{kl} \right) \Delta t. \tag{D.17}$$

In order to calculate the time evolution of the mass function, we numerically solve this equation.

Next, we consider the total mass of bodies contained within a bin of ith mass, $M_i^n \Delta m_i$. At $t = 0$, $M_i^n = m_i f_i^n$. In the case with $(m_i + m_{i-1})/2 \leq m_k + m_l < (m_{i+1} + m_i)/2$, f_k decreases by $\nu_{kl}\Delta t$, f_l also decreases by $\nu_{kl}\Delta t$, and f_i increases by $\nu_{kl}\Delta t$. Then, M_k decreases by $m_k \nu_{kl}\Delta t$, M_l decreases by $m_l \nu_{kl}\Delta t$, and M_i increases not by $m_i \nu_{kl}\Delta t$ but by $(m_k + m_l)\nu_{kl}\Delta t$. In such a case, we have $f_i^{n+1} = f_i^n + \nu_{kl}\Delta t$ and $M_i^{n+1} = M_i^n + (m_k + m_l)\nu_{kl}\Delta t$. At the next time step, $t = t_n + \Delta t$, we redefine a new mass coordinate, m_i, as M_i^{n+1}/f_i^{n+1}. When $f_i^{n+1} = 0$ and/or $M_i^{n+1} = 0$, the mass coordinate, m_i, remains unchanged.

In the case with $l = i$, then f_k decreases by $\nu_{ki}\Delta t$, f_i remains unchanged (i.e., $f_i^{n+1} = f_i^n$), M_k decreases by $m_k \nu_{ki}\Delta t$, and M_i increases by $m_k \nu_{ki}\Delta t$.

When m_{i+1} becomes larger than ${\delta_m}^2 m_i$ and M_{399}^n is zero, then we redefine the new mass

coordinates, $m_{i,\,\mathrm{new}}$, as

$$\begin{aligned}
&m_{i,\,\mathrm{new}} = m_i,\\
&m_{i+1,\,\mathrm{new}} = \delta_m m_i,\\
&m_{i+2,\,\mathrm{new}} = m_{i+1},\\
&m_{i+3,\,\mathrm{new}} = m_{i+2},\ m_{i+4,\,\mathrm{new}} = m_{i+3},\ \ldots,\ m_{398,\,\mathrm{new}} = m_{397},\ \text{and}\\
&m_{399,\,\mathrm{new}} = m_{398},
\end{aligned} \tag{D.18}$$

and the new thickness of the grid as

$$\Delta m_{i,\,\mathrm{new}} = (m_{i+1,\,\mathrm{new}} - m_{i-1,\,\mathrm{new}})/2. \tag{D.19}$$

We define $M^n_{i,\,\mathrm{new}}$ as

$$\begin{aligned}
&M^n_{i,\,\mathrm{new}} = M^n_i \Delta m_{i,\,\mathrm{new}}/\Delta m_i,\\
&M^n_{i+1,\,\mathrm{new}} = M^n_i - M^n_{i,\,\mathrm{new}} + M^n_{i+1} - M^n_{i+2,\,\mathrm{new}},\\
&M^n_{i+2,\,\mathrm{new}} = M^n_{i+1} \Delta m_{i+2,\,\mathrm{new}}/\Delta m_{i+1},\\
&M^n_{i+3,\,\mathrm{new}} = M^n_{i+2},\ M^n_{i+4,\,\mathrm{new}} = M^n_{i+3},\ \ldots,\ M^n_{398,\,\mathrm{new}} = M^n_{397},\ \text{and}\\
&M^n_{399,\,\mathrm{new}} = M^n_{398} + M^n_{399},
\end{aligned} \tag{D.20}$$

and $f^n_{i,\,\mathrm{new}}$ as

$$\begin{aligned}
&f^n_{i,\,\mathrm{new}} = M^n_{i,\,\mathrm{new}}/m_{i,\,\mathrm{new}},\\
&f^n_{i+1,\,\mathrm{new}} = M^n_{i+1,\,\mathrm{new}}/m_{i+1,\,\mathrm{new}},\\
&f^n_{i+2,\,\mathrm{new}} = M^n_{i+2,\,\mathrm{new}}/m_{i+2,\,\mathrm{new}},\\
&f^n_{i+3,\,\mathrm{new}} = f^n_{i+2},\ f^n_{i+4,\,\mathrm{new}} = f^n_{i+3},\ \ldots,\ f^n_{398,\,\mathrm{new}} = f^n_{397},\ \text{and}\\
&f^n_{399,\,\mathrm{new}} = M^n_{399,\,\mathrm{new}}/m_{399,\,\mathrm{new}}.
\end{aligned} \tag{D.21}$$

On the other hand, when m_{i+1} becomes larger than ${\delta_m}^2 m_i$ and M^n_{399} is not zero, then we define $\delta_{m,\,\mathrm{new}}$ as

$$\delta_{m,\,\mathrm{new}} = {\delta_m}^{3/2}. \tag{D.22}$$

When m_{i+1} becomes smaller than ${\delta_m}^{1/2} m_i$, on the other hand, then we redefine the new mass coordinates, $m_{i,\,\mathrm{new}}$, as

$$\begin{aligned} &m_{i,\,\mathrm{new}} = m_{i+1}, \\ &m_{i+1,\,\mathrm{new}} = m_{i+2}, \\ &m_{i+2,\,\mathrm{new}} = m_{i+3},\ m_{i+3,\,\mathrm{new}} = m_{i+4},\ \ldots,\ m_{398,\,\mathrm{new}} = m_{399},\ \text{and} \\ &m_{399,\,\mathrm{new}} = \delta_m m_{399}. \end{aligned} \tag{D.23}$$

We define $M^n_{i,\,\mathrm{new}}$ as

$$\begin{aligned} &M^n_{i,\,\mathrm{new}} = M^n_i + M^n_{i+1}(m_{i+1,\,\mathrm{new}} - m_{i+1})/2\Delta m_{i+1}, \\ &M^n_{i+1,\,\mathrm{new}} = M^n_{i+2} + M^n_{i+1}(m_{i+1} - m_{i,\,\mathrm{new}})/2\Delta m_{i+1}, \\ &M^n_{i+2,\,\mathrm{new}} = M^n_{i+3},\ M^n_{i+3,\,\mathrm{new}} = M^n_{i+4},\ \ldots,\ M^n_{398,\,\mathrm{new}} = M^n_{399},\ \text{and} \\ &M^n_{399,\,\mathrm{new}} = 0, \end{aligned} \tag{D.24}$$

and $f^n_{i,\,\mathrm{new}}$ as

$$\begin{aligned} &f^n_{i,\,\mathrm{new}} = M^n_{i,\,\mathrm{new}}/m_{i,\,\mathrm{new}}, \\ &f^n_{i+1,\,\mathrm{new}} = M^n_{i+1,\,\mathrm{new}}/m_{i+1,\,\mathrm{new}}, \\ &f^n_{i+2,\,\mathrm{new}} = f^n_{i+3},\ f^n_{i+3,\,\mathrm{new}} = f^n_{i+4},\ \ldots,\ f^n_{398,\,\mathrm{new}} = f^n_{399},\ \text{and} \\ &f^n_{399,\,\mathrm{new}} = 0. \end{aligned} \tag{D.25}$$

D.3.2 Test Calculation

We consider the case with

$$K(m, m') = m + m', \tag{D.26}$$

and adopt the initial condition that is given by

$$f(t=0, m) = \begin{cases} 1 & (m = m_0 = 1) \\ 0 & (m \neq m_0) \end{cases}. \tag{D.27}$$

For the case with equations (D.26) and (D.27), the analytical solution is given by

$$f(t, m) = \frac{m^{m-1}}{m!} e^{-t} (1 - e^{-t})^{m-1} \exp[-m(1 - e^{-t})], \tag{D.28}$$

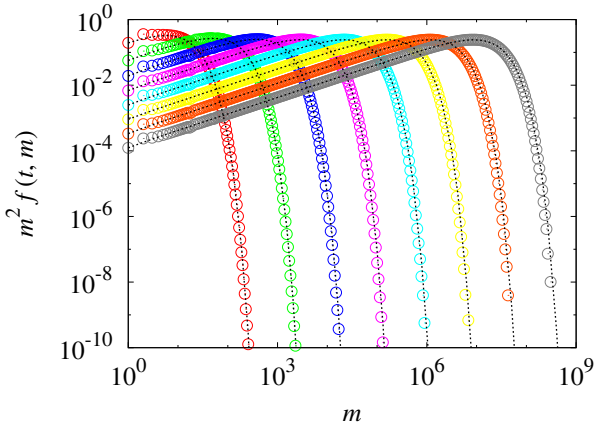

Figure D.2: Results of a test of our numerical method for the growth of bodies at $t = 1$ (red), 2 (green), 3 (blue), 4 (magenta), 5 (cyan), 6 (yellow), 7 (orange) and 8 (gray), respectively. Numerical results (circles) are compared with analytic solutions by Trubnikov (1971) (black dotted lines). The monochrome version of this figure was presented in Hasegawa & Tsuribe (2013) as figure 5.

(Trubnikov 1971). The initial mass coordinate is given by equation (D.3). We set $\delta_m = 1.1$ and $\Delta t = 10^{-3}$. Figure D.2 shows the results with our numerical method for the growth of bodies. In figure D.2, it is seen that our numerical method gives satisfactory results in the calculation of the growth of dust aggregates.

Appendix E

Linear Stability Analysis of Laminar Flow for KHI

We present the linear stability analysis of the laminar flow for KHI (Chandrasekhar 1961). We assume that there is one component fluid and that the fluid is incompressible and inviscid. We consider the Cartesian coordinate system (x, y, z) at rest, and assume that there are a laminar flow in the direction of y and the gravitational force in the negative direction of z. We also assume that the gravitational acceleration is spatially and temporally constant. The governing equations are given as

$$\frac{\partial u}{\partial x} + \frac{\partial v}{\partial y} + \frac{\partial w}{\partial z} = 0, \tag{E.1}$$

$$\frac{\partial \rho}{\partial t} + u\frac{\partial \rho}{\partial x} + v\frac{\partial \rho}{\partial y} + w\frac{\partial \rho}{\partial z} = 0, \tag{E.2}$$

$$\frac{\partial u}{\partial t} + u\frac{\partial u}{\partial x} + v\frac{\partial u}{\partial y} + w\frac{\partial u}{\partial z} = -\frac{1}{\rho}\frac{\partial P}{\partial x}, \tag{E.3}$$

$$\frac{\partial v}{\partial t} + u\frac{\partial v}{\partial x} + v\frac{\partial v}{\partial y} + w\frac{\partial v}{\partial z} = -\frac{1}{\rho}\frac{\partial P}{\partial y}, \tag{E.4}$$

and

$$\frac{\partial w}{\partial t} + u\frac{\partial w}{\partial x} + v\frac{\partial w}{\partial y} + w\frac{\partial w}{\partial z} = -\frac{1}{\rho}\frac{\partial P}{\partial z} - g_z, \tag{E.5}$$

where t is the time, (u, v, w) are the (x, y, z) components of the velocity, ρ is the density of the fluid, P is the pressure, and $g_z = \text{const} > 0$ is the constant acceleration due to the gravitational force.

We assume that the unperturbed state is steady and uniform in y direction, and that the x and z components of the unperturbed velocity are zero. Then, we have

$$u_0 = 0,\ v_0 = v_0(z),\ w_0 = 0,\ \rho_0 = \rho_0(z),\ \text{and}\ P_0 = P_0(z), \tag{E.6}$$

where subscript 0 refers the unperturbed quantities. For the unperturbed state, from equations (E.5) and (E.6), we have

$$0 = -\frac{1}{\rho_0}\frac{dP_0}{dz} - g_z. \tag{E.7}$$

To obtain the linear perturbation equations, we write the quantities as $f = f_0 + f_1$, where subscript 1 refers the perturbed quantities, and neglect the second-order terms of the perturbed quantities. For the perturbed state, from equations (E.1)-(E.7), we have

$$\frac{\partial u_1}{\partial x} + \frac{\partial v_1}{\partial y} + \frac{\partial w_1}{\partial z} = 0, \tag{E.8}$$

$$\frac{\partial \rho_1}{\partial t} + v_0\frac{\partial \rho_1}{\partial y} + w_1\frac{d\rho_0}{dz} = 0, \tag{E.9}$$

$$\frac{\partial u_1}{\partial t} + v_0\frac{\partial u_1}{\partial y} = -\frac{1}{\rho_0}\frac{\partial P_1}{\partial x}, \tag{E.10}$$

$$\frac{\partial v_1}{\partial t} + v_0\frac{\partial v_1}{\partial y} + w_1\frac{dv_0}{dz} = -\frac{1}{\rho_0}\frac{\partial P_1}{\partial y}, \tag{E.11}$$

and

$$\frac{\partial w_1}{\partial t} + v_0\frac{\partial w_1}{\partial y} = -\frac{1}{\rho_0}\frac{\partial P_1}{\partial z} - g_z\frac{\rho_1}{\rho_0}. \tag{E.12}$$

Perturbed quantities are assumed to have the form as $f_1 = \hat{f}_1(z)\exp[i(k_x x + k_y y - \omega t)]$, where k_x is the wave number in the direction of x, k_y is the wave number in the direction of y, and $\omega \equiv \omega_r + i\omega_i$ is the complex angular frequency. Hereafter $\hat{}$ is omitted, and equations (E.8)-(E.12) are given by

$$ik_x u_1 + ik_y v_1 + D_z w_1 = 0, \tag{E.13}$$

$$-i\omega\rho_1 + ik_y v_0\rho_1 + w_1 D_z\rho_0 = 0, \tag{E.14}$$

$$-i\omega u_1 + ik_y v_0 u_1 = -ik_x\frac{P_1}{\rho_0}, \tag{E.15}$$

$$-i\omega v_1 + ik_y v_0 v_1 + w_1 D_z v_0 = -ik_y\frac{P_1}{\rho_0}, \tag{E.16}$$

and

$$-i\omega w_1 + ik_y v_0 w_1 = -\frac{1}{\rho_0}D_z P_1 - g_z\frac{\rho_1}{\rho_0}, \tag{E.17}$$

where $D_z \equiv d/dz$.

Multiplying equations (E.15) and (E.16) by $ik_x\rho_0$ and $ik_y\rho_0$, respectively, we have

$$\rho_0\bar{\omega}k_x u_1 = {k_x}^2 P_1, \tag{E.18}$$

and

$$\rho_0\bar{\omega}k_y v_1 + i\rho_0 k_y(D_z v_0)w_1 = {k_y}^2 P_1, \tag{E.19}$$

where $\bar{\omega} \equiv \omega - k_y v_0$. From equations (E.13), (E.18) and (E.19), we have

$$D_z[i\rho_0\bar{\omega}D_z w_1 + i\rho_0 k_y(D_z v_0)w_1] = k^2 D_z P_1, \tag{E.20}$$

where $k^2 \equiv {k_x}^2 + {k_y}^2$. Multiplying equation (E.17) by $-k^2\rho_0$, we have

$$i\rho_0\bar{\omega}k^2 w_1 = k^2 D_z P_1 + g_z k^2\rho_1. \tag{E.21}$$

From equations (E.14), (E.20) and (E.21), we have

$$D_z[\rho_0\bar{\omega}D_z w_1 + \rho_0 k_y(D_z v_0)w_1] - \rho_0\bar{\omega}k^2 w_1 = g_z k^2(D_z\rho_0)\frac{w_1}{\bar{\omega}}. \tag{E.22}$$

For simplicity, we consider the case when there are laminar flows of two superposed fluids with a relative horizontal velocity. To obtain the boundary condition at the boundary surface of laminar flows, we suppose that there is a boundary surface of laminar flows at $z = z_{\rm s}$. For the unperturbed state, $z_{\rm s} = z_{\rm s0}$ is a constant value. The equation of motion for the boundary surface is given as

$$\frac{\partial z_{\rm s}}{\partial t} + u(z_{\rm s})\frac{\partial z_{\rm s}}{\partial x} + v(z_{\rm s})\frac{\partial z_{\rm s}}{\partial y} + w(z_{\rm s})\frac{\partial z_{\rm s}}{\partial z} = w(z_{\rm s}). \tag{E.23}$$

In the perturbed state, the surface becomes slightly deformed. We define the deformed surface by $z_{\rm s} = z_{\rm s0} + z_{\rm s1}$. From equation (E.23), the equation of motion for the deformed surface is given as

$$\frac{\partial z_{\rm s1}}{\partial t} + v_0(z_{\rm s0})\frac{\partial z_{\rm s1}}{\partial y} = w_1(z_{\rm s0}). \tag{E.24}$$

In equation (E.24), we use the following expansions:

$$v_0(z_{\rm s0} + z_{\rm s1}) = v_0(z_{\rm s0}) + \left.\frac{dv_0}{dz}\right|_{z=z_{\rm s0}} z_{\rm s1}, \tag{E.25}$$

and

$$w_1(z_{\rm s0} + z_{\rm s1}) = w_1(z_{\rm s0}) + \left.\frac{dw_1}{dz}\right|_{z=z_{\rm s0}} z_{\rm s1} = w_1(z_{\rm s0}). \tag{E.26}$$

We assume that the perturbed quantity $z_{\rm s1}$ is given as $z_{\rm s1} = z_{\rm s1}(z)\exp[i(k_x x + k_y y - \omega t)]$, then we have

$$-i\omega z_{\rm s1} + ik_y v_0(z_{\rm s0}) z_{\rm s1} = w_1(z_{\rm s0}). \tag{E.27}$$

From equation (E.27), we have

$$z_{\rm s1} = \left.\frac{iw_1}{\bar{\omega}}\right|_{z=z_{\rm s0}}. \tag{E.28}$$

Equation (E.28) shows that $w_1/\bar{\omega}$ must be continuous at the boundary surface of laminar flows.

To obtain the condition at the boundary surface, $z = z_{\rm s}$, we integrate equation (E.22) over an infinitesimal element $(z_{\rm s0} - \epsilon, z_{\rm s0} + \epsilon)$ and pass to the limit $\epsilon \to 0$. Since gk^2 and $w_1/\bar{\omega}$ are continuous at the boundary surface, we obtain the condition at the boundary surface as

$$\Delta_{\rm s0}[\rho_0\bar{\omega}D_z w_1 + \rho_0 k_y (D_z v_0) w_1] = g_z k^2 [\Delta_{\rm s0}(\rho_0)] \left.\left(\frac{w_1}{\bar{\omega}}\right)\right|_{z=z_{\rm s0}}, \tag{E.29}$$

where

$$\Delta_{\rm s0}(F) \equiv F(z = z_{\rm s0} + 0) - F(z = z_{\rm s0} - 0) = \lim_{\epsilon\to 0}\int_{z-\epsilon}^{z+\epsilon} D_z F dz. \tag{E.30}$$

We set $z_{\rm s0} = 0$ and consider the case with

$$v_0(z) = \begin{cases} v_+ & (z > 0) \\ v_- & (z < 0) \end{cases}, \tag{E.31}$$

and

$$\rho_0(z) = \begin{cases} \rho_+ & (z > 0) \\ \rho_- & (z < 0) \end{cases} . \tag{E.32}$$

Then, $D_z v_0 = 0$ and $D_z \rho_0 = 0$ at $z \neq 0$. We assume that $v_+ \neq v_-$ and that $\rho_+ \leq \rho_-$. From equation (E.22), we have

$$D_z^2 w_1 - k^2 w_1 = 0. \tag{E.33}$$

The general solution of equation (E.33) is a linear combination of e^{kz} and e^{-kz}. We assume the boundary condition that w_1 is zero at $z \to \pm\infty$. From equation (E.28), $w_1/\bar{\omega}$ is continuous at $z = 0$. Then, we obtain the solution of equation (E.33) as

$$w_1(z) = \begin{cases} A(\omega - k_y v_+)e^{-kz} & (z > 0) \\ A(\omega - k_y v_-)e^{kz} & (z < 0) \end{cases} , \tag{E.34}$$

where A is a integral constant. From equation (E.34), we have

$$\left(\frac{w_1}{\bar{\omega}}\right)\Big|_{z=0} = A. \tag{E.35}$$

From equations (E.29)-(E.32), (E.34) and (E.35), we obtain the dispersion relation as

$$(\rho_+ + \rho_-)\omega^2 - 2k_y(\rho_+ v_+ + \rho_- v_-)\omega + {k_y}^2(\rho_+ {v_+}^2 + \rho_- {v_-}^2) - g_z k(\rho_- - \rho_+) = 0. \tag{E.36}$$

The roots of equation (E.36) are given by

$$\omega = \frac{k_y(\rho_+ v_+ + \rho_- v_-) \pm i\sqrt{{k_y}^2 \rho_+ \rho_- (v_- - v_+)^2 - g_z k({\rho_-}^2 - {\rho_+}^2)}}{\rho_+ + \rho_-}. \tag{E.37}$$

From equation (E.37), instability occurs for the modes with

$${k_y}^2 \rho_+ \rho_- (v_- - v_+)^2 - g_z k({\rho_-}^2 - {\rho_+}^2) > 0. \tag{E.38}$$

Therefore, two uniform fluids in a horizontal relative motion separated by a horizontal boundary surface is unstable, and this is called the Kelvin-Helmholtz instability (KHI). Since $g_z > 0$ and $\rho_+ \leq \rho_-$, equation (E.38) is rewritten as

$$k > k_{\min}(k_x) \equiv \frac{g_z}{(v_- - v_+)^2} \frac{{\rho_-}^2 - {\rho_+}^2}{\rho_+ \rho_-} \frac{k^2}{{k_y}^2} \geq k_{\min}(0) = \frac{g_z}{(v_- - v_+)^2} \frac{{\rho_-}^2 - {\rho_+}^2}{\rho_+ \rho_-} > 0. \tag{E.39}$$

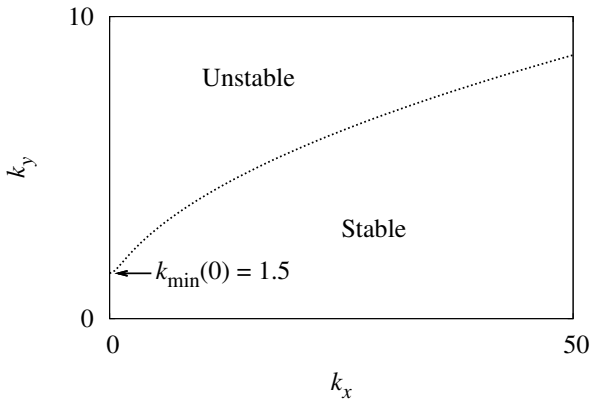

Figure E.1: The stability and instability of laminar flows of two fluids in the case with $v_+ = 1$, $v_- = 2$, $\rho_+ = 1$, $\rho_- = 2$ and $g_z = 1$.

Figure E.1 shows the stability and instability of laminar flows of two fluids in the case with $v_+ = 1$, $v_- = 2$, $\rho_+ = 1$, $\rho_- = 2$ and $g_z = 1$. For the mode with $k_y = 0$, then $k_{\min}(\propto k^2/{k_y}^2) = +\infty$ [equation (E.39)]. For such a mode, the finite wave number k $(= k_x)$ can not become larger than $k_{\min}$, then two uniform fluids are stable. Thus, perturbations perpendicular to the direction of flows can not cause KHI. We explain this result by the process of the onset of KHI described in subsection 1.5.2. The surplus energy results from the momentum transfer between the regions with different unperturbed velocities in fluctuation of the plane interface. Even if the surplus energy causes the x-component of fluctuation, the momentum transfer does not occur because the x-component of the unperturbed velocity is zero. Then, the amplitude of fluctuation in the direction of z is not amplified. Thus, KHI does not occur if the wave number in the direction of x, k_x, become large.

The real part of the complex angular frequency is given by

$$\omega_r = \begin{cases} k_y(\rho_+ v_+ + \rho_- v_-)/(\rho_+ + \rho_-) & [k > k_{\min}(k_x)] \\ k_y(\rho_+ v_+ + \rho_- v_-)/(\rho_+ + \rho_-) & \\ \quad \pm \sqrt{g_z k(\rho_-{}^2 - \rho_+{}^2) - {k_y}^2 \rho_+ \rho_- (v_- - v_+)^2}/(\rho_+ + \rho_-) & [k \leq k_{\min}(k_x)] \end{cases}, \quad \text{(E.40)}$$

and the imaginary part of the complex angular frequency that corresponds to the growth rate

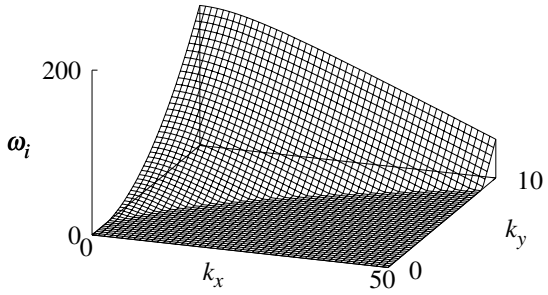

Figure E.2: Growth rates of KHI in the case with $v_+ = 1$, $v_- = 2$, $\rho_+ = 1$, $\rho_- = 2$ and $g_z = 1$.

of KHI is given by

$$\omega_i = \begin{cases} \pm\sqrt{{k_y}^2\rho_+\rho_-(v_- - v_+)^2 - g_z k({\rho_-}^2 - {\rho_+}^2)}/(\rho_+ + \rho_-) & [k > k_{\min}(k_x)] \\ 0 & [k \leq k_{\min}(k_x)] \end{cases}, \tag{E.41}$$

The mode with the negative growth rate of KHI decays with increaseing time. Thus, we only consider the positive growth rate of KHI.

Figure E.2 shows positive growth rates of KHI in the case with $v_+ = 1$, $v_- = 2$, $\rho_+ = 1$, $\rho_- = 2$ and $g_z = 1$. From Figure E.2, it is shown that the growth rate, ω_i, decreases with increasing the wave number in the direction of x, k_x. Thus, the mode with $k_x = 0$ is the most unstable.

Next, we consider the effect of rotation on the development of KHI. We adopt the local Cartesian coordinate system (x, y, z) rotating with an uniform angular velocity $\mathbf{\Omega} = (0, 0, \Omega)$. Then, equations (E.10) and (E.11) are replaced by

$$\frac{\partial u_1}{\partial t} + v_0\frac{\partial u_1}{\partial y} - 2\Omega v_1 = -\frac{1}{\rho_0}\frac{\partial P_1}{\partial x}, \tag{E.42}$$

and

$$\frac{\partial v_1}{\partial t} + v_0\frac{\partial v_1}{\partial y} + w_1\frac{dv_0}{dz} + 2\Omega u_1 = -\frac{1}{\rho_0}\frac{\partial P_1}{\partial y}. \tag{E.43}$$

In these equations, we neglect the tidal force. Then, equation (E.29) is replaced by

$$\Delta_{\rm s0}\left[\rho_0\bar{\omega}\left(1-\frac{4\Omega^2}{\bar{\omega}^2}\right)D_z w_1+\left(1+\frac{2i\Omega}{\bar{\omega}}\right)\rho_0 k_y(D_z v_0)w_1\right]=g_z k^2[\Delta_{\rm s0}(\rho_0)]\left(\frac{w_1}{\bar{\omega}}\right)\Big|_{z=z_{\rm s0}}. \quad \text{(E.44)}$$

From equation (E.44), we have

$$w_1(z)=\begin{cases} A(\omega-k_y v_+)\exp(-\kappa_+ z) & (z>0) \\ A(\omega-k_y v_-)\exp(\kappa_- z) & (z<0) \end{cases}, \quad \text{(E.45)}$$

where

$$\kappa_\pm \equiv k\left[1-\frac{4\Omega^2}{(\omega-k_y v_\pm)^2}\right]^{-1/2}. \quad \text{(E.46)}$$

We consider the most unstable mode with $k_x=0$. The dispersion relation is given by

$$\rho_+(\omega-k_y v_+)^2\left[1-\frac{4\Omega^2}{(\omega-k_y v_+)^2}\right]^{1/2}+\rho_-(\omega-k_y v_-)^2\left[1-\frac{4\Omega^2}{(\omega-k_y v_-)^2}\right]^{1/2}=g_z k_y(\rho_- -\rho_+). \quad \text{(E.47)}$$

For simplicity, we consider the case with $\rho_+=\rho_-$. Then, we obtain the angular frequency as

$$\omega=\frac{k_y(v_+ +v_-)\pm i\sqrt{{k_y}^2(v_- -v_+)^2-8\Omega^2}}{2}, \quad \text{(E.48)}$$

and the growth rate of KHI is given as

$$\omega_i=\frac{1}{2}\sqrt{{k_y}^2(v_- -v_+)^2-8\Omega^2}. \quad \text{(E.49)}$$

Equation (E.49) shows that rotation decreases the growth rate of KHI.

Appendix F

Typical Size of Dust Aggregates in the Dust Sedimentation with Growth

We explain the reason that the typical size of dust aggregates $\bar{s}(z)$ is a linear function of z at $z/H_{\rm g} \ll 1$ and at $t/t_{\rm sed} \ll 1$ owing to collisions due to sedimentation in the case with growth of dust aggregates (Hasegawa & Tsuribe 2013). We now estimate the mean collision time by the same method as that used in Nakagawa et al. (1981). The mean collision time is given by

$$t_{\rm coll} = \frac{1}{n_{\rm d}\sigma\Delta v}, \tag{F.1}$$

where $n_{\rm d}$ is the number density of dust aggregates, σ is the collisional cross section and Δv is the relative velocity of the dust-dust collision. We assume that the sizes of dust aggregates are given by the typical size, and that masses of dust aggregates are given by the typical mass of dust aggregates. The typical mass is given by

$$\bar{m}(z) = \frac{4}{3}\pi\rho_{\rm s}[\bar{s}(z)]^3, \tag{F.2}$$

and we regard that $\sigma = \pi\bar{s}^2$. We treat $n_{\rm d}$ as $\rho_{\rm d}/\bar{m}$ or $(\Sigma_d/\Sigma_g)[\rho_{\rm g}/\bar{m}]$ at $z/H_{\rm g} \ll 1$ and at $t/t_{\rm sed} \ll 1$. For the collision due to sedimentation, we simply put $|s - s'| = \bar{s}$ and $\Delta v = \Delta v_{\rm s}$. The mean collision time for sedimentation is defined as $t_{\rm coll,\,s}$. At $z/H_{\rm g} \ll 1$ and at $t/t_{\rm sed} \ll 1$,

$t_{\mathrm{coll,\,s}}$ is obtained as

$$t_{\mathrm{coll,\,s}} = \frac{2\sqrt{2}}{3}\frac{\Sigma_{\mathrm{g}}}{\Sigma_{\mathrm{d}}}\frac{1}{\Omega_{\mathrm{K}}}\left(\frac{z}{H_{\mathrm{g}}}\right)^{-1} = 36\left(\frac{z}{H_{\mathrm{g}}}\right)^{-1}\ [\mathrm{year}]. \tag{F.3}$$

In equation (F.3), it can be seen that $t_{\mathrm{coll,\,s}}$ is independent of $\bar{s}$, and that $t_{\mathrm{coll,\,s}} \propto z^{-1}$. For collisions due to the thermal motion, we simply put $m = m' = \bar{m}$ and $\Delta v = \Delta v_{\mathrm{B}}$. The mean collision time for the thermal motion, $t_{\mathrm{coll,\,B}}$, is obtained by

$$t_{\mathrm{coll,\,B}} = \frac{4}{3}\sqrt{\frac{2}{3}}\frac{\pi H_{\mathrm{g}}}{\Sigma_{\mathrm{d}}}\frac{{\rho_{\mathrm{s}}}^{\frac{3}{2}}{s_0}^{\frac{5}{2}}}{\sqrt{k_{\mathrm{B}}T}}\left(\frac{\bar{s}}{s_0}\right)^{\frac{5}{2}}\exp\left[\left(\frac{z}{H_{\mathrm{g}}}\right)^2\right] = 28\left(\frac{\bar{s}}{s_0}\right)^{\frac{5}{2}}\ [\mathrm{year}], \tag{F.4}$$

at $z/H_{\mathrm{g}} \ll 1$ and at $t/t_{\mathrm{sed}} \ll 1$. In equation (F.4), it can be seen that $t_{\mathrm{coll,\,B}}$ is independent of z and $t_{\mathrm{coll,\,B}} \propto \bar{s}^{\,5/2}$ at $z/H_{\mathrm{g}} \ll 1$ and at $t/t_{\mathrm{sed}} \ll 1$.

From equations (F.3) and (F.4), it is found that $t_{\mathrm{coll,\,B}} < t_{\mathrm{coll,\,s}}$ when sizes of dust aggregates are small. Therefore, it is expected that collisions due to thermal motion dominate as long as the sizes of the dust aggregates are small. After dust aggregates have grown, it is expected that $t_{\mathrm{coll,\,B}} > t_{\mathrm{coll,\,s}}$, and that collisions due to sedimentation dominate. The growing speed of dust aggregates in sedimentation is expected to be proportional to z because $t_{\mathrm{coll,\,s}} \propto z^{-1}$. Thus, it is supposed that the typical mass of dust aggregates at z, $\bar{m}(z)$, is given by

$$\bar{m}(z) = \left(a_1 \times \frac{z}{H_{\mathrm{g}}} + a_2\right) m_0, \tag{F.5}$$

where a_1 and a_2 are appropriate values. Then, the typical size of dust aggregates at z is given by $\bar{s}(z) = [a_1(z/H_{\mathrm{g}}) + a_2]^{1/3} s_0$. If $a_1 z/a_2 H_{\mathrm{g}} \ll 1$, it is supposed that $\bar{s}(z)$ is approximated by

$$\bar{s}(z) = \left(a_3 \times \frac{z}{H_{\mathrm{g}}} + a_4\right) s_0, \tag{F.6}$$

with the Taylor expansion. Symbols a_3 and a_4 are appropriate values.

Figure F.1 shows the distribution of the typical mass and size of dust aggregates at $z/H_{\mathrm{g}} \ll 1$ and at $t = 25$ year in numerical results in subsection 3.2.1. From figure F.1, it is confirmed the functional form of $\bar{s}(z) = [a_3(z/H_{\mathrm{g}}) + a_4]s_0$ at $z/H_{\mathrm{g}} \ll 1$ and at $t/t_{\mathrm{sed}} \ll 1$.

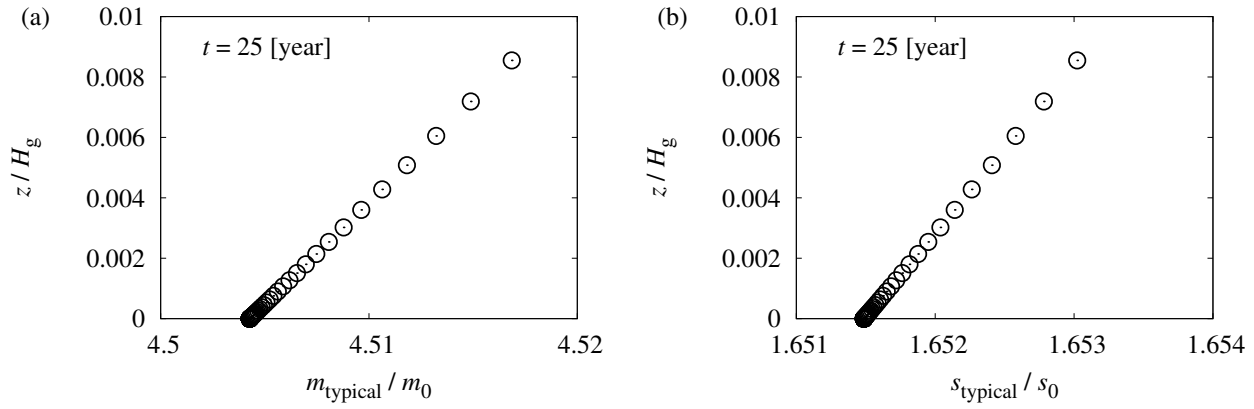

Figure F.1: (a) Distribution of the typical mass of dust aggregates in $r = 1$ AU at $t = 25$ year. The abscissa, where $m_{\rm typical}$ means $\bar{m}$, shows the typical mass, $\bar{m}$, in units of m_0. The ordinate shows z coordinate in units of $H_{\rm g}$. (b) Distribution of the typical size of dust aggregates at $t = 25$ year. The abscissa, where $s_{\rm typical}$ means $\bar{s}$, shows the typical size, $\bar{s}$, in units of s_0. The ordinate shows z coordinate in units of $H_{\rm g}$. This figure was presented in Hasegawa & Tsuribe (2013) as figure 14.

The above discussions assume that collisions due to sedimentation become more dominant than those due to the thermal motion. However, it is not confirmed that collisions due to sedimentation are dominant before $t = 25$ year. We should now confirm that the dominant effect in the growth of dust aggregates is sedimentation at $t = 25$ year.

At $z/H_{\rm g} \ll 1$ and $t \approx 0$, it is expected that collisions due to the thermal motion are dominant, and that $t_{\rm coll,\,B}$ is independent of z. In this case, it is supposed that the typical size of dust aggregates is independent of z, i.e., a_3 in the formula for $\bar{s}(z)$ is temporally constant. However, in a certain time, it is expected that the dominant effect in the growth of dust aggregates changes from collisions due to the thermal motion to those due to sedimentation because of dust growth. Therefore, the time for this change can be determined by investigating the time development of a_3 for $\bar{s}(z)$.

Figure F.2 shows the time development of a_3. In figure F.2, a_3 is approximated by $a_3 = 6.3\times10^{-5}(t/1\ [\rm yr])^2 + 7.0\times10^{-3}(t/1\ [\rm yr]) - 3.0\times10^{-2}$. This shows that $a_3 > 0$ at $t \gtrsim 4$ yr, then it is expected that collisions due to sedimentation dominate in the growth of dust aggregates

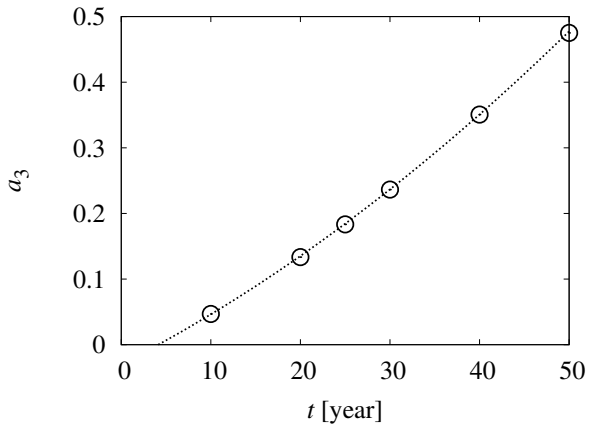

Figure F.2: The time development of a_3 (circles) in $r = 1$ AU and $z/H_{\rm g} \ll 1$ at $t/t_{\rm sed} \ll 1$. The abscissa shows time and the ordinate shows a_3 that is derived from fitting $\bar{s}(z)$ into $[a_3(z/H_{\rm g}) + a_4]s_0$. The approximated curve is also drawn (dotted line). This figure was presented in Hasegawa & Tsuribe (2013) as figure 15.

at $t \gtrsim 4$ yr. Therefore, we conclude that the assumption that collisions due to sedimentation become more dominant than those due to the thermal motion is appropriate at $t = 25$ yr.

Appendix G

Linear Perturbation Equation for KHI

We present the derivation of a set of linear perturbation equations for KHI for a fluid with a continuous density distribution in the protoplanetary disk (Sekiya & Ishitsu 2000). We assume that there is one component fluid and that the fluid is incompressible and inviscid. We assume that the protoplanetary disk is axisymmetric with respect to the rotational axis of the disk. We adopt the local Cartesian coordinate system (x, y, z) rotating around a central star with the constant azimuthal velocity. The curvature is neglected. We take into account only the gravitational force from the central star and neglect the self-gravity of the fluid. For simplicity, we assume $\partial\Omega_{\rm K}/\partial z = 0$, where $\Omega_{\rm K}$ is the Keplerian angular velocity. The Coriolis and tidal forces are neglected. The governing equations are the equation of continuity, the equation of incompressibility and equations of motion, and are given as

$$\frac{\partial u}{\partial x} + \frac{\partial v}{\partial y} + \frac{\partial w}{\partial z} = 0, \tag{G.1}$$

$$\frac{\partial \rho}{\partial t} + u\frac{\partial \rho}{\partial x} + v\frac{\partial \rho}{\partial y} + w\frac{\partial \rho}{\partial z} = 0, \tag{G.2}$$

$$\frac{\partial u}{\partial t} + u\frac{\partial u}{\partial x} + v\frac{\partial u}{\partial y} + w\frac{\partial u}{\partial z} = -\frac{1}{\rho}\frac{\partial P}{\partial x}, \tag{G.3}$$

$$\frac{\partial v}{\partial t} + u\frac{\partial v}{\partial x} + v\frac{\partial v}{\partial y} + w\frac{\partial v}{\partial z} = -\frac{1}{\rho}\frac{\partial P}{\partial y}, \tag{G.4}$$

and

$$\frac{\partial w}{\partial t} + u\frac{\partial w}{\partial x} + v\frac{\partial w}{\partial y} + w\frac{\partial w}{\partial z} = -\frac{1}{\rho}\frac{\partial P}{\partial z} - {\Omega_{\rm K}}^2 z, \tag{G.5}$$

where t is the time, (u, v, w) are the (x, y, z) components of the velocity, ρ is the density of the fluid and P is the pressure. Equations (G.1)-(G.5) are the same as equations (E.1)-(E.5), except for $g_z = {\Omega_{\rm K}}^2 z$ and $\partial g_z/\partial z \neq 0$.

We consider the case when the unperturbed velocity, density and pressure are given by equation (E.6), i.e.,

$$u_0 = 0,\ v_0 = v_0(z),\ w_0 = 0,\ \rho_0 = \rho_0(z),\ \text{and}\ P_0 = P_0(z). \tag{G.6}$$

Subscript 0 refers the unperturbed quantities, and subscript 1 refers the perturbed quantities. To obtain the linear perturbation equations, we give the quantities as $f = f_0 + f_1$ and neglect the second-order terms of the perturbed quantities. Perturbed quantities are assumed to have the form as $f_1 = \hat{f}_1(z)\exp[i(k_x x + k_y y - \omega t)]$, where k_x is the wave number in the direction of x, k_y is the wave number in the direction of y, and $\omega \equiv \omega_r + i\omega_i$ is the complex angular frequency. Hereafter $\hat{}$ is omitted, then equations (G.1)-(G.5) are replaced by equations (E.13)-(E.17), i.e.,

$$ik_x u_1 + ik_y v_1 + \frac{dw_1}{dz} = 0, \tag{G.7}$$

$$-i\bar{\omega}\rho_1 + \frac{d\rho_0}{dz}w_1 = 0, \tag{G.8}$$

$$-i\bar{\omega}u_1 = -ik_x\frac{P_1}{\rho_0}, \tag{G.9}$$

$$-i\bar{\omega}v_1 + \frac{dv_0}{dz}w_1 = -ik_y\frac{P_1}{\rho_0}, \tag{G.10}$$

and

$$-i\bar{\omega}w_1 = -\frac{1}{\rho_0}\frac{dP_1}{dz} - \frac{{\Omega_{\rm K}}^2 z}{\rho_0}\rho_1, \tag{G.11}$$

where $\bar{\omega} \equiv \omega - k_y v_0$, and the linear perturbation equation is given by equation (E.22), i.e.,

$$\frac{d^2 w_1}{dz^2} + \frac{1}{\rho_0}\frac{d\rho_0}{dz}\frac{dw_1}{dz} - \left(k^2 + \frac{1}{\bar{v}}\frac{d^2 v_0}{dz^2} + \frac{1}{\rho_0}\frac{d\rho_0}{dz}\frac{1}{\bar{v}}\frac{dv_0}{dz} + \frac{k^2}{{k_y}^2}\frac{{\Omega_{\rm K}}^2 z}{\bar{v}^2}\frac{1}{\rho_0}\frac{d\rho_0}{dz}\right)w_1 = 0, \tag{G.12}$$

where $k^2 \equiv {k_x}^2 + {k_y}^2$ and $\bar{v} \equiv v_0 - \omega/k_y = -\bar{\omega}/k_y$. Equations (G.7)-(G.12) are the same as equations (E.13)-(E.17) and (E.22), except for $g_z = {\Omega_{\rm K}}^2 z$ and $\partial g_z/\partial z \neq 0$. We assume that v_0, ρ_0 and P_0 are continuous at any z, and that $v_0(-z) = v_0(z)$, $\rho_0(-z) = \rho_0(z)$ and $P_0(-z) = -P_0(z)$.

To solve the linear perturbation equation (G.12), boundary conditions are needed. We consider the case with $\partial v_0/\partial z = 0$ and $\partial \rho_0/\partial z = 0$ at $|z| \geq z_{\rm d}$, where $z_{\rm d}$ is an arbitrary value and corresponds to the scale height of the dust layer. At $|z| \geq z_{\rm d}$, equation (G.12) is simplified as

$$\frac{d^2 w_1}{dz^2} - k^2 w_1 = 0. \tag{G.13}$$

From equation (G.13), we have

$$w_1 = \begin{cases} A_+ \exp(-kz) & (z \geq z_{\rm d}) \\ A_- \exp(kz) & (z \leq -z_{\rm d}) \end{cases}, \tag{G.14}$$

where A_+ and A_- are arbitrary constants. At $z = \pm z_{\rm d}$, P_1 should be continuous. From equations (G.7), (G.9) and (G.10), we have

$$P_1 = \frac{i\rho_0\bar{\omega}}{k^2}\left(\frac{dw_1}{dz} - \frac{1}{\bar{v}}\frac{dv_0}{dz}w_1\right). \tag{G.15}$$

At $|z| \geq z_{\rm d}$, using equation (G.14), equation (G.15) is simplified as

$$P_1 = \begin{cases} -(i\rho_0\bar{\omega}/k)w_1 & (z \geq z_{\rm d}) \\ (i\rho_0\bar{\omega}/k)w_1 & (z \leq -z_{\rm d}) \end{cases}. \tag{G.16}$$

At $z = \pm z_{\rm d}$, from equations (G.15) and (G.16), we have

$$\frac{dw_1}{dz} + \left(\pm k - \frac{1}{\bar{v}}\frac{dv_0}{dz}\right) w_1 = 0 \text{ at } z = \pm z_{\rm d}. \tag{G.17}$$

From equation (G.17), there are two types of solutions: odd solutions, where $w_1(-z) = -w_1(z)$, i.e.,

$$w_1 = 0 \text{ at } z = 0, \tag{G.18}$$

and even solutions, where $w_1(-z) = w_1(z)$, i.e.,

$$\frac{dw_1}{dz} = 0 \text{ at } z = 0. \tag{G.19}$$

As the same in the case in the Appendix E, the mode with $k_x = 0$ is the most unstable. For such a mode, k is equal to k_y, and the linear perturbation equation is given by

$$\frac{d^2w_1}{dz^2} + \frac{1}{\rho_0}\frac{d\rho_0}{dz}\frac{dw_1}{dz} - \left(k^2 + \frac{1}{\bar{v}}\frac{d^2v_0}{dz^2} + \frac{1}{\rho_0}\frac{d\rho_0}{dz}\frac{1}{\bar{v}}\frac{dv_0}{dz} + \frac{{\Omega_{\rm K}}^2 z}{\bar{v}^2}\frac{1}{\rho_0}\frac{d\rho_0}{dz}\right) w_1 = 0. \tag{G.20}$$

Boundary conditions are given by

$$w_1 = 0 \text{ at } z = 0 \text{ (odd mode)}, \tag{G.21}$$

$$\frac{dw_1}{dz} = 0 \text{ at } z = 0 \text{ (even mode)}, \tag{G.22}$$

and

$$\frac{dw_1}{dz} + \left(k - \frac{1}{\bar{v}}\frac{dv_0}{dz}\right) w_1 = 0 \text{ at } z = z_{\rm d}. \tag{G.23}$$

Equation (G.20) is applicable to the case with the continuous density distribution. On the other hand, in the Appendix E, we considered the case with discontinuous density distribution. This is the difference between the Appendix E and the Appendix G.

Bibliography

Adachi, I., Hayashi, C., & Nakazawa, K. 1976, Prog. Theor. Phys., 56, 1756

Bai, X.-N., & Stone, J. M. 2010, ApJ, 722, 1437

Barranco, J. A. 2009, ApJ, 691, 907

Binney, J., & Tremaine, S. 1987, Galactic Dynamics (Princeton, NJ: Princeton Univ. Press), 310

Blum, J., & Wurm, G. 2000, Icarus, 143, 138

Cameron, A. G. W. 1978, M&P, 18, 5

Carson, J., Thalmann, C., Janson, M., Kozakis, T., Bonnefoy, M., Biller, B., Schlieder, J., Currie, T., McElwain, M., Goto, M., Henning, T., Brandner, W., Feldt, M., Kandori, R., Kuzuhara, M., Stevens, L., Wong, P., Gainey, K., Fukagawa, M., Kuwada, Y., Brandt, T., Kwon, J., Abe, L., Egner, S., Grady, C., Guyon, O., Hashimoto, J., Hayano, Y., Hayashi, M., Hayashi, S., Hodapp, K., Ishii, M., Iye, M., Knapp, G., Kudo, T., Kusakabe, N., Matsuo, T., Miyama, S., Morino, J., Moro-Martin, A., Nishimura, T., Pyo, T., Serabyn, E., Suto, H., Suzuki, R., Takami, M., Takato, N., Terada, H., Tomono, D., Turner, E., Watanabe, M., Wisniewski, J., Yamada, T., Takami, H., Usuda, T., & Tamura, M. 2013, ApJ, 763, L32

Chandrasekhar, S. 1961, Hydrodynamic and Hydromagnetic Stability (Oxford: Clarendon Press), 428

Chiang, E. 2008, ApJ, 675, 1549

Cuzzi, J. N., Dobrovolskis, A. R., & Champney, J. M. 1993, Icarus, 106, 102

Dobrovolskis, A. R., Dacles-Mariani, J. S., & Cuzzi, J. N. 1999, J. Geophys. Res., 104, 30805

Dodson-Robinson, S. E., Veras, D., Ford, E. B., & Beichman, C. A. 2009, ApJ, 707, 79

Dominik, C., & Tielens, A. G. G. M. 1997, ApJ, 480, 647

Doyle, L. R., Carter, J. A., Fabrycky, D. C., Slawson, R. W., Howell, S. B., Winn, J. N., Orosz, J. A., Pr˘sa, A., Welsh, W. F., Quinn, S. N., Latham, D., Torres, G., Buchhave, L. A., Marcy, G. W., Fortney, J. J., Shporer, A., Ford, E. B., Lissauer, J. J., Ragozzine, D., Rucker, M., Batalha, N., Jenkins, J. M., Borucki, W. J., Koch, D., Middour, C. K., Hall, J. R., McCauliff, S., Fanelli, M. N., Quintana, E. V., Holman, M. J., Caldwell, D. A., Still, M., Stefanik, R. P., Brown, W. R., Esquerdo, G. A., Tang, S., Furesz, G., Geary, J. C., Berlind, P., Calkins, M. L., Short, D. R., Steffen, J. H., Sasselov, D., Dunham, E. W., Cochran, W. D., Boss, A., Haas, M. R., Buzasi, D., & Fischer, D. 2011, science, 333, 1602

Epstein, P. S. 1924, Phys. Rev., 23, 710

Garaud, P., & Lin, D. N. C. 2004, ApJ, 608, 1050

Goldreich, P., & Lynden-Bell, D. 1965, MNRAS, 130, 97

Goldreich, P., & Ward, W. R. 1973, ApJ, 183, 1051

Gómez, G. C., & Ostriker, E. C. 2005, ApJ, 630, 1093

Goodman, A. A., Benson, P. J., Fuller, G. A., & Myers, P. C. 1993, ApJ, 406, 528

Hasegawa, Y., & Tsuribe, T. 2013, PASJ, 65, 51

Hasegawa, Y., & Tsuribe, T. 2014, PASJ, 66, L2, in press (arXiv:1311.7471)

Hayashi, C. 1981, Prog. Theor. Phys. Suppl., 70, 35

Hayashi, C., Nakazawa, K., & Nakagawa, Y. 1985, In Protostars and Planets II (Univ. of Arizona Press), 1100

Hayashi, C., Narita, S., & Miyama, S. M. 1982, Prog. Theor. Phys., 68, 1949

Hirano, T., Narita, N., Sato, B., Takahashi, Y. H., Masuda, K., Takeda, Y., Aoki, W., Tamura, M., & Suto, Y. 2012, ApJ, 759, L36

Ishitsu, N., & Sekiya, M. 2002, Earth, Planets, Space, 54, 917

Ishitsu, N., & Sekiya, M. 2003, Icarus, 165, 181

Johansen, A., Henning, T., & Klahr, H. 2006, ApJ, 643, 1219

Johansen, A., & Youdin, A. 2007, ApJ, 662, 627

Kalas, P., Graham, J. R., Chiang, E., Fitzgerald, M. P., Clampin, M., Kite, E. S., Stapelfeldt, K., Marois, C., & Krist, J. 2008, science, 322, 1345

Kempf, S., Pfalzner, S., & Henning, T. K. 1999, Icarus, 141, 388

Kimura, S. S., & Tsuribe, T. 2012, PASJ, 64, 116

Kokubo, E., & Ida, S. 1996, Icarus, 123, 180

Kokubo, E., & Ida, S. 1998, Icarus, 131, 171

Kokubo, E., & Ida, S. 2000, Icarus, 143, 15

Lee, A. T., Chiang, E., Asay-Davis, X., & Barranco, J. 2010, ApJ, 718, 1367

Marois, C., Macintosh, B., Barman, T., Zuckerman, B., Song, I., Patience, J., Lafrenière, D., & Doyon, R. 2008, science, 322, 1348

Mayor, M., & Queloz, D. 1995, Nature, 378, 355

Michikoshi, S., & Inutsuka, S. 2006, ApJ, 641, 1131

Mizuno H., 1980, Prog. Theor. Phys., 64, 544

Nakagawa, Y., Nakazawa, K., & Hayashi, C. 1981, Icarus, 45, 517

Nakagawa, Y., Sekiya, M., & Hayashi, C. 1986, Icarus, 67, 375

Nayakshin, S. 2010, MNRAS, 408, L36

Ohashi, N., Hayashi, M., Ho, P. T. P., Momose, M., Tamura, M., Hirano, N., & Sargent, A. I. 1997, ApJ, 488, 317

Okuzumi, S. 2009, ApJ, 698, 1122

Okuzumi, S., & Hirose, S. 2011, ApJ, 742, 65

Okuzumi, S., & Hirose, S. 2012, ApJ, 753, L8

Okuzumi, S., Tanaka, H., Kobayashi, H., & Wada, K. 2012, ApJ, 752, 106

Okuzumi, S., Tanaka, H., & Sakagami, M. 2009, ApJ, 707, 1247

Rafikov, R. R. 2005, ApJ, 621, L69

Roe, P. L. 1986, Ann. Rev. Fluid Mech., 18, 337

Safronov, V. S. 1969, Evolution of the Protoplanetary Cloud and Formation of the Earth and Planets (Moscow: Nauka) (Translation 1972, NASA Tech. Trans. F-677), 206

Sano, T., Miyama, S. M., Umebayashi, T., & Nakano, T. 2000, ApJ, 543, 486

Sekiya, M. 1983, Prog. Theor. Phys., 69, 1116

Sekiya, M. 1998, Icarus, 133, 298

Sekiya, M., & Ishitsu, N. 2000, Earth Planets Space, 52, 517

Sekiya, M., & Ishitsu, N. 2001, Earth Planets Space, 53, 761

Suyama, T., Wada, K., & Tanaka, H. 2008, ApJ, 684, 1310

Takeuchi, T., Muto, T., Okuzumi, S., Ishitsu, N., & Ida, S. 2012, ApJ, 744, 101

Tanaka, H., Himeno, Y., & Ida, S. 2005, ApJ, 625, 414

Toomre, A. 1964, ApJ, 139, 1217

Trubnikov, B. A. 1971, Soviet Phys. Dokl., 16, 124

Umebayashi, T. 1983, Prog. Theor. Phys., 69, 480

Wada, K., Tanaka, H., Suyama, T., Kimura, H., & Yamamoto, T. 2007, ApJ, 661, 320

Wada, K., Tanaka, H., Suyama, T., Kimura, H., & Yamamoto, T. 2009, ApJ, 702, 1490

Watanabe, S., & Yamada, T. 2000, Eos, Trans. Am. Geoph. Union Suppl., 81, 22, 99

Weidenschilling, S. J. 1980, Icarus, 44, 172

Wetherill, G. W., & Stewart, G. R. 1989, Icarus, 77, 330

Wurm, G., & Blum, J. 1998, Icarus, 132, 125

Youdin, A. N., & Goodman, J. 2005, ApJ, 620, 459

Zhou, S., Evans, N. J., II, Kömpe, C., & Walmsley, C. M. 1993, ApJ, 404, 232

Zsom, A., Ormel, C. W., Güttler, C., Blum, J., & Dullemond, C. P. 2010, A&A, 513, A57